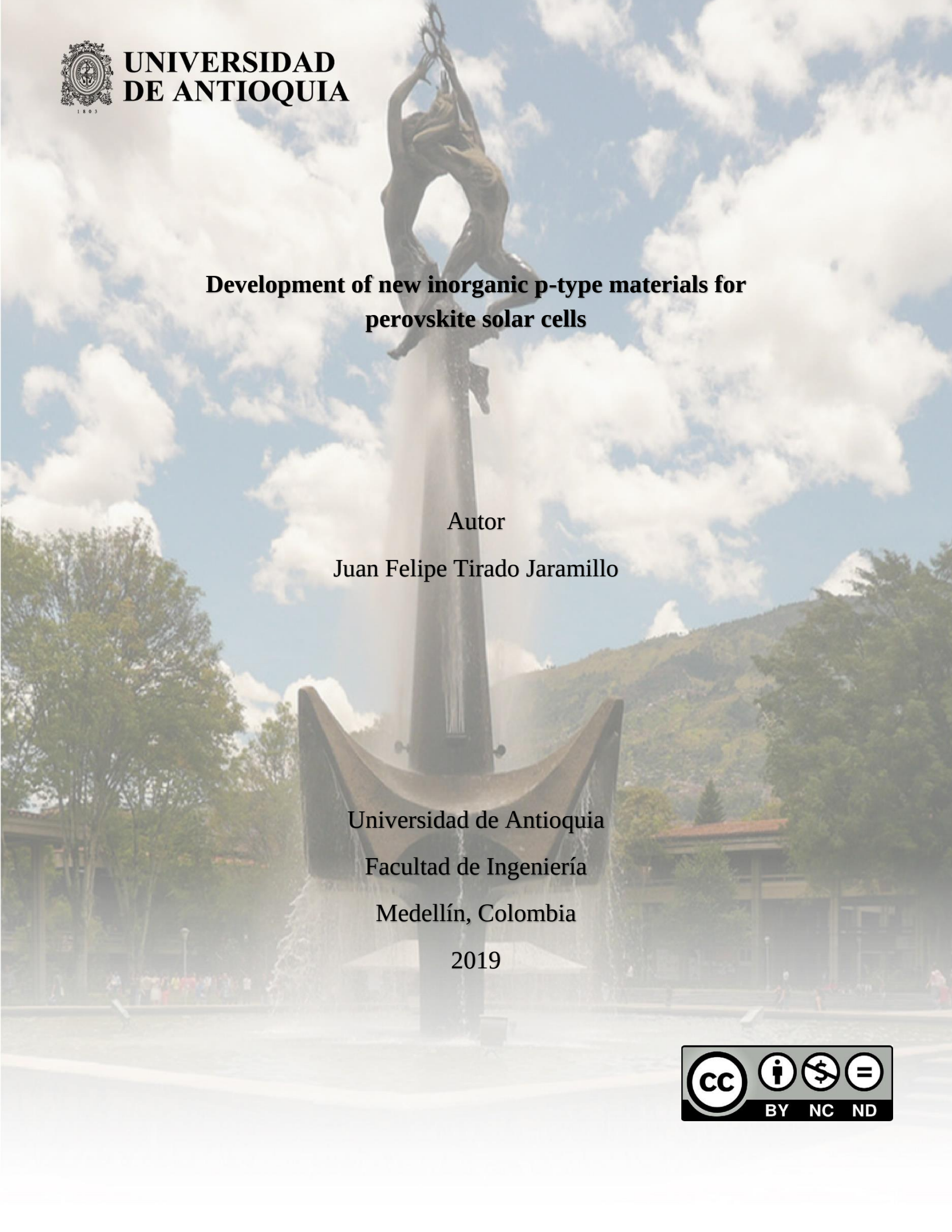

UNIVERSIDAD DE ANTIOQUIA

# Development of new inorganic p-type materials for perovskite solar cells


Autor

Juan Felipe Tirado Jaramillo

Universidad de Antioquia

Facultad de Ingeniería

Medellín, Colombia


2019

# Development of new inorganic p-type materials for perovskite solar cells

Juan Felipe Tirado Jaramillo

Faculty of Engineering

Universidad de Antioquia

Advisor Prof. Franklin Jaramillo Isaza. PhD

A thesis submitted to accomplish all the requirements for the degree of

Doctor in Materials Engineering at the University of Antioquia

September 2019

# Abstract

Photovoltaic (PV) energy is one the most promising alternatives to replace fossil fuels as main electricity source and decrease greenhouse effect caused by related $CO_2$ emissions. Perovskite solar cells (PSC) is a third generation PV technology which has revolutionized this field because of its extremely fast increase in power conversion efficiency (PCE). Remarkably, PSC PCE has achieved values >24% being comparable with polycrystalline silicon and thin film PV (CdTe, CIGS) so that it has become in a real alternative to traditional silicon PV. In order to reach a commercialization quality level, PSC need to improve its long-term stability, PCE of large devices and cost-effectiveness. It has been widely recognized that charge selective layers are crucial components of PSC structure for managing of photogenerated charges. Specifically, hole-transporting materials (HTM) have a strong influence on device performance, stability and cost. However, they represent one of the major bottleneck for PSC commercialization owing to unstable and expensive organic molecules materials often employed. In this framework, inorganic p-type semiconductors are a promising option to overcome issues related to organic HTM because of their intrinsic good properties as hole selective contacts and ambient stability. Nevertheless, relative few inorganic materials have been explored for this function so that they have not reached organic counterparts' performance. Thus, it is mandatory to explore and optimize new inorganic alternatives for HTM in PSC.

Accordingly, in this thesis two inorganic p-type semiconductors, namely, copper sulfide and nickel oxide, have been applied in two different PSC architectures by three distinct approaches. First, copper sulfide thin films ($Cu_xS$) were fabricated by spray pyrolysis technique and applied as semi-transparent electrode in planar p-i-n PSC. Morphological and optoelectronic properties of $Cu_xS$ were correlated with

device performance. In the second approach, copper sulfide was synthesized in the form of nanoparticles (CuS NPs) and colloidal dispersions in non-polar solvents were obtained. Subsequently, the CuS NPs were applied by spin-coating technique in a mesoscopic n-i-p architecture, acting as sole HTM and exhibiting efficiencies over 13%. Third, hydrophobic nickel oxide (ho-$NiO_x$) nanocrystals were synthesized and corresponding colloidal dispersions were obtained. Then, n-i-p planar PSC were fabricated employing ho-$NiO_x$ as sole HTM which was deposited by solution-process spin-coating. Remarkably, PCE as high as 12.7% and impressive high-humidity air stability was observed. Namely, PCE retention over 90% was exhibited by ho-$NiO_x$-based PSC for more than 1000 h. The optoelectronic properties, energy band alignment and interface phenomena are studied and discussed in detailed for all the obtained semiconductors and devices.

KEYWORDS: Perovskite solar cells, inorganic hole transporting materials, stability, low-cost, solution process.

## Acknowledgements

First of all, I want to thank my parents for their unconditional support in all aspects of my life and for giving me the strength to pursue my dreams. Also, I would like to thank my advisor Prof. Franklin Jaramillo for trusting me and for giving me the opportunity to travel a four-year path that changed my life on a professional and personal level.

Sincere thanks go to Prof. Mohammad Khaja Nazeeruddin for giving me the chance to work in his group for six months. To GMF team members for sharing their knowledge and for making my stay in Switzerland a very rewarding experience.

I would like to thank all CIDEMAT energy line group members: Daniel, Rafael, Mario, Juan, Johny, John, José Ignacio, Santiago, Esteban and Manuel for the fruitful scientific discussions, advice and for sharing their knowledge and experiences.

Finally, I must thank God for putting all these wonderful people in my way.

Medellín, 31 March 2019

# Abbreviations

| | |
|---|---|
| AFM | Atomic Force Microscopy |
| CB | Conduction band |
| $CO_2$ | Carbon dioxide |
| CuS NPs | Copper sulfide nanoparticles |
| $Cu_xS$ | Mixed crystal phases copper sulfide |
| DSSC | Dye-sensitized solar cells |
| ETM | Electron-transporting material |
| FF | Fill Factor |
| FoM | Figure of Merit |
| FTO | fluorine-doped tin oxide |
| ho-$NiO_x$ | Hydrophobic nickel oxide |
| HTM | Hole-transporting material |
| IPCC | Intergovernmental Panel on Climate Change |
| ITO | indium-doped tin oxide |
| $J_{MPP}$ | Current at maximum power point |
| $J_{sc}$ | Short circuit current density |
| J-V | Current-Voltage |
| $NiO_x$ | Nickel oxide |
| PCE | Power conversion efficiency |
| $P_{in}$ | incident light power density |
| $P_{max}$ | Maximum Power point |
| PSC | Perovskite solar cells |
| PV | Photovoltaics |

| | |
|---|---|
| SEM | Scanning electron microscopy |
| SPO | Stabilized power output |
| TCE | Transparent conductive electrode |
| TCO | Transparent conductive oxide |
| TEM | Transmission electron microscopy |
| VB | Valence band |
| $V_{MPP}$ | Voltage at maximum power point |
| $V_{oc}$ | Open circuit voltage |

# Contents


Abstract…… 2

Acknowledgements…… 4

Abbreviations……..... 5

1. Introduction…… 9

    1.1. Motivation…… 9

    1.2. Perovskite solar cells……... 11

        1.2.1. Material……... 11

        1.2.2. Photovoltaic parameters…….. 12

        1.2.3. Device structures……... 13

        1.2.4. Hole transporting materials…… 19

            1.2.4.1. Role of HTM on PSC performance…….. 19

            1.2.4.2. Inorganic HTM……... 22

        1.2.5. Materials cost in PSC…… 26

    1.3. Thesis synopsis…… 27

        1.3.1. Aim of the thesis……... 27

        1.3.2. Outline of the thesis…….. 28

2. Chapter 2. Low-cost semi-transparent copper sulfide electrode for indium-tin-oxide-free perovskite solar cells……. 30

    2.1. Introduction…….. 30

    2.2. Copper sulfide thin films fabrication and basic characterization……. 32

    2.3. Perovskite solar cells employing copper sulfide as electrode……... 36

    2.4. Conclusions……... 42

3. Chapter 3. Copper sulfide nanoparticles as hole-transporting-material in a fully-inorganic blocking layers n-i-p perovskite solar cells: Application and working insights…….. 44

3.1. Introduction…….. 44
3.2.Copper sulfide nanoparticles synthesis and characterization…… 45
3.3. Mesoscopic PSC employing CuS nanoparticles as HTM……... 49
3.4. Insights on CuS working mechanisms as HTM in n-i-p PSC…… 55
3.5. Conclusions……... 60
4. Chapter 4. Air-stable n-i-p planar perovskite solar cells using nickel oxide nanocrystals as sole hole-transporting material……. 62
4.1. Introduction…….. 62
4.2. Synthesis and characterization of nickel oxide nanocrystals…… 64
4.3. Application of nickel oxide nanocrystals as HTM in planar n-i-p PSC... 67
4.4. Conclusions……... 81
5. Experimental part……... 83
6. Appendix…….. 90
7. General conclusions and outlook……. 96
8. References…… 99

# 1. Introduction

## 1.1. Motivation

At present, humanity is starting to recognize that the sources from which we obtain the necessary energy to sustain productive chains, access services and in general, cover the needs of society are having a negative effect on the environment. An example of this is the increase in global temperatures above the level expected as safe, more specifically, it is expected that the temperature increases by 2050 about 3.6 ° C, which is well above the 2° C calculated as natural by the International Energy Agency (IEA)[1]. Associated with this exaggerated increase in global temperature, it is expected that the risk of food security, access to potable water, extreme natural phenomena and the loss of marine and coastal ecosystems will increase considerably, which calls into question our ability to maintain the current standard of living[2]. The Intergovernmental Panel on Climate Change (IPCC) indicates that the main agent causing the planet temperature increase is $CO_2$ which derives from the burning of fossil fuels. Interestingly, 80% of the energy used on the planet[2] come from mentioned non-renewable and pollutant source, making this situation very worrying if we consider that the increase in total energy demand is expected to double and that the demand for electric power quadruples by the year 2050. Given this scenario, renewable energy sources are shown as the best strategy to cover the demand for power (under current standards of living) that can reach 60 TW for a future population of 10 billion people[1]. Among the alternatives are wind energy, hydro power, geothermal energy and photovoltaic solar energy (PV)[3]

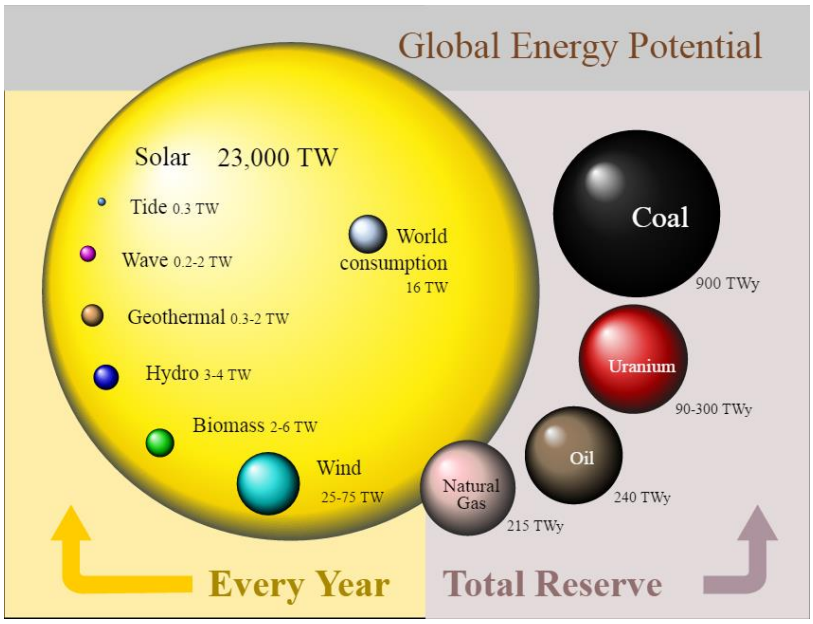


**Figure 1.1.** Generation potential of different energy sources. Figure from http://asrc.albany.edu/people/faculty/perez/Kit/pdf/a-fundamental-look-at%20the-planetary-energy-reserves.pdf.

However, PV is the most viable option to cover, in a sustainable way, the growing energy demand because it is based on an inexhaustible and excessive source[4]. For example, in an hour the Earth surface receives from the sun the energy that the humanity uses in one year[1] (see **Figure 1.1**). Additionally, taking into account that around 40% of $CO_2$ emissions are produced after electricity generation[5], it is evident that the PV, whose objective is the production of electricity, is the best option to reduce greenhouse gas emissions, this is demonstrated by new investments in renewable technologies at **Figure 1.2**. At present, there are already government efforts, although still few, to insert solar energy into the markets and achieve price parity with respect to the energy generated by fossil fuels[1].

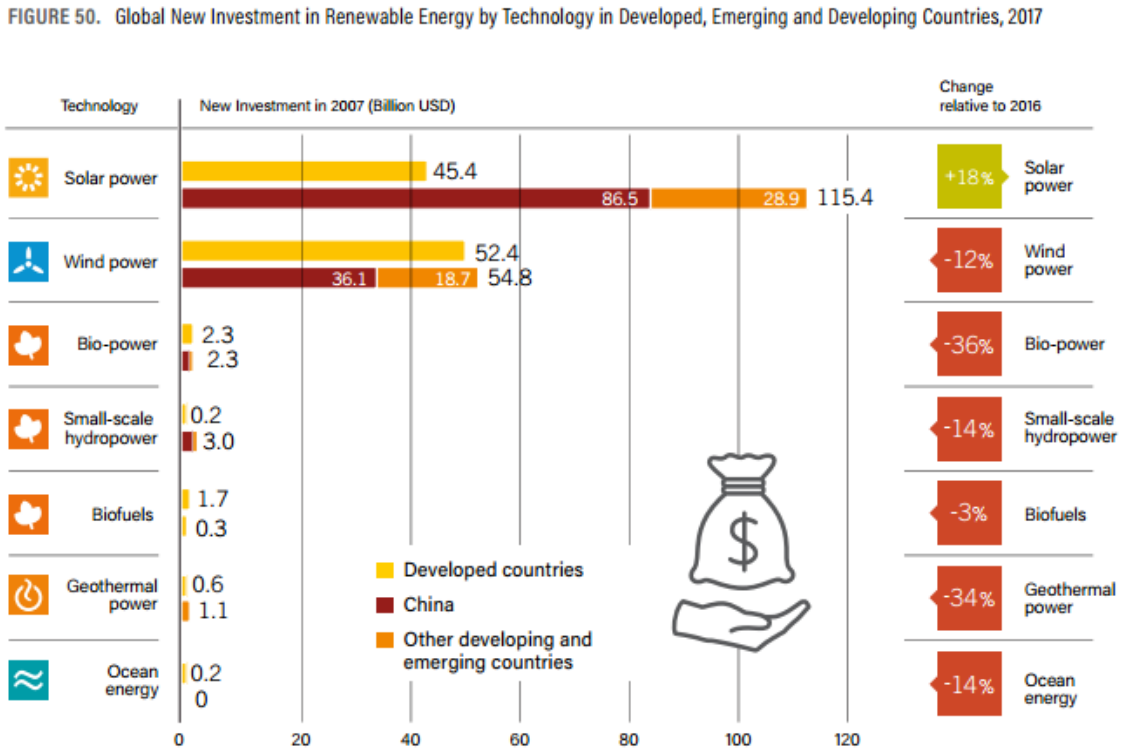


**Figure 1.2.** Global new investment in renewable energy technology expected in 2017 Image from Reference[5].

To consistently promote the PV market, there is an urgent need to establish a cost-effective PV industry that can survive without government subsidies[6]. The effort to lower costs has resulted in the development of many new PV technologies based on cheap materials and low-cost processes, such as thin film silicon solar cells, thin film CdTe, CIGS, dye-sensitized solar cells (DSSC), organic solar cells and recently perovskite solar cells.

## 1.2. Perovskite solar cells

### 1.2.1. Material

Perovskite solar cells (PSC) are a type of third generation solar cells which have received a tremendous attention and research efforts during the last decade. Since the first report in 2009 their power conversion efficiency (PCE) has raised from ~3%

until certified values of ~24% which is comparable with performance of polycrystalline silicon devices and thin film solar cells such as CdTe or CIGS[7–10]. In fact, PSC have become in the most promising alternative to replace silicon based solar cells by more cost-effective PV technologies with attractive properties such as transparency, color control, flexibility, low weight and so on[1]. The main reason is the proper combination of desirable properties of light harvester. Namely, the core of PSC is the organic-metallic mixed halide perovskite absorber which present an $ABX_3$ perovskite structure. Position A can be made up of an organic or inorganic cation (i.e., $MA^+$: $CH_3NH_3^+$, $FA^+$: $CH_3(NH_2)_2^+$, $Rb^+$ and $Cs^+$), B is normally a metal cation such as $Pb^{2+}$ or $Sn^{2+}$ and X can be a halide anion (i.e., $Cl^-$, $Br^-$, $I^-$, $BF4^-$, $SCN^-$ and so on)[10,11]. Corresponding crystal structure is normally a 3D network of corner sharing BX6 octahedra with the A ion sit in the cuboctahedral interstices inside a perovskite structure and forming a cubic Pm3m crystal structure[12]. The prime advantage of this kind of materials is their direct band gap, low exciton binding energy (~2 meV), large absorption coefficient ($5.7\ x\ 10^4\ cm^{-1}$) enabling efficient light absorption in thin films, long diffusion length (~1 μm in thin films), high electron and hole mobility (10-2320 $cm^2\ V^{-1}\ s^{-1}$), simple and easy fabrication techniques (most of them compatible with solution process methods)[13,14]. In addition, replacement of A and X positions by different species allows to tune the optical and electronic properties of perovskite films make them suitable for a variety of applications and device structures[15]. Thus, organic-metallic mixed halide perovskites represent an ideal material for photovoltaics.

### 1.2.2. Photovoltaic parameters

Performance of PSC is characterized by running photocurrent-voltage curve (J-V curve) sweep under standard 1-sun intensity (1000 W $m^{-2}$ illumination with AM1.5G spectrum). Basically, an external potential bias is applied to the cell while measuring

the current response (see **Figure 1.3a**). The result is a curve, where open-circuit voltage ($V_{oc}$) is determined as the measured potential at open-circuit condition when the current density equals to 0 mA cm$^{-2}$ and short-circuit current ($J_{sc}$) is the current density at short-circuit condition when voltage is equal to 0 V. On the other hand, maximum power point ($P_{max}$) is the point at which voltage ($V_{MPP}$) and current density ($J_{MPP}$) product results in maximum power output from the device (see **Figure 1.3b**)[1,16]. To extract PCE it is necessary to divide $P_{max}$ by the incident light power density $P_{in}$.

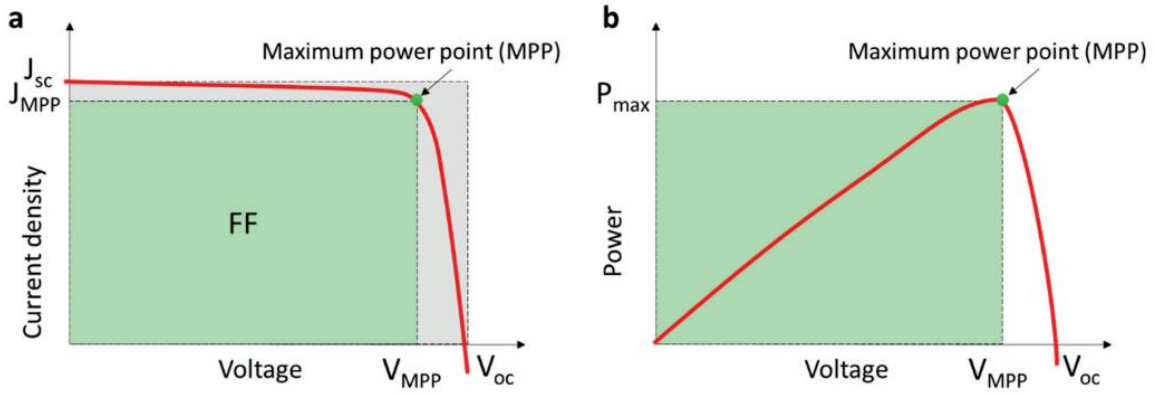


**Figure 1.3.** (a) Typical J-V curve of solar cells. (b) Power vs Voltage curve showing maximum power point. From Domanski[17].

$$PCE = \frac{P_{max}}{P_{in}} = \frac{V_{MPP}\,J_{MPP}}{P_{in}} = \frac{FF\,V_{OC}J_{SC}}{P_{in}} \quad Eq\ 1$$

$V_{MPP}$ and $J_{MPP}$ are not practical parameters to characterize solar cells, so that a geometrical factor (Fill Factor: *FF*) is introduced to relate those to $J_{sc}$ and $V_{oc}$. Additionally, *FF* means that J-V curve is not square due to diode behavior of solar cells and the power obtained is less than the product of $J_{sc}$ and $V_{oc}$.

### 1.2.3. Device structures

In terms of architecture, PSC are commonly a multilayered system where perovskite absorber is accompanied by at least four more layers to allow efficient photovoltaic conversion[10,18]. Particularly, light absorbed by perovskite promotes the generation of

an electron-hole pair in the bulk of the material, then they separate and diffuse to proper direction due to charge selective materials: hole and electron transporting layers (HTM and ETM, respectively). Finally, free charge carriers are collected at proper electrode, namely, transparent conductive or back metal electrode. Depending on whether the perovskite is deposited on an n-type (ETM) or p-type (HTM) semiconductor (**Figure 1.4**) the structure receives the name of n-i-p (normal) or p-i-n (inverted) PSC, respectively[11]. Moreover, each architecture involves advantages and disadvantages as well as different combination of materials because of intrinsic technological challenges to deposit each layer[18].

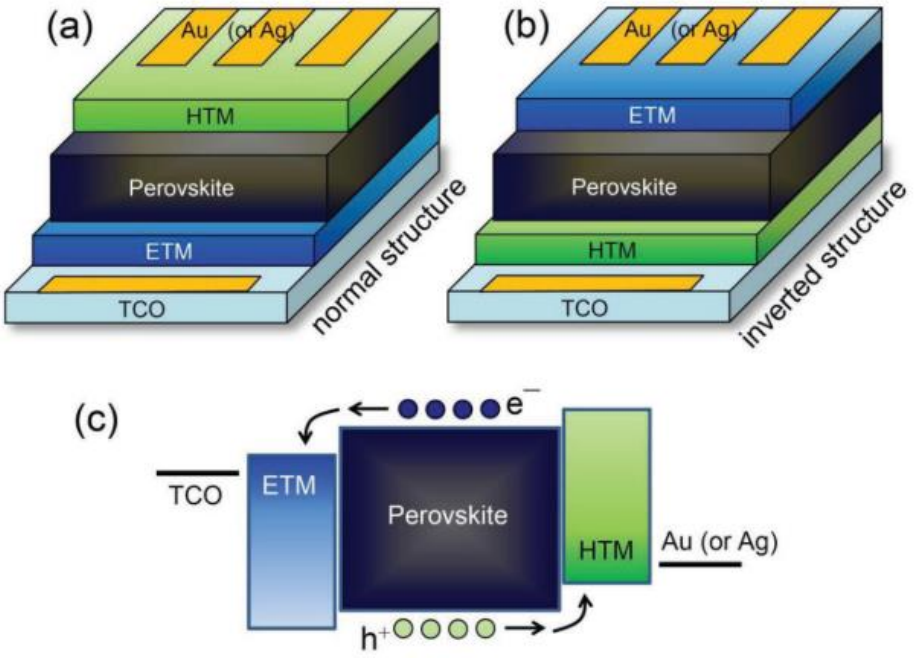


**Figure 1.4**. PSC structure types and basic working principle. From ref[19]. (a) Normal or direct PSC architecture, (b) inverted PSC and (c) charge carriers separation scheme.

Specifically, n-i-p architecture can be divided into two types: mesoporous and planar devices (see **Figure 1.5a and 1.5b**). Mesoporous ones are based on a transparent electrode commonly fluorine-doped tin oxide (FTO) or indium-doped tin oxide (ITO) through which the light enters the device, then a compact thin layer

of $TiO_2$ (~20-50 nm) as a hole-blocking layer, a mesoporous layer of $TiO_2$ or $Al_2O_3$ (forming the so called meso-superstructured PSC) with thickness around 100-300 nm and filled with perovskite material, then an HTM (100-300 nm) is deposited on perovskite film. Finally a metal electrode, usually Ag or Au (50-100 nm) is deposited by vacuum thermal deposition. This is called normal structure because the first demonstration of organic-metallic mixed halide perovskite as a light harvester in a functional solar cell was done by Kojima et al. in a DSSC device structure, employing perovskite as a sensitizer on a thick $TiO_2$ mesoporous layer and a liquid electrolyte[20]. Subsequently, Kim et al. demonstrated a solid-state device by replacing liquid electrolyte by the organic molecule 2,2′,7,7′-tetrakis-(N,N-di-4-methoxyphenylamino)- 9,9′-spirobifluorene (Spiro-OMeTAD) obtaining a PCE of 9.7%, a considerable enhancing in stability and marking a breakthrough in third generation solar cells field[21]. After intense developments, PCE in n-i-p mesoporous structure has reached values around 24%[8], being the most efficient structure so far. Planar n-i-p PSC where first reported by Snaith and coworkers in 2012, they avoided the TiO2 mesoporous layer without a relevant lose in charge generation due to high absorption coefficient of perovskite[22]. Nowadays, planar n-i-p have exhibited PCE as high as 20.8%[23].

On the other hand, inverted or p-i-n structure is based on the opposite arrangement than n-i-p PSC (**Figure 1.5c**). This kind of devices are also built on transparent conductive electrode (TCO), usually ITO. Then a compact HTM layer (<40 nm) is deposited on TCO, commonly the organic polymer poly(3,4-ethylenedioxythiophene)-poly(styrenesulfonate) (PEDOT:PSS) or recently some inorganic p-type semiconductors such as $NiO_x$. Perovskite absorber is deposited onto HTM and subsequently an ETM layer (~50 nm) is fabricated on top of light harvester. Most representative ETM for this architecture is a fullerene derivate [6,6]-

phenyl-$C_{61}$-butyric acid methyl ester ($PC_{61}BM$)[23]. From the first report of p-i-n PSC in 2013 by Jeng et al. PCE has reached from 3.9% to more than 20%[24]. This structure, which has been inspired by typical organic solar cells (OSC), allows to fabricate devices by low temperature processes (<150°C) because of avoiding $TiO_2$ and related high crystallization temperatures, making this architecture suitable for roll-to-roll and inject printing fabrication[25]. In addition, p-i-n PSC can include an insulating $Al_2O_3$ mesoporous layer being an inverted meso-superstructured device. Ramirez at al. demonstrated the positive roll of $Al_2O_3$ scaffold to improve reproducibility and stability of large scale PSC modules retaining considerable PCE for more than 2000 h in outdoor conditions[26]. Thus, p-i-n architecture has attracted a lot of attention for scaling up purposes.

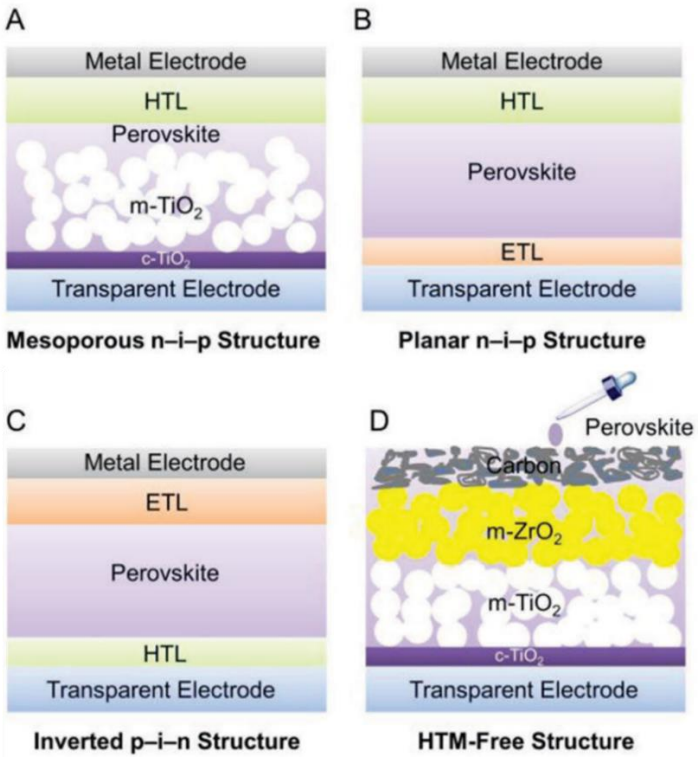


**Figure 1.5.** PSC architectures from ref[23]. (a) Mesoporous n-i-p, (b) planar n-i-p, (c) inverted p-i-n and (d) HTM free structures.

**Figure 1.5d** shows an HTM-free PSC or "infiltrable" architecture which was first reported by Han and coworkers in 2013[25]. The structure is composed by a transparent electrode (FTO) with a dense compact $TiO_2$ layer on top. Then a $TiO_2$ mesoporous layer is screen printed as an ETM followed by an insulating mesoporous layer of $ZrO_2$ which acts as a space layer to prevent short circuit. Subsequently, a carbon paste is printed and annealed at high temperature to obtain a porous carbon black electrode. Finally, perovskite absorber is infiltrated in the complete structure from an appropriate precursor followed by an annealing process[12]. This PSC architecture has shown PCE as high as 15.6% and exhibited a notably stability owing to inorganic mesoporous components. However, high temperatures involved in fabrication process hinders HTM-free PSC scalability and cost-effectiveness[27].

Organic-metallic mixed halide perovskite is the core of the PSC so that a great deal of deposition strategies have been developed during a decade of intense research to obtain highly crystalline and homogeneous films. Methylammonium lead iodide ($CH_3NH_3PbI_3$) is the most simple and widely used perovskite absorber[28]. As mentioned above it is a part of a family of materials with appropriate optoelectronic properties for photovoltaic applications. Interestingly, organic-metallic mixed halide perovskite thin films can be fabricated by simple solution process taking advantage of its tendency to crystalize at relative low temperatures by solvent evaporation from inexpensive precursors (lead salts and organic halides) and solvents such as N,N-dimethylformamide (DMF), dimethylsulfoxide (DMSO) or γ-butyrolactone (GBL)[29]. Most common deposition techniques are spin-coating: one or two step process, sequential deposition, anti-solvent quenching (by spin-coating), vapor assisted deposition or vacuum-assisted solvent drying[15].

In order to improve PSC efficiency and stability, different variations of A, B and X positions of $ABX_3$ perovskite structure have been tested. Namely, A position has been completely or partially replaced by $FA^+$ or $Cs^+$ obtaining faster crystallization, larger grain size and more resistance against moisture. Also, X position has been occupied by $I^-$, $Br^-$ or $Cl^-$ anions and mixtures of them improving film morphology and optoelectronic properties of devices. Moreover, a variety of divalent cations have been proposed to replace toxic lead such as $Sn^{2+}$, but $Pb^{2+}$ still shows the best performance so far[13–15,23]. Regarding stability, low dimensional layered systems like 2D perovskites have demonstrated to be a suitable alternative to have highly stable PSC especially against water-mediated degradation. The latter structures are obtained by partially or completely introducing large organic cations in A position such as PEA: $C_6H_5(CH_2)_2NH_3^+$, 5-ammoniumvaleric acid (5-AVA) and so on[13,14,30]. Alternatively, Grancini et al.[31] proposed a multidimensional 2D/3D perovskite combining the high optoelectronic properties of 3D perovskite with ambient and thermal stability of 2D counterparts exhibiting excellent PCE retention at common operational conditions for more than one year.

Despite of impressive advances achieved in the field of PSC, related to enhancement of PCE, there are several challenges to be overcome towards a realistic incursion of PSC technology in a commercial level. Particularly, i) efficiency of large scale devices, ii) stability and iii) devices cost-effectiveness are critical factors[14,30]. As described above, there are several solution strategies proposed in literature from perovskite absorber point of view. However, as a multilayered system PSC performance strongly depends on interaction of different materials involved in each architecture. In other words, interfaces between light harvester and HTM, ETM, and corresponding electrodes also affect PCE and operational stability[32]. Among mentioned materials, HTM still represents a major bottleneck on stability and

fabrication of large scale PSC due to the extended use of expensive and extrinsic unstable materials to achieve high performance devices[12]. Alternatives to state-of-the-art HTM deal with the tradeoff between efficiency and cost[33–35]. In the next section the role of HTM on PSC behavior, stability and device cost are discussed.

### 1.2.4. Hole transporting materials.

#### 1.2.4.1 Role of HTM on PSC performance.

In general PSC working principle has several steps: 1) generating electron-hole pairs; 2) excited electrons are transferred into conduction band (CB) of an n-type semiconductor; 3) formed holes in perovskite valence band (VB) are transferred to p-type semiconductor; 4) finally holes and electrons are collected on, respectively, front and back electrodes[16,36]. Thus, charge selective layer are necessary to achieve high photovoltaic performance and avoid undesirable charge-transfer processes at ETM/perovskite/HTM interfaces (see **Figure1.6**), especially because of low defect density and low recombination rates of organic-metallic mixed halide perovskite absorbers which leads to large diffusion lengths and long-lived charge carriers[32,37]. In other words, due to important advances on perovskite crystal quality and intrinsic defects tolerance of this material non-radiative losses are almost negligible compared with the ones caused by surface recombination at ETM/perovskite/HTM interfaces so that those interfaces strongly determine the quality of devices[32]. There are satisfactory advances in the development of chemical and thermal stable ETM based on earth abundant materials such as $TiO_2$ or $SnO_2$, specially, in n-i-p architecture[38]. Moreover, recombination in ETM/perovskite interface has been studied and considerable reduced by insertion of dopant agents or surface functionalities at ETM surface[37]. On the other hand, as said in previous section, HTM

is still a bottleneck due to instability of high performance materials and inherent high cost. Accordingly, there has been a huge research effort to resolve these issues so that it is possible to find an enormous catalogue of reported HTM and detailed studies of their respective influence on device performance, stability and cost.

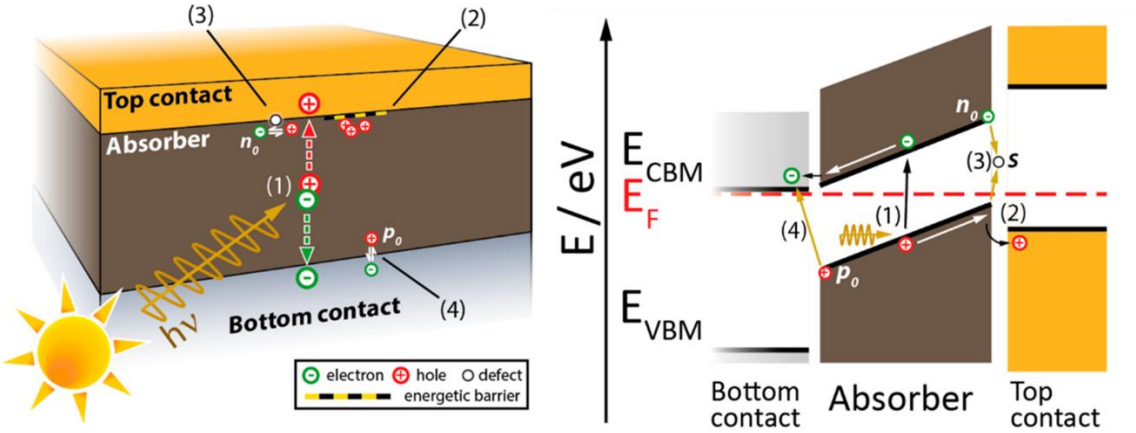


**Figure 1.6**. Schematic of loss mechanisms present at interfaces in a simplified photovoltaic device. After photoexcitation (1) and transport of free charge carriers to the contact interfaces, carrier extraction can be impaired by (2) interfacial energy barriers due to imperfect band alignment of perovskite absorber and charge selective layers, (3) defect-driven interface recombination, and (4) back recombination. $E_{CBM}$, $E_{VBM}$, and $E_F$ are the conduction band minimum, valence band maximum, and Fermi level, respectively. Figure re-drawn based on ref[32].

From operational point of view HTM serves different purposes in PSC: 1) it is a physical barrier between anode and perovskite absorber blocking electron transfer to anode; 2) it improves the hole transfer efficiency by reducing series resistance and increasing recombination resistance at perovskite/HTM interface; 3) it influences $V_{oc}$ by determining the splitting of quasi Fermi energy levels of light harvester and reducing non-radiative recombination; 4) it prevents degradation of absorber by avoiding metal electrode/perovskite contact, specially, when Ag is employed[12,39]. Also, it has the opposite effect when hygroscopic agents are used, as will be discussed later[40]. Accordingly, a proper HTM should offer a variety of properties

such as 1) high hole mobility to reduce losses during charge carrier transport to the hole collecting contact; 2) less negative and close VB (or HOMO level) with respect to perovskite VB to minimize injection losses; 3) high thermal and chemical stability to external degradation factor for long term durable devices; 4) low-cost and 5) low electron affinity to enhance electron blocking properties[23].

HTM employed in PSC can be categorized in organic and inorganic materials. Organic materials can also be divided into two types: small molecules and conducting polymers. Organic small molecules have been widely studied owing to their synthetic variety, tunable properties by chemical structural changes, high purity and simple solution processing[13,39]. In fact, state-of-the-art HTM used since first reports of solid-state PSC is the Spiro-OMeTAD which allowed to reach most of the highest efficient devices so far[28]. Another small molecules are based on benzotrithiophene (BTT), anthratetrathiophene (ATT), truxene (Trux), phenylpyrazole (PPyra), bipyridine, indolo[3,2-b]indole (IDID) and paracyclophance[23]. Despite of PCE easily exhibits more than 18%, these kind of materials suffer from intrinsic low hole mobility and poor conductivity in their pristine form. To reach high performance devices it is necessary to introduce p-dopants such as lithium trifluoromethanesulfonimide (Li-TFSI), 4-tert-butylpyridine (TBP) or cobalt(III) complex (FK209) (see **Figure 1.7**)[9,41,42].

Among conducting polymers poly-[bis(4-phenyl)(2,4,6-trimethylphenyl)amine] (PTAA) is the most efficient material so far, exhibiting PCE ~22%[39]. Polymers are attractive for PSC due to their fusibility, good solubility in commercial solvents, processability and high hole mobility[43,44]. However, good performance polymers like PTAA are extremely expensive (about 2000 US$/g)[23].

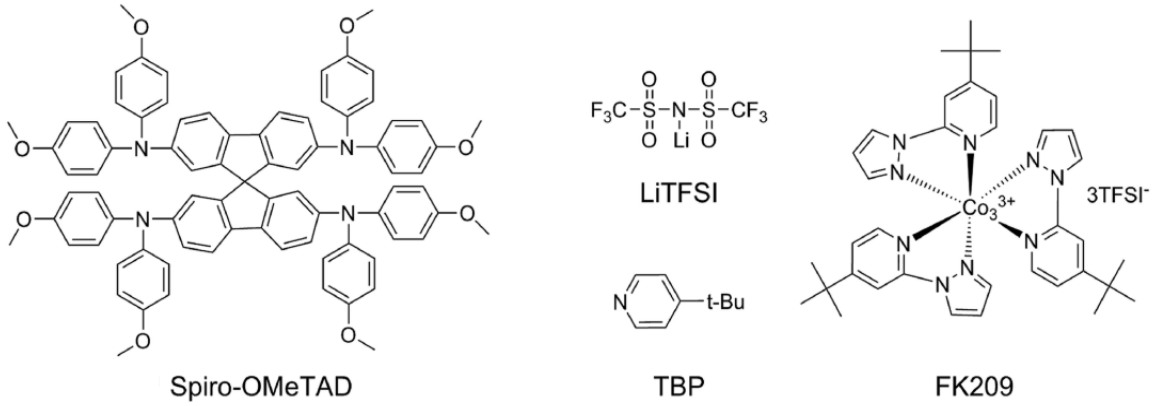


**Figure 1.7.** Spiro-OMeTAD and common p-doping agent chemical structures.

Despite of excellent PCE achieved using organic HTM, the obtained devices suffer from different obstacles such as stability issues owing to hygroscopic p-type dopants and material cost. Last but not least important, Spiro-OMeTAD and similar molecules are more expensive than noble metals like gold or platinum[45].

### 1.2.4.2. Inorganic HTM.

Inorganic HTM have attracted intense interest because of their intrinsic high chemical stability, high hole mobility and their cost-effective fabrication processes and related reagents. Thus, inorganic HTM are very promising candidates to overcome stability and cost issues that hinders PSC large scale production. However, inorganic p-type semiconductors have been less explored than organic counterparts owing to limited choice in suitable materials[45,46]. The most relevant inorganic HTM employed in PSC so far are mentioned as follows:.

*Nickel Oxide*

NiO thin films have been widely studied as HTM in PSC because of its intrinsic chemical and thermal stability, wide band gap, high optical transmittance and proper valence band alignment with various photoactive perovskite materials (~5.2-5.4 eV). Several methods are suitable for NiO films synthesis such as sol-gel, electro-

deposition, RF sputtering, e-beam evaporator, pulsed laser deposition (PLD), screen-printing technology or spin-coating. However, deposition on perovskite absorber limits synthetic routes alternatives so that most of the NiO-based PSC are reported at p-i-n architecture[47–49]. Corresponding devices often exhibit smaller *FF* than organic counterparts, whereas $V_{oc}$ is generally higher by effective charge carrier extraction and prolonged charge lifetime[12,39,49]. PCE as high as 20.65% has been achieved with NiO-based p-i-n PSC employing spray coating technique[50].

*Molybdenum trioxide*

$MoO_3$ (usually $MoO_x$) is a transition metal oxide with non-toxicity and high ambient stability used as either a buffer layer or sole extraction layer in a variety of optoelectronic devices. In PSC $MoO_x$ has been employed in p-i-n structure exhibiting PCE ~18%, whereas n-i-p $MoO_x$-based PSC presented modest efficiency <12%. This material enables the use of cost-effective metal electrodes such as Al instead of noble Au or Ag. The most studied techniques to deposit $MoO_x$ thin films in PSC are vacuum thermal evaporation and spin-coating[12,51].

*Copper based materials*

Inorganic p-type copper-based HTMs such as copper iodide (CuI), copper thiocyanate (CuSCN), copper oxide (CuO), cuprous oxide ($Cu_2O$) and so on, represent a promising family of materials which have been widely used in dye-sensitized and quantum dot solar cells. They can be fabricated in the form of thin films by several solution process techniques. Moreover, they often exhibit optimum optoelectronic properties for hole extraction purposes[12,52]. The most successful copper-based HTM in PSC are described below.

*Copper iodide (CuI)*

It is an inexpensive and stable p-type semiconductor with a large bandgap (~3.1 eV) and high hole mobility (~9 $cm^2\ V^{-1}\ s^{-1}$). CuI thin films have been fabricated by spin-coating, doctor blading, spray casting and vacuum thermal evaporation. PCE as high as 16.67% and 16.8% have been reported in n-i-p and p-i-n structures, respectively[12,27].

*Copper Oxides ($CuO_x$)*

Cupric oxide (CuO) and cuprous oxide ($Cu_2O$) are well-known p-type semiconductors. Particularly, $Cu_2O$ presents an extremely high hole mobility (~100 $cm^2\ V^{-1}\ s^{-1}$), large band gap and proper VB level around 5.4 eV. Several techniques have been employed to deposit highly crystalline $Cu_2O$ films especially in p-i-n architecture, namely, spin-coating from aqueous precursors, RF sputtering or electro spray. Accordingly, maximum PCE of ~16.8% was achieved in planar p-i-n PSC. Performance in n-i-p devices was <10% until recent reports as will be discussed later[12,38,53,54].

*Copper (I) thiocyanate (CuSCN)*

It is a good alternative for organic HTM due to high conductivity ($10^{-2}$ – $10^{-3}$ S $cm^{-1}$), high hole mobility (~0.1 $cm^2\ V^{-1}\ s^{-1}$), good transparency in solar spectrum (band gap = 3.6 eV), considerable chemical stability and it can be synthesized by simple preparation techniques[28,55–57]. Namely, spin-coating, electro-deposition, doctor blading, spray coating and drop casting. The most efficient CuSCN-based PSC have been reported in mesoscopic n-i-p architecture employing spin-coating technique reaching PCE ~20.8%. However, in the same report it was necessary to use an extra interlayer of reduced graphene oxide (r-GO) and toxic solvent[56].

Other inorganic p-type semiconductors employed in PSC such as $CuGaO_2$, $Cu_3SbS_4$, $Cu_2ZnSnS_4$, $WO_x$ and $VO_x$ have exhibited considerable efficiencies but related high cost fabrication methods reduce their suitability for large scale applications[12,27].

As said above, most of the techniques employed to fabricate high performance inorganic HTM requires high vacuum conditions, expensive equipment or strong polar solvents (for solution process techniques). Therefore, deposition of this kind of materials in n-i-p architecture (desirable for low-cost devices due to low-cost metal oxide ETM) is limited by perovskite absorber sensitivity[23,40]. Consequently, few works have been reported using this kind of HTM e.g. CuI[16], CuSCN[58], $Cu_2O$[59], CuS[60], NiO[61], graphene oxide[62], carbon nanotubes (CNTs)[63], CIGSSe nanocrystals[46] or $FeS_2$[64]. However, most of them requires high crystallization temperatures or require to be stacked with Spiro-OMeTAD to reach a relevant PCE[52,60,65]. Among the above restrictions, few interesting inorganic alternatives have appeared in literature. For example, recent investigation demonstrates a promising efficiency of ~ 16% for a mesoscopic n-i-p configuration employing CuSCN[66] which further improves to 20.2% when including reduced graphene oxide[56]. Unfortunately this material requires the use of toxic and dangerous solvents such as diethyl sulfide, highly undesirable for scaling up and industrial processes. Similar efficiencies have been also obtained for CNTs composites when they are functionalized with poly (3-hexylthiophene), yet the insertion of such organic semiconductor increases considerably the materials cost[63]. Recently, some interesting works have successfully employed copper compounds such as $CuCrO_2$ and $Cu_2O$ nanoparticles as a sole inorganic HTM in direct PSC reaching PCE around ~16.1% and ~18.9%, respectively[38,67,68]. Additionally, they highlight the importance of morphology, energy band alignment, interface interactions and surface chemistry to accomplish high performance with this kind of p-type semiconductors as HTM.

### 1.2.5. Materials cost in PSC

PV technologies are a promising alternative to replace common energy resources. However, they need to offer electricity to lower cost than traditional technologies in order to be really competitive without help of government support[30]. For instance, levelized cost of electricity produced (LCOE) from common sources as hydroelectric or coal is around 7-11 US cents/kWh, whereas LCOE of commercial silicon PV is around 19 US cents/kWh. PSC have emerged as a promising option to reduce this gap through a decrease in materials and processes cost[69]. Some works reports the materials cost distribution in typical PSC. Interestingly, as shown in **Figure 1.8** TCO is the major contributor to device cost representing more than 50%. Also, the same work reports that both high PCE and stability are key factors to decrease LCOE of PSC. Specifically, PCE of modules >12% and >15 years of operation are desirable to achieve commercial competitive PSC[6].

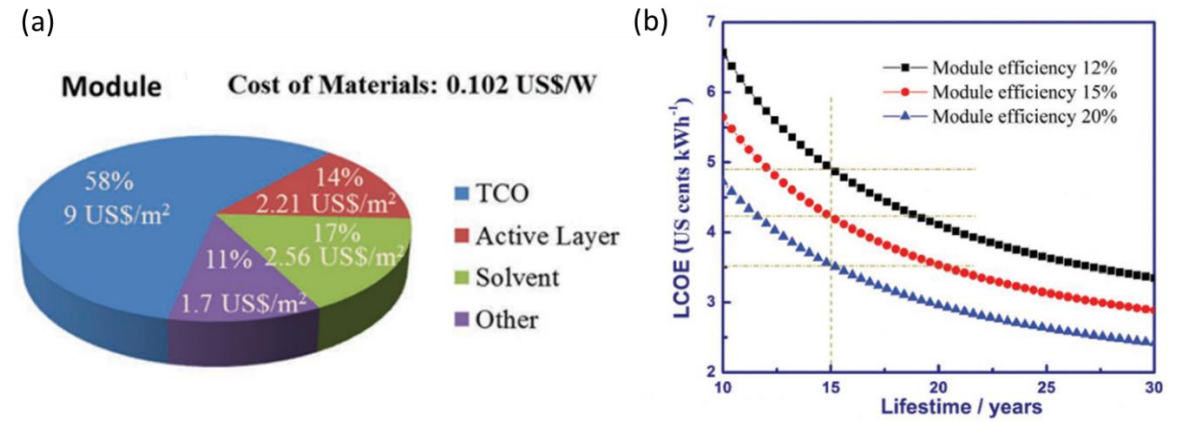


**Figure 1.8.** (a) Cost of materials involved in PSC fabrication. (b) Estimated LCOE of PSC modules with different efficiencies and lifetimes. Figure re-drawn based on Ref[6].

## 1.3. Thesis synopsis

### 1.3.1. Aim of the thesis

Perovskite solar cells are the most promising third generation PV technology, a technology that could replace non-renewable electricity sources. However, device cost and stability remain as bottlenecks to reach a realistic commercialization point. Although, intense and fruitful research has been developed on improving these issues from perovskite absorber point of view, stability associated to charge transporting layers, especially HTM, is still a major challenge. High performance inorganic HTM seem to be a promising alternative for cost-effective and ambient stable hole selective contacts. However, deposition conditions and techniques are limited by perovskite sensitivity to moisture and high temperatures. In addition, TCO still represents the biggest contributor to PSC materials cost so that reduction of TCO cost should have a tremendous influence on PSC LCOE. Although notable progress has been made today in new TCO and inorganic HTM, still there are challenges implementing these materials to get devices with decent performance. Accordingly, the aim of the work described in this thesis was to synthesize and apply some earth-abundant inorganic p-type semiconductor which had not been previously employed in PSC. The goal was to develop and optimize synthetic routes for proper precursors of these materials in order to fabricate corresponding thin films. Subsequently, solution process methods were employed to incorporate these materials in different PSC architectures. Moreover, the effect of each new material on device performance was evaluated and studied by different characterization techniques as well as their effect on stability.

### 1.3.2. Outline of the thesis

The second chapter described the synthesis of copper sulfide ($Cu_xS$) thin films on glass by spray pyrolysis technique. Optoelectronic properties of $Cu_xS$ films were evaluated as function of thickness. Subsequently, $Cu_xS$ films on glass were employed as TCO in an ITO-free HTM-free p-i-n PSC architecture. Effect of films thickness on device photovoltaic parameters was studied as well as its influence on perovskite absorber electronic properties. Finally, materials cost including the proposed electrode was estimated.

Third chapter shows the synthesis and characterization of copper sulfide nanoparticles (CuS NPs) as a promising p-type semiconductor. The suitability of CuS NPs as HTM was evaluated in a mesoscopic n-i-p PSC structure. This material was applied by spin-coating technique starting from appropriated colloidal precursor. Influence of deposition parameters on device performance was observed. HTM optoelectronic properties were studied and correlated with PSC behavior by different characterization techniques.

Chapter fourth described the synthesis and surface modification of nickel oxide nanocrystals ($NiO_x$ NCs). This material was applied as HTM in a planar n-i-p PSC structure by spin-coating technique and the effect of its thickness on device performance was also evaluated. Moreover, similar to CuS NPs, $NiO_x$ optoelectronic properties were measured and their influence on PSC behavior and stability was studied.

Fifth chapter describes materials, experimental procedures and characterization techniques employed through this thesis, sixth chapter provides some additional characterization of materials and devices in order to complement the results showed in previous chapters. Finally, seventh chapter summarizes main findings and

provides guidelines for future works employing the materials developed in this thesis.

# Chapter 2. Low-cost semi-transparent copper sulfide electrode for indium-tin-oxide-HTM free perovskite solar cells.

This chapter is based on published work: Tirado et al. Thin Solid Films 2018, 662, 90–96. DOI: 10.1016/j.tsf.2018.07.037.

## 2.1. Introduction

During the last decade a variety of PSCs structures have been developed, including planar regular (n-i-p) and inverted (p-i-n) heterojunction cells and their mesoporous counterparts using $TiO_2$ or $Al_2O_3$ scaffolds [22,70–72]. In particular, the inverted structure has gained a broad interest in the photovoltaic community by enabling the device processing in solution at low temperature [25,73]. Moreover, the inverted configuration potentially suppresses the use of expensive and unstable hole-transporting-materials (HTM) by taking advantage of the relatively high hole-mobility of the perovskite [74]. Both inverted and direct PSCs structures require the use of transparent conductive electrodes (TCE) which have been identified as the biggest contributors to the total materials cost of the cells [69]. In that direction, the widely used ITO presents several issues such as indium scarcity and toxicity, mechanical fragility and high processing temperature (>300 °C)[73,75–79]. On the other hand, the advent during the last decade of active transparent electronic components and related devices made apparent the need of obtaining p-type TCEs with high optical transparency and high conductivity. The common approach based on transparent conductive oxides (TCO) has found many challenges principally due to the difficulty in achieving shallow acceptors and large hole effective masses [80,81]. To date, graphene has demonstrated to be the best p-type TCE. Several groups have reached PCEs as high as 17.1% by including a $MoO_3$-doped graphene electrode [82,83]. However, the

morphological and functionality of the graphene electrode strongly depend on the fabrication conditions [84,85] in addition to the well-known difficulties in scaling up the graphene technology to large area devices [86]. Another alternative relies on a highly conductive PEDOT:PSS electrode reaching up to 12% PCE [87,88]. However, the acidity and hygroscopicity of the PEDOT:PSS layer represent a source of degradation limiting its application [86].

On the other hand, new earth-abundant materials with proper optoelectronic properties have the potential to achieve scalable solution processes contributing to the development of the PSCs field. Among these, the p-type semiconducting copper sulfide chalcogenide represents one of the most promising materials for future sustainable energy supply due its low cost, environmental friendliness and its particular physical and chemical properties such as metal-like conductivity, high carrier mobility, high catalytic activity, non-toxicity and excellent chemical stability [89–92]. Moreover, a variety of deposition techniques have been used to grow copper sulfide thin layers such as spin-coating, spray pyrolysis, hydrothermal deposition, sputtering and chemical bath deposition [93–97]. For these reasons, different copper sulfide crystal phases have been included as functional materials in several electronic and optoelectronic devices including supercapacitors [98], LEDS [99], lithium rechargeable batteries [100] and solar cells [89]. Indeed, copper sulfide has been effectively employed as TCE in quantum-dots solar cells [101] and resistive touch-screen devices [102] while surprisingly it has not been considered in PSCs.

Thus, ITO-free and HTM-free inverted-planar PSCs was achieved by implementing a copper sulfide ($Cu_xS$) semi-transparent electrode. Herein, it is reported for the first time the use of copper sulfide as TCE in a PSCs structure. The novel semi-transparent electrode was obtained in-situ by a solution-based spray pyrolysis process.

## 2.2. Copper sulfide thin films fabrication and basic characterization

Copper sulfide thin films were fabricated by spray pyrolysis technique. In brief, this process involves three steps and it is illustrated in **Figure 2.1a** (See chapter 5 for experimental details). First, a precursor solution with proper metal salts and additives is atomized by one of three possible systems: air blast, ultrasonic and electrostatic atomizer. Second, formed droplets are transported as an aerosol through the air towards a heated surface. Third, decomposition or reaction between reagents present in precursor solution occurs on substrate surface promoted by solvent evaporation. Parameters that control this process are substrate temperature, precursor concentration, precursor chemistry and operational variables such as gas pressure (influencing droplet properties), nuzzle-substrate distance and deposition time[95,103]. Following an optimization study developed by Adelifard et al.[104] it was found the right conditions to deposit homogenous layers of copper sulfide on glass substrates. Namely, a nuzzle-substrate distance of 20 cm and air pressure of 40 psi were determined as the best operational parameters (See chapter 5 for details). Subsequently, an in-house equipment (**Figure 2.1b**) was used to sequentially deposit different copper sulfide layers (called cycles) and study the effect of different cycles on films and PSC properties. Initially, X-ray diffraction (XRD) was used to assess the crystalline phase of the synthesized material. The resulting $Cu_xS$ electrode was formed by covellite (CuS) and digenite ($Cu_{1.8}S$) phases, while its surface properties strongly depended on the deposition conditions. The diffraction pattern shown in **Figure 3a** presents peaks at $2\theta$ = 27.85°, 29.46°, 31.98°, 48.26° and 59.71° corresponding to the (101), (102), (103), (110) and (116) diffraction planes of copper sulfide covellite phase (CuS), respectively [105]. In addition, the peak at $2\theta$ = 46.53° is related to the (220) diffraction plane of the copper sulfide digenite phase ($Cu_{1.8}S$) [89]. Accordingly, the fabricated films, referred as $Cu_xS$ are a mixture of two copper

sulfide phases with a mass composition of 86% covellite and 14% digenite as estimated using the reference intensity ratio (RIR) method from the XRD pattern in **Figure 2.1c**. This in agreement with Cu:S atomic ratio of 1.04:1 obtained by EDS analysis (**Figure A1**, Appendix section) Additionally, analysis of the major peaks from plane (101) and (102) of covellite phase allowed us to calculate the crystallite size by employing the Scherrer equation, giving 8.3 nm and 9.7 nm, respectively. Moreover, calculated optical band gap in **Figure 2.1d** around 2.7 eV is consequent with values reported for a range copper sulfide crystal phases[99].

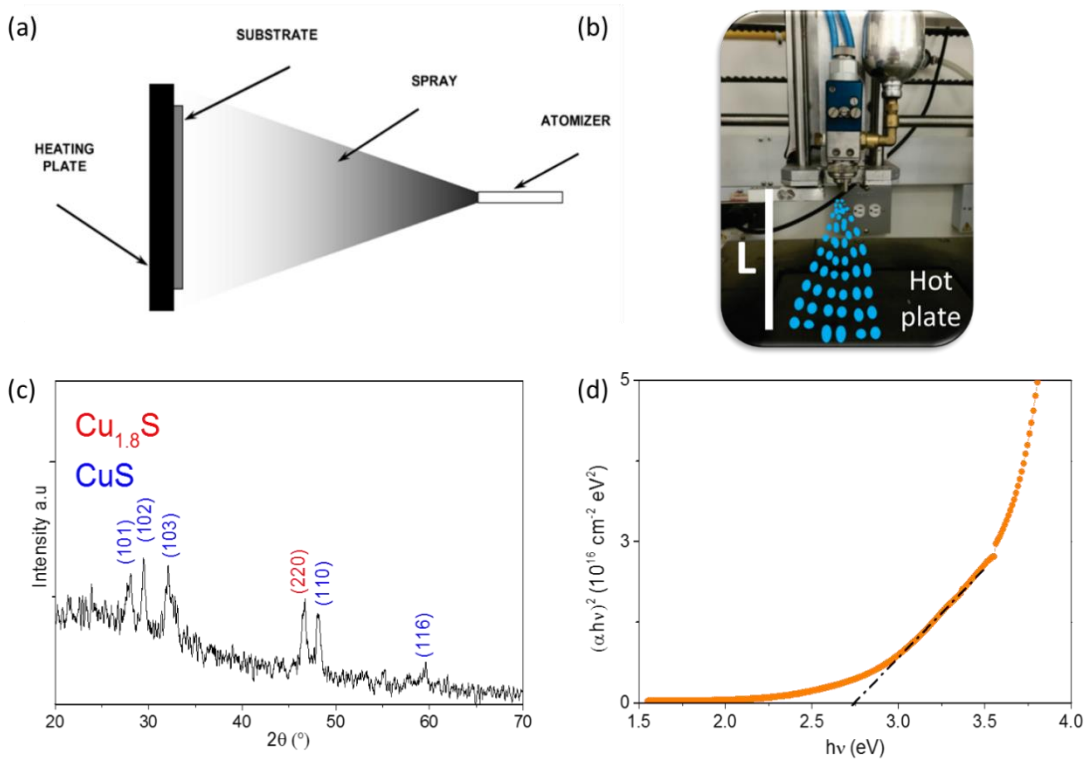


**Figure 2.1.** (a) Scheme of spray pyrolysis system taken from reference[103]. (b) In-house spray coater employed to fabricate $Cu_xS$ thin films. (c) XRD pattern revealing covellite and digenite phases in $Cu_xS$ electrode on glass substrate. (d) Estimated optical band gap of CuxS films.

As expected, thickness and roughness of the $Cu_xS$ films strongly depended on the spray pyrolysis parameters. In fact, as shown in **Figure 2.2a**, average film thicknesses (δ) of 38, 51, 63 and 82 nm were obtained with 4, 5, 6 and 7 spray cycles, respectively.

The growing trend is almost linear which is expected for this particular film deposition process. In addition, Atomic Force Microscopy (AFM) was employed for revealing the topography characteristics of the fabricated films. **Figure 2.2b** shows 3D AFM images of films deposited with 4 to 7 spray cycles. In all cases, a 40-80 nm particle size was found. Interestingly, the growth of particles clusters was apparent and dependent on δ, starting from some small aggregates for δ = 38 nm to big clusters of around 500 nm wide and 40 nm high for δ = 82 nm (see also SEM images of Figure A2, Appendix). This topography characteristic explains the surface roughness ($R_{ms}$) increasing with film thickness from 5.7 nm at δ = 38 nm up to 28.3 nm at δ = 82 nm.

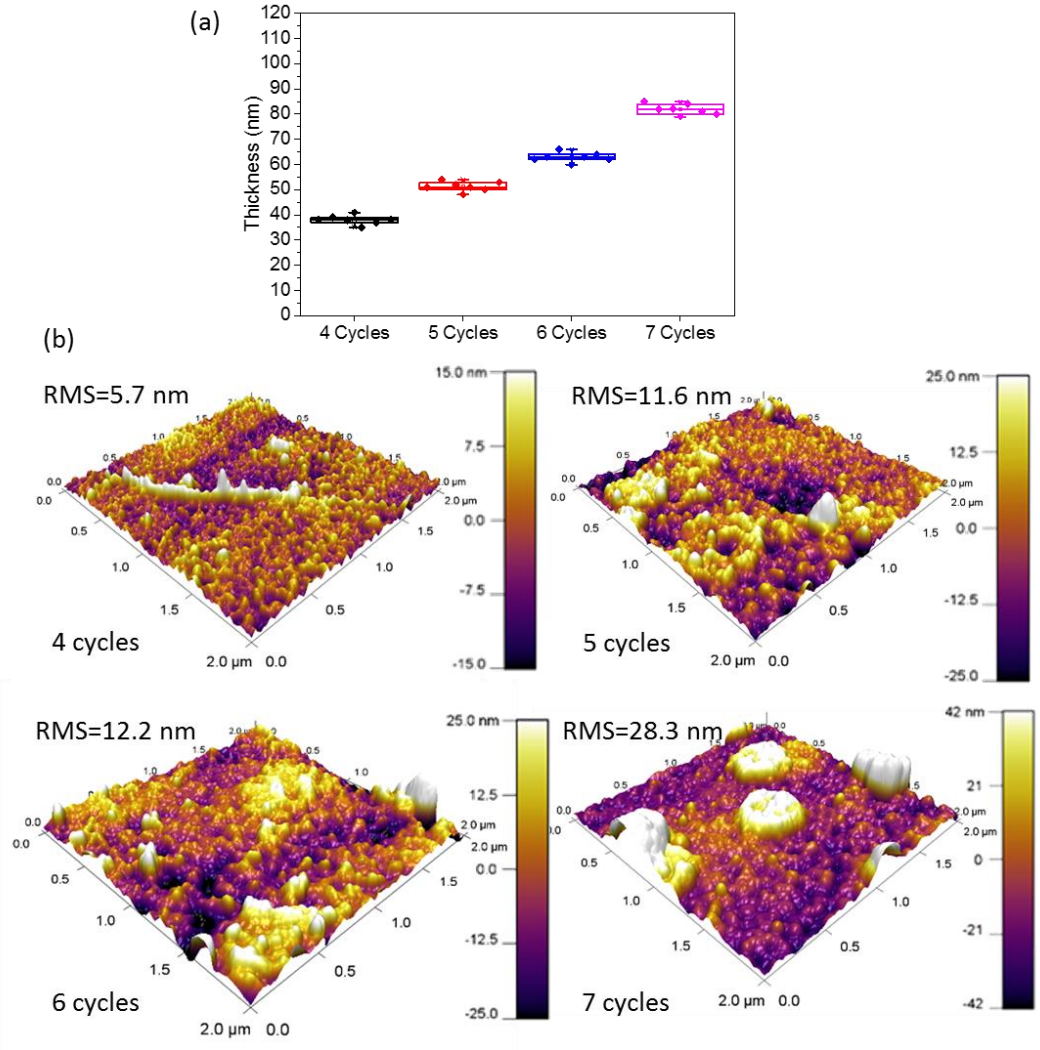

**Figure 2.2.** Morphological analysis of $Cu_xS$ electrode. (a) Dependence of films thickness related to deposition cycles. (b) 3D AFM images of $Cu_xS$ films showing corresponding roughness ($R_{ms}$).

The optoelectronic characterization of the resulting $Cu_xS$ films revealed a semiconductor exhibiting high conductivity (**Figure 2.3a**) and low sheet resistance ($R_{sq}$). Remarkably, a top value of 1094 S $cm^{-1}$ was obtained which was in the same order of other high performance TCEs [87]. Also, $Cu_xS$ films presented a moderate average optical transmittance since some optical absorption was observed especially in the blue region below 500 nm which is coherent with calculated optical bandgap (See **Figure 2.3b**) ($T_{avg}$, determined in the range 300-800 nm).

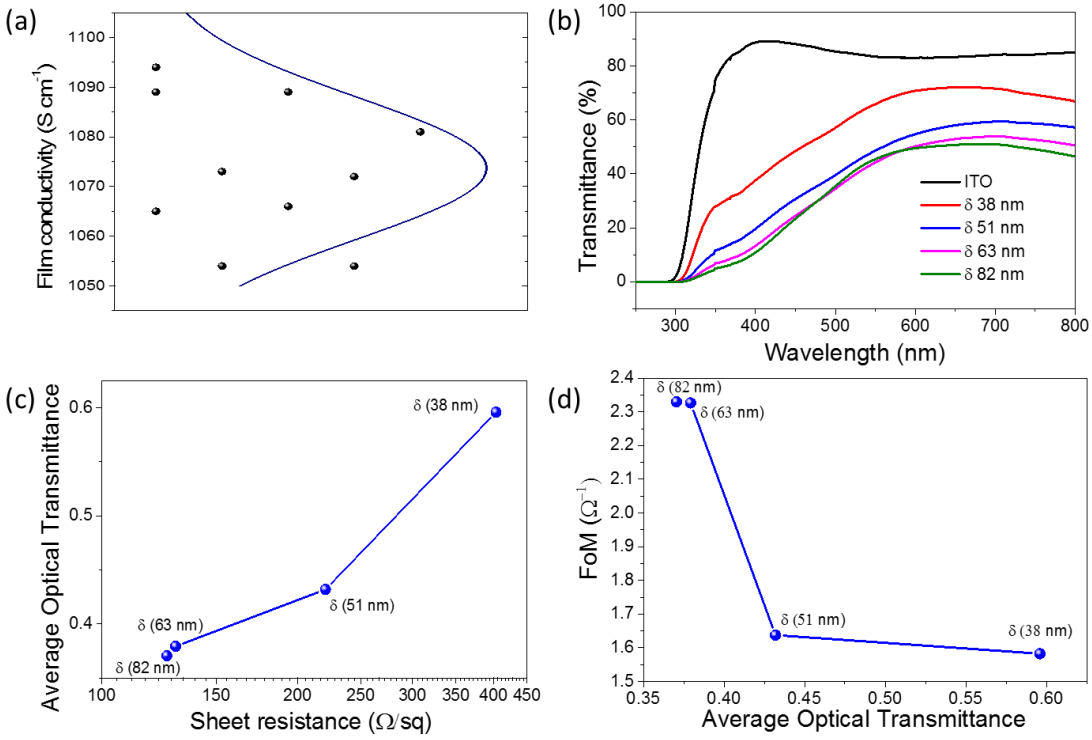


**Figure 2.3.** Optoelectronic characterization of fabricated $Cu_xS$ thin films. (a) Conductivity of layer deposited on glass. (b) Absorption spectra of $Cu_xS$ with different thickness and reference ITO. (c) Correlation between the average optical transmittance, layer thickness (δ) and sheet-resistance (Rsq) of the $Cu_xS$ films. (d) Figure-of-Merit of the proposed semi-transparent electrode.

As shown in **Figure 2.2c**, the $T_{avg}$ and the $R_{sq}$ relate inversely similar to other semi-transparent electrodes. In order to find the optimal ratio between electrical and optical conductivity of fabricated films, closely dependent on the $Cu_xS$ layer thickness, the electrical to optical conductivity ratio was employed as Figure-of-Merit (FoM) relating $T_{avg}$ and $R_{sq}$ [106] following the trend shown in **Figure 2.2c**. The FoM increases with δ reaching a maximum value of 2.36 $\Omega^{-1}$ at δ=82 nm. Therefore, the latter suggests that the thickest fabricated $Cu_xS$ film should present the best performance as semi-transparent electrode.

### 2.3. Perovskite solar cells employing copper sulfide as electrode

Copper sulfide ($Cu_xS$) was employed as semi-transparent electrode in hole-transporting-material-free planar perovskite solar cells. As shown in **Figure 2.4a** and **Figure 2.4b** $Cu_xS$ replaced ITO in this developed PSC forming a p-i-n structure according to the provided energy band diagrams obtained from reference values[42,107]. The best device obtained with this novel structure reached a PCE of 5.9%. **Figure 2.5** and **Table 2.1** summarize the obtained photovoltaic parameters. After varying the $Cu_xS$ thickness (δ) from 32 to 82 nm, the PCE increased from 2.5 ± 0.5% to 4.3 ± 1.0%, correspondingly. As comparison, a hole-transport-layer free ITO-based reference device was fabricated reaching a 6.9 ± 1.1% PCE. Remarkably, both optimal $Cu_xS$ and ITO based devices exhibit relatively close PCE values.

Although $Cu_xS$-based cells present low $V_{oc}$, their PCE is compensated by an impressive *FF* reaching up to 81% as shown in **Figure 2.5a**. On the other hand, the obtained $J_{sc}$ is just slightly less for $Cu_xS$-based devices than for ITO-based ones. This similitude is explained from the EQE response of the devices (**Figure 2.5b**). Overall, $Cu_xS$-based devices present a low EQE response in the range below 500 nm which is consequent with the calculated optical band gap of the material (**Figure 2.2d**) but they reach values comparable to the ones achieved by ITO-devices in the rest of the

sunlight spectrum. Since blue and UV light makes up a small part of the total photon flux [4,108], the resulting optical loss between 300 and 500 nm leads to a $J_{sc}$ reduction below 10%. In addition, maximum EQE for both reference and $Cu_xS$-based devices was around 60%. The latter indicates that there are some losses during the photovoltaic process but the effect on the final behavior is very similar in all evaluated cases which suggests that defects density in the $Cu_xS$ bulk[109,110] is low enough to allow a hole transfer at least as efficient as in ITO. According to this idea, device performance could be improved by finding the way to reduce $Cu_xS$ bulk defects during the spray pyrolysis fabrication process.

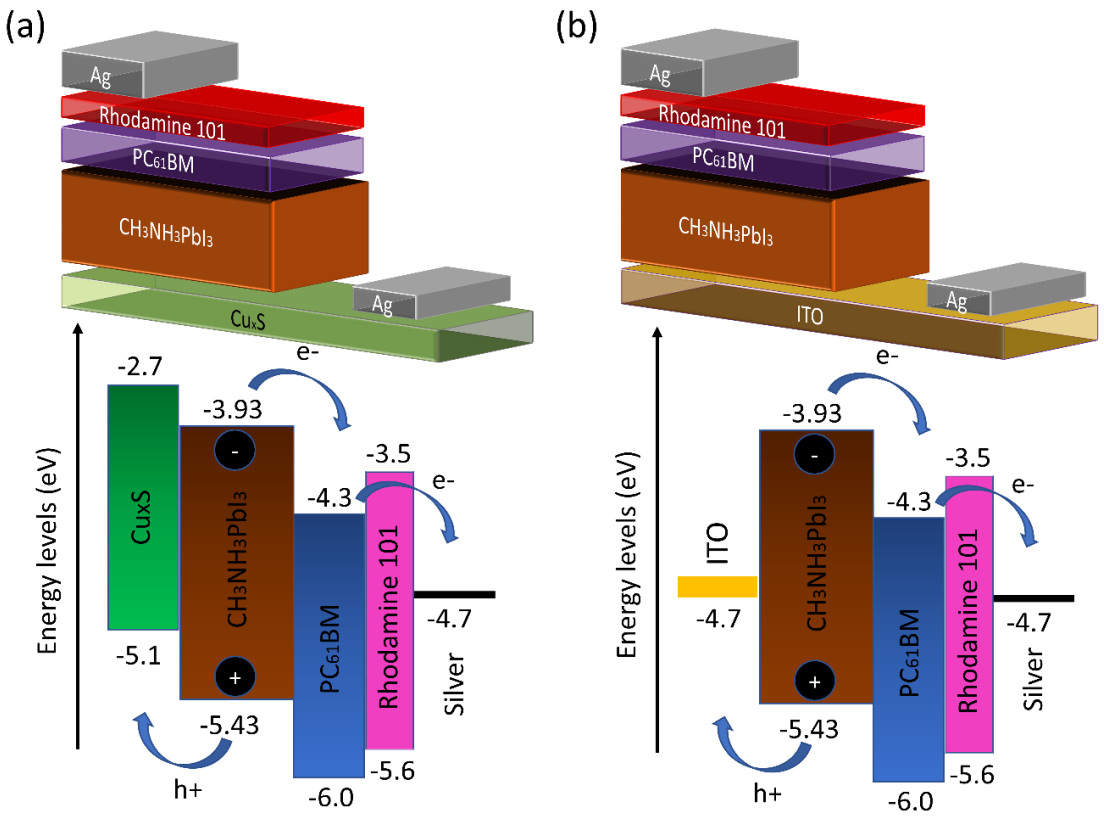


**Figure 2.4.** (a) Structure of the p-i-n hole-transporting-material-free PSC including $Cu_xS$ as semi-transparent electrode and corresponding energy band diagram. (b) Structure of reference hole-transporting-layer free PSC employing ITO as electrode and corresponding energy band diagram.

**Table 2.1** shows forward and reverse photovoltaic parameters of analyzed devices. A considerable hysteresis was observed in $Cu_xS$-based PSCs therefore a stabilized power output measure (SPO) of the best $Cu_xS$ PSC was performed as a more trustworthy measurement of the device PCE. In **Figure 2.2c** the SPO of 82 nm- $Cu_xS$ PSC is shown at maximum power output point (Voltage = 0.49 V) where a stabilized PCE of 4.6% was obtained.

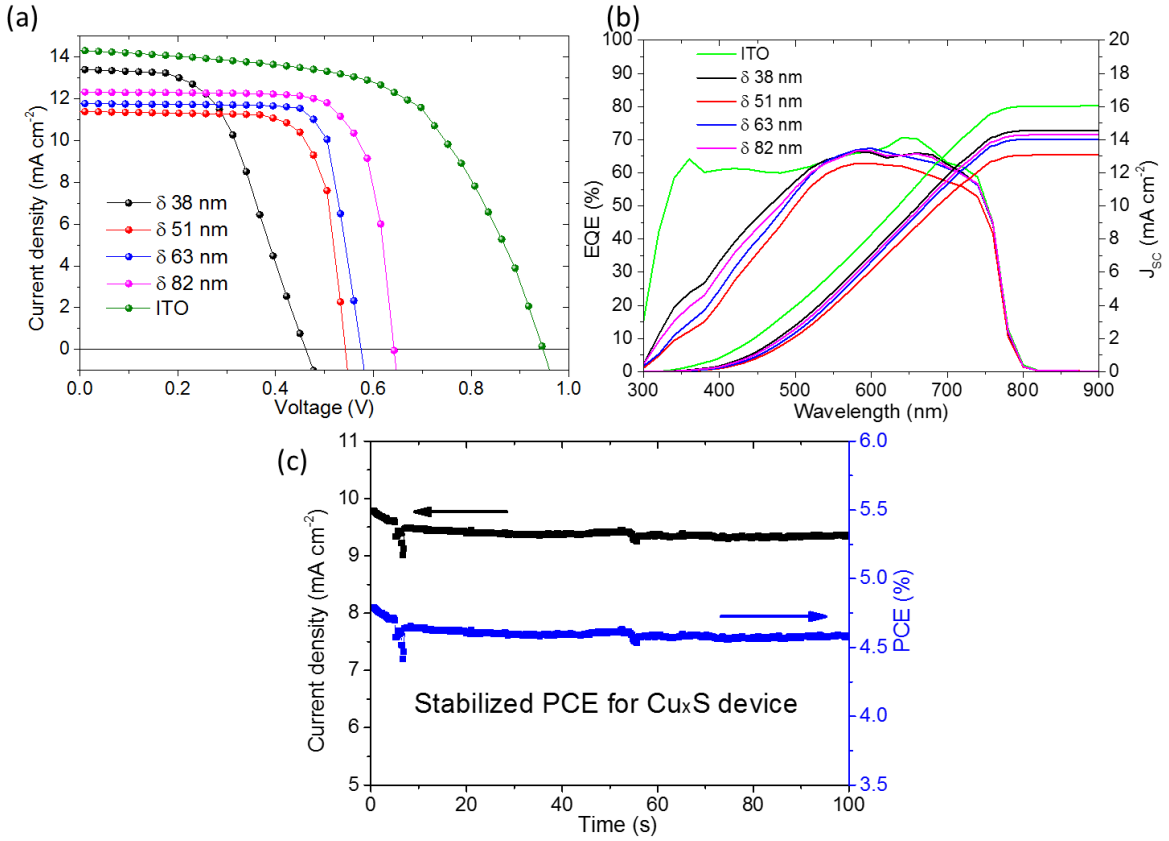


**Figure 2.5.** Summary of photovoltaic parameters obtained with our proposed PSC structure. (a) J-V curves of best devices. (b) EQE response and integrated $J_{sc}$. (c) Stabilized PCE and $J_{sc}$ of PSC with 82 nm-$Cu_xS$ electrode.

The effect of $Cu_xS$ films topography on device performance was analyzed by AFM. The relatively high $R_{ms}$ of the $Cu_xS$ did not prevent obtaining high quality perovskite films as can be seen in **Figure 2.6**. In fact, perovskite topography when ITO and $Cu_xS$ are employed as TCEs was very similar. Thus, from the morphology point of view,

it is not expected a negative effect of $Cu_xS$ on the device performance. As shown elsewhere, high performance planar inverted devices have been achieved with high roughness electrodes [25]. In fact, some authors claim that surface roughness can promote good perovskite crystallization [111] and surface coverage [112].

**Table 2.1.** Photovoltaic parameters of the $Cu_xS$ and ITO based PSCs. Best PCE is presented in parenthesis.

| **Electrode** | **Sweep Direction** | **$J_{sc}$ (mA cm$^{-2}$)** | **$V_{oc}$ (V)** | **FF (%)** | **PCE (%)** |
|---|---|---|---|---|---|
| $Cu_xS$ 38 nm | $J_{sc}$ to $V_{oc}$ | 11.7 ± 1.0 | 0.39 ± 0.07 | 54.9 ± 6.6 | 2.5 ± 0.5 (3.3) |
| | $V_{oc}$ to $J_{sc}$ | 11.5 ± 0.9 | 0.28 ± 0.08 | 38.7 ± 5.2 | 1.3 ± 0.6 |
| $Cu_xS$ 51 nm | $J_{sc}$ to $V_{oc}$ | 11.1 ± 0.6 | 0.42 ± 0.09 | 75.2 ± 8.3 | 3.6 ± 1.0 (4.7) |
| | $V_{oc}$ to $J_{sc}$ | 10.9 ±0.6 | 0.26 ± 0.03 | 40.8 ± 7.7 | 1.2 ± 0.3 |
| $Cu_xS$ 63 nm | $J_{sc}$ to $V_{oc}$ | 12.0 ± 0.8 | 0.49 ± 0.09 | 70.9 ± 5.2 | 4.2 ± 0.7 (5.3) |
| | $V_{oc}$ to $J_{sc}$ | 11.9 ± 0.6 | 0.31 ± 0.07 | 46.8 ± 9.3 | 1.8 ± 0.6 |
| $Cu_xS$ 82 nm | $J_{sc}$ to $V_{oc}$ | 11.7 ± 0.8 | 0.53 ± 0.08 | 69.9 ± 10.1 | 4.3 ± 1.0 (5.9) |
| | $V_{oc}$ to $J_{sc}$ | 11.7 ± 0.8 | 0.34 ± 0.04 | 47.1 ± 4.7 | 1.9 ± 0.3 |
| ITO | Both | 13.2 ± 0.9 | 0.92 ± 0.08 | 56.7 ± 3.8 | 6.9 ± 1.1 (8.0) |

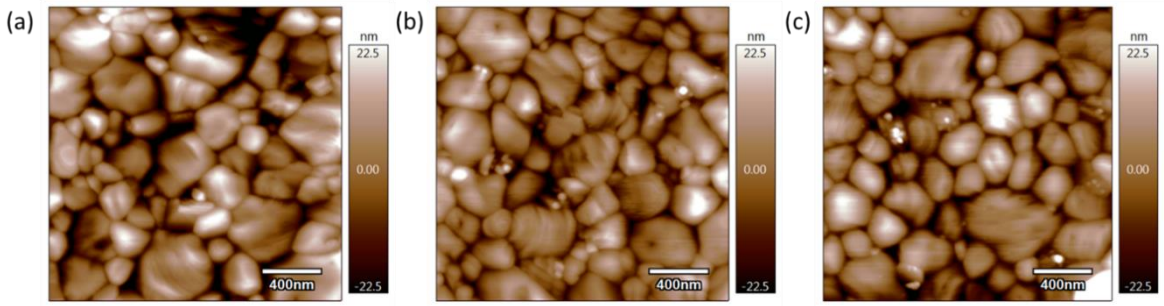


**Figure 2.6.** AFM topography of $CH_3NH_3PbI_3$ perovskite surface grown on (a) ITO, (b) 4 cycles $Cu_xS$ and (c) 7 cycles $Cu_xS$.

Additionally, the effect of the $Cu_xS$ films on the perovskite growing was addressed from KPFM analysis. As shown in **Figure 2.7a**, perovskite surface showed a negative SPV indicating a superficial n-type behavior which is ideal in p-i-n PSCs. Moreover, work functions of $Cu_xS$ and perovskite growing on it (see **Figure 2.7b**), at dark and different illuminations, are closer each other than the work function of ITO and ITO/perovskite, indicating that there is a better band alignment when $Cu_xS$ is used as TCE. However, in the evaluated illumination range, the SPV curve for perovskite grown on $Cu_xS$ did not reach the saturation regime, meanwhile the curve using ITO as electrode effectively did it. The latter suggests that perovskite grown on $Cu_xS$ still presents surface unsaturated trap states when illuminated which might explains the low $V_{oc}$ (see **Table 2.1**) achieved in the $Cu_xS$-based PSCs compared to the ITO-based counterparts [113,114]. These findings open room for further improvement employing $Cu_xS$ as TCE after better controlling the perovskite film formation.

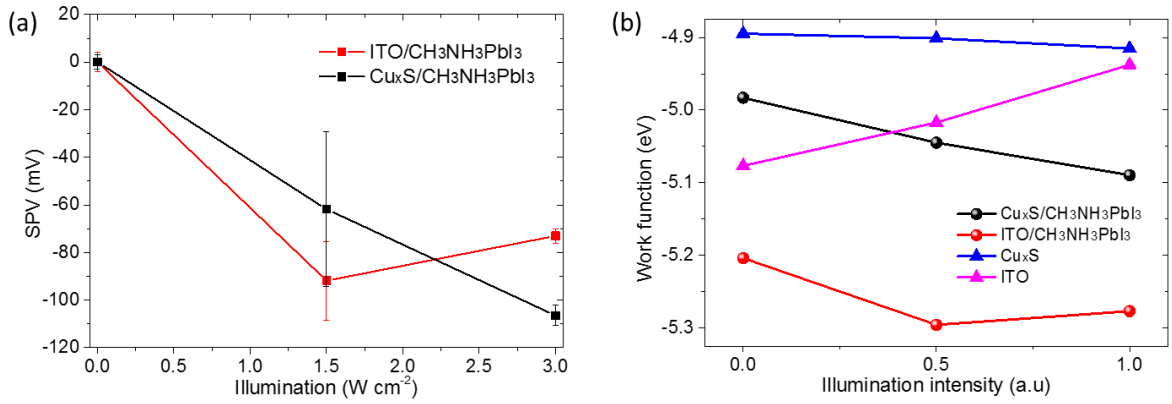


**Figure 2.7.** Kelvin probe force microscopy analysis (KPFM). (a) Surface photovoltage of perovskite grown on $Cu_xS$ and ITO. (b) Surface work function of $Cu_xS$, ITO, and perovskite grown on each TCE.

Finally, since the presented $Cu_xS$ is fabricated from earth abundant and by a low cost and scalable deposition technique, the total cost of this material is expected to be much lower than typical semi-transparent electrodes such as ITO. Commercially, ITO is fabricated at large-scale mainly using sputtering. Spray coating has also been recognized to have potential as scalable processing method since its compatibility with roll-to-roll processing and capability for developing patterns. Based on the materials used in the $Cu_xS$ spray deposition and their cost at lab-scale, the cost of $Cu_xS$ TCE per square meter was estimated to be around 2.02 US$/m$^2$ (see **Figure 2.8**). This is a lab-scale cost which that can be unfairly compared to the large-scale cost reported for ITO at 9 US$/m$^2$ [69]; however this comparison represents a minimum cost reduction of 77.6% which has room to be higher after successfully implementing the spray coating of TCOs at large-scale. These findings demonstrate the potential of the $Cu_xS$ film as a promising low-cost alternative to ITO for inverted planar PSCs opening also a route for application in other optoelectronic devices relevant well beyond the materials community.

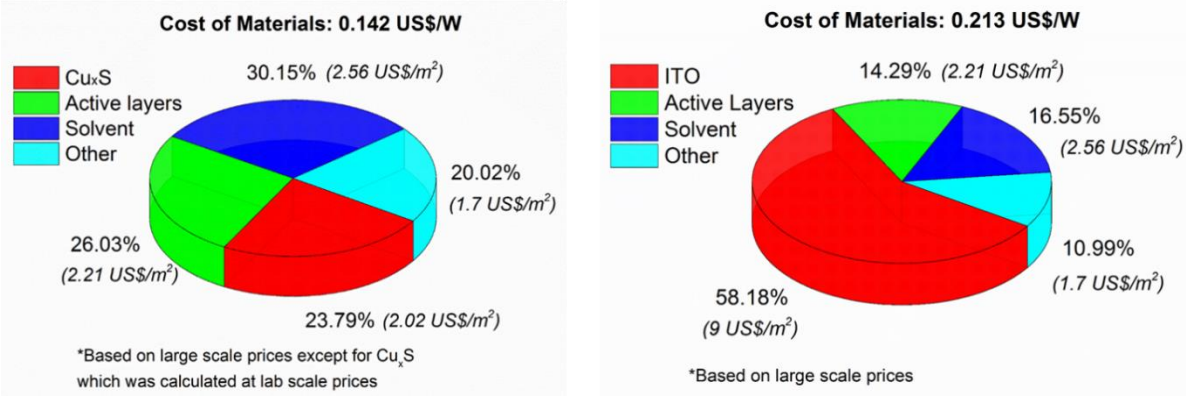


**Figure 2.8.** Materials cost estimation for PSC employing $Cu_xS$ (Left) and ITO (Right) as electrode.

## 2.4. Conclusions

In summary, I have presented a novel implementation of copper sulfide ($Cu_xS$) in p-i-n perovskite solar cells with double functionality as semi-transparent electrode and hole transporting material. Resulting ITO-free and hole-transporting-material-free perovskite solar cells reached an unprecedented 5.96% efficiency. Compositionally, the $Cu_xS$ films were formed by covellite (CuS) and digenite ($Cu_{1.8}S$) phases exhibiting 40-80 nm particles grouped in clusters. In addition, the $Cu_xS$ electrodes exhibited a high 1094 S $cm^{-1}$ electrical conductivity, comparable to commercial TCEs, and a 2.7 eV optical band gap. This relatively low bandgap leads to a blue-optical-loss affecting reducing less than 10% the obtained photocurrent since blue and UV light makes up a very small part of the total solar radiation. According to the used semi-transparent electrode Figure-of-Merit, an 82 nm thick $Cu_xS$ film corresponded to the optimal $Cu_xS$ thickness leading to the best performing device. In addition, surface photovoltage analysis suggests that the perovskite grown on the $Cu_xS$ film exhibits an n-type behaviour which is optimal in the p-i-n PSC configuration. Additionally, there is a better band alignment between perovskite and TCE when $Cu_xS$ is employed. However, surface trap states

seem to be favoured by $Cu_xS$ regarding to ITO which might be the reason $Cu_xS$-based PSCs present a relative low $V_{oc}$. However, the latter indicates that photovoltaic behaviour of $Cu_xS$-based PSCs can be still improved by a better perovskite growing control which can promotes further works out of the scope of this work. Finally, it is determined that $Cu_xS$ as TCE represents a 77.6% reduction total material cost per square meter (US$/m$^2$) compared to commercial ITO. These properties, in addition to the scalability of the spray pyrolysis processing, highlight the potential application of $Cu_xS$ films in achieving low-cost perovskite solar cells and other related optoelectronic devices.

# Chapter 3. Copper sulfide nanoparticles as hole-transporting-material in fully-inorganic blocking layers n-i-p perovskite solar cells: Application and working insights.

This chapter is based on published work: Tirado et al. Appl. Surf. Sci. 2019, 478, 607–614. DOI:10.1016/j.apsusc.2019.01.289.

## 3.1. Introduction.

Earth abundant and extremely cheap copper sulfide derivatives ($Cu_{2-x}S$, $0>x>1$) represent an interesting class of p-type semiconductors with tunable optical properties and high charge-transport mobility, conductivity and chemical stability[90,115]. Among the different stable phases with variable Cu:S ratio, covellite (CuS) presents the highest concentration of valence-band-delocalized holes, resulting in an unusual p-type metallic-like character with dual semiconductor-plasmonic nature[116]. Due to such electronic properties, CuS has been successfully employed for different optoelectronic applications, including the tuning of the ITO work function[97], or the passivation of the HTM/metal interface via CuS sublimation[60]. Moreover, CuS behaves as inorganic barrier against environmental moisture[60], which could prevent perovskite materials from degradation. However, despite all these benefits, CuS has not been yet employed as a sole inorganic HTM, mainly due to the lack of precursor solutions compatible with the perovskite material[117]. In addition, CuS synthesis normally require the use of high temperatures (200-500ºC)[118,119] or highly toxic materials, and due to its narrow thermodynamic stability domain, its selective growth can be more restrictive compared to other phases, hindering its fabrication[120].

In this chapter, I present the synthesis and characterization of stable CuS nanoparticles (CuS NPs) suitable for being used as low-cost HTMs. The colloidal dispersion can be stabilized in non-polar and halogen-free solvents that are fully compatible with the perovskite layer, extending its application to either the p-i-n or n-i-p cell configuration. In addition, such versatility is combined with a low-temperature solution based fabrication method which is fully scalable to printing role-to-role (R2R) and large scale industrial processes. By using this facile approach, It is presented here a first demonstration of PSCs with n-i-p device configuration based on CuS NPs, which leads to short circuit currents ($J_{sc}$) and fill factor (FF) values comparable to the state-of-the-art devices ($J_{sc} > 20$ mA·cm$^{-2}$; $FF > 0.7$). Moreover, CuS behavior as HTM was investigated the by UPS, XPS and PL measurements.

### 3.2. Copper sulfide nanoparticles synthesis and characterization.

The CuS nanocrystals were prepared by using a modified version of the synthesis reported by Zhang et al[121], in order to achieve a stable and high concentrated dispersion in non-polar solvents. In brief, it wasprepared two separated precursor solutions containing sulfur powder and copper chloride respectively, both dissolved in oleylamine which acts as ligand, solvent and reductant agent. The latter was first heated to 150°C and then sulfur was rapidly added, completing the reaction after only few minutes. CuS nanoparticles were then collected from centrifugation and dispersed in toluene. The detailed crystal analysis and size-morphology are shown in **Figure 3.1**. The X-Ray diffraction (XRD) pattern of the as prepared material deposited by drop casting is presented in **Figure 3.1a**. In agreement with previous works, these results demonstrate several diffraction peaks at 27.21°, 29.36°, 32.35°, 33.52°, 48.09°, 52.33° and 59.05° corresponding to the hexagonal CuS phase previously reported in literature[92]. No additional peaks related to other $Cu_{2-x}S$ phases were further detected, suggesting a pure CuS phase with a 1:1 stoichiometry.

Moreover, in agreement with previous works, our CuS material also exhibits an optical band gap around 2.4 eV[104,122] and a single, intense extinction band at NIR wavelengths (> 900 nm) (see **Figure 3.1b**). Such a behavior has been well documented in CuS nanocrystals, revealing its characteristic plasmonic-semiconductor dual nature. **Figure 3c** shows the size-morphology of the crystalline nanoparticles observed by electron transmission microscopy (TEM). As observed in the TEM-images, the nanocrystals exhibit a 2D disk-like shape with a maximum size of 20 nm and a thickness around 4 nm, closely resembling those previously obtained through water-based synthetic strategies[121].

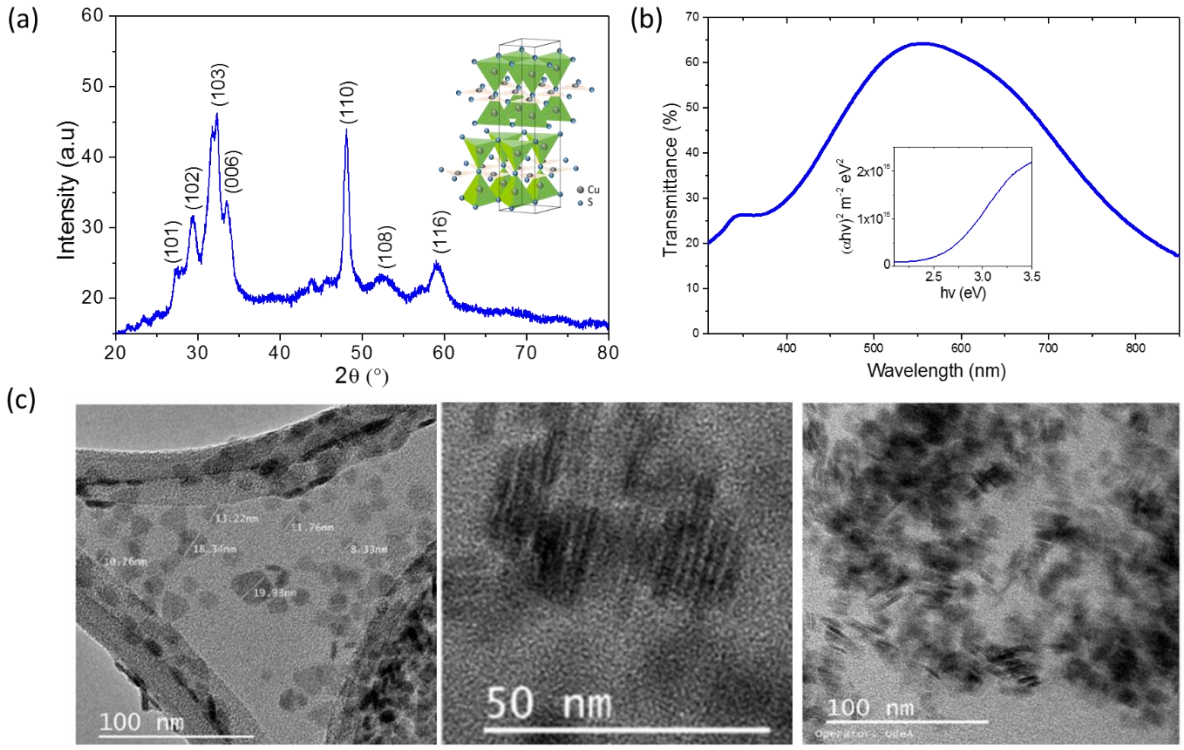


**Figure 3.1.** (a) XRD difractogram of dried CuS nanoparticles showing the characteristic peaks of covellite copper sulfide. Inset: scheme of crystal structure. (b) Transmittance spectrum of a CuS film deposited on glass and band gap estimation (inset). (c) TEM image showing the flake-like shape of CuS nanoparticles.

In addition, two intense Raman active phonon modes around 60 and 475 $cm^{-1}$ are expected for covellite phase, which can be easily detected in the as prepared sample, shown in **Figure 3.2a** and **Figure 3.b**.[115] The peaks, assigned to the stretching vibrational modes of S-S covalent bonds[123], provide additional support to the formation of CuS. Moreover, FTIR of as prepared CuS nanoparticles in **Figure 3.1c** shows characteristic peaks of C-H stretching of $–CH_2$ (2908 and 2995 $cm^{-1}$), C-N stretching vibration (1240 $cm^{-1}$) and typical CuS absorption at 603 $cm^{-1}$ which again confirms the presence of covellite copper sulfide and, most important, the existence of alkyl chains at material surface which is expected due to nanoparticles stabilized with oleyamine[121,124]. To verify the exact chemical composition X-Ray photoelectron spectroscopy (XPS) measurements were developed. **Figure 3.3a** reports the core level spectrum of Cu 2p and S 2p obtained for the thin films deposited on FTO. As observed, the Cu $2p_{3/2}$, S $2p_{1/2}$ and S $2p_{3/2}$ bands located at 932.8 eV, 162.59 eV and 163.77 eV, respectively, consist of one contribution each, hence one chemical species.

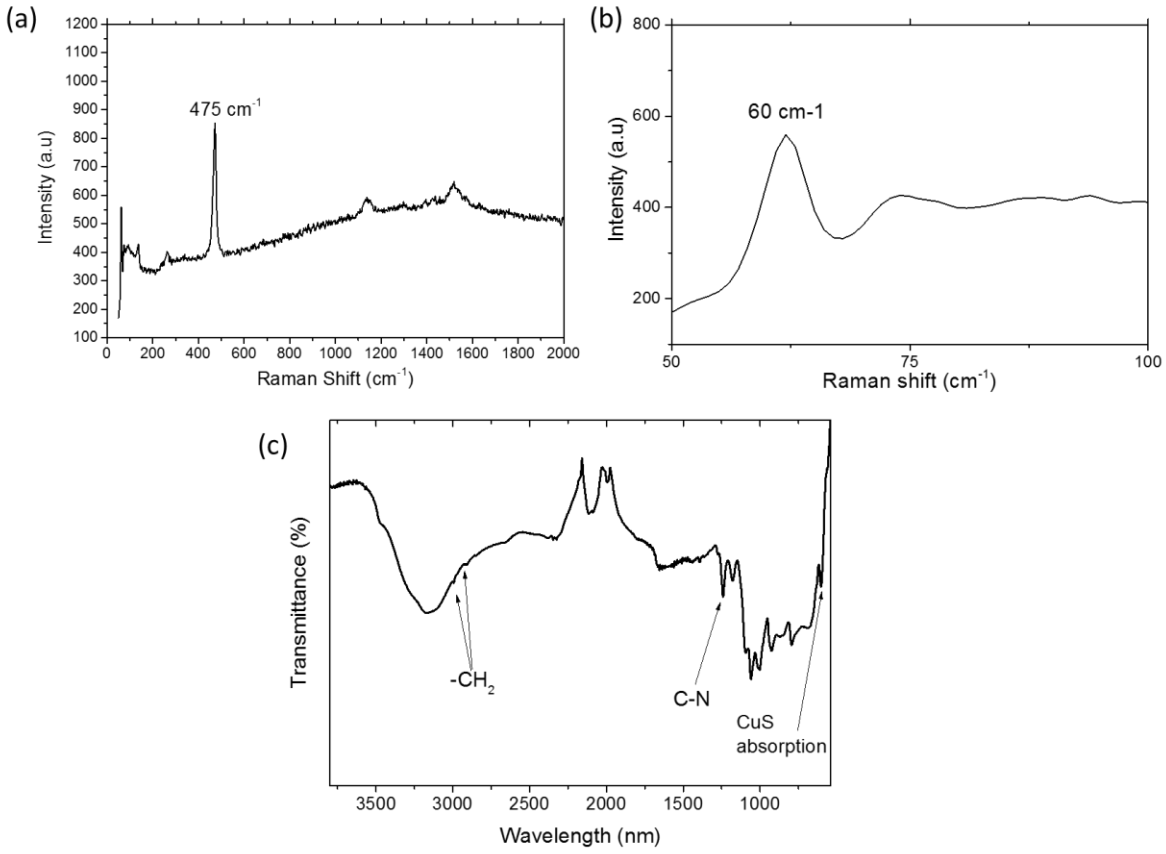


**Figure 3.2.** (a) Raman spectrum of synthesized CuS powder, (b) zoom to low Raman shift spectrum and (c) FTIR spectrum of CuS nanoparticles.

However, it is note here that assessing the chemical state of Cu can be difficult from the XPS main peak position. In particular, it is highlighted the presence of satellite features (between 940 eV and 946 eV) and the binding energy position of the LMM Auger peak, as revealed in **Figure 3.3b**. The observation of the Cu shake-up satellite at ca. 943 eV, and the strong peak corresponding to the Cu LMM Auger line at ca. 568.8 eV in the XPS survey (**Figure 3.3b**) are the signature for the presence of Cu(II), instead of Cu(I) in the material, discarding any additional mixed phase[125,126]. This is supported by the close to one Cu:S relative ratio estimated from the XPS results.

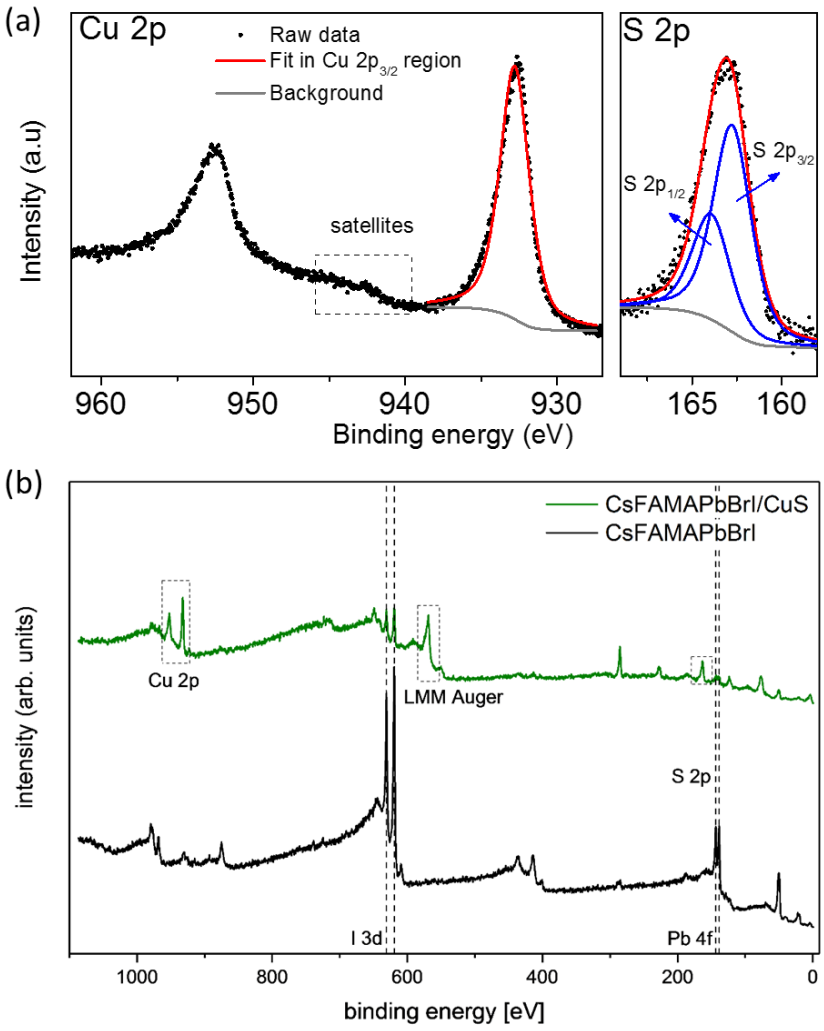


**Figure 3.3.** (a) XPS core level spectra of Cu 2p, and S 2p for CuS. The fitting was restricted to the part of the XP spectra corresponding to Cu $2p_{2/3}$ for Cu 2p. The shake-up satellite found between 940 eV and 946 eV (dashed rectangle) is characteristic of Cu(II). (b) Wide-scan XPS survey spectra of CsFAMAPbIBr (black), and CuS (green). The I 3d, and Pb 4f core level spectra from the underlying perovskite layer are detected for CuS, indicating an inhomogeneous CuS layer. The Cu LMM Auger peak at 568.8 eV, characteristic for Cu(II) is also discernable.

### 3.3. Mesoscopic PSC employing CuS nanoparticles as HTM.

To test CuS as a sole HTM amesoporous PSCs containing $MAPbI_3$ and CsFAMAPbIBr as the photoactive material was prepared in order to observe device photovoltaic response and to analyze interactions between CuS and corresponding

perovskite at the interface. $TiO_2$ was employed as electron blocking layer and CuS NPs dispersion as the HTM deposited by spin-coating technique at different rates. A statistical analysis of the photovoltaic parameters as a function of the HTM thickness is shown in **Figure 3.4a** and **3.4b** and **Table 3.1**, which is proportional to the rate employed during the spin-deposition.

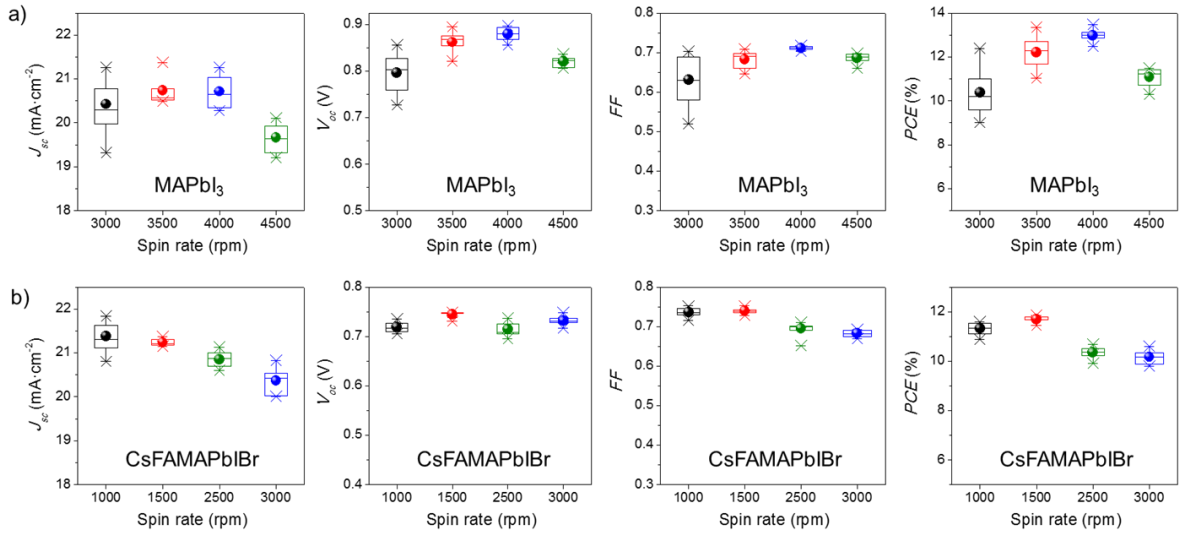


**Figure 3.4.** Photovoltaic parameters obtained for 80 devices (10 per condition) prepared for the CuS deposition optimization on (a) $MAPbI_3$ and (b) CsFAMAPbIBr perovskite.

Interestingly, the optimal conditions for CuS were very different depending on the perovskite employed, probably due to the distinct surface roughness achieved for each layer[127,128]. In particular, it was highlighted the different morphology and grain-crystals observed in the cross-sectional scanning electron microscopy (SEM) images presented in **Figure 3.5a** and **3.5b**, which clearly demonstrate a very smooth and compact surface for $MAPbI_3$ compared to CsFAMAPbIBr. This allows the use of much thinner HTM layers without the presence of shunts. Therefore, only 55 nm CuS NPs were necessary to properly cover $MAPbI_3$ layer, while 120 nm were

required for CsFAMAPbIBr. As a consequence, a PCE of ~13.5 % was achieved for $MAPbI_3$ and ~12% for CsFAMAPbIBr (**Figure 3.6**).

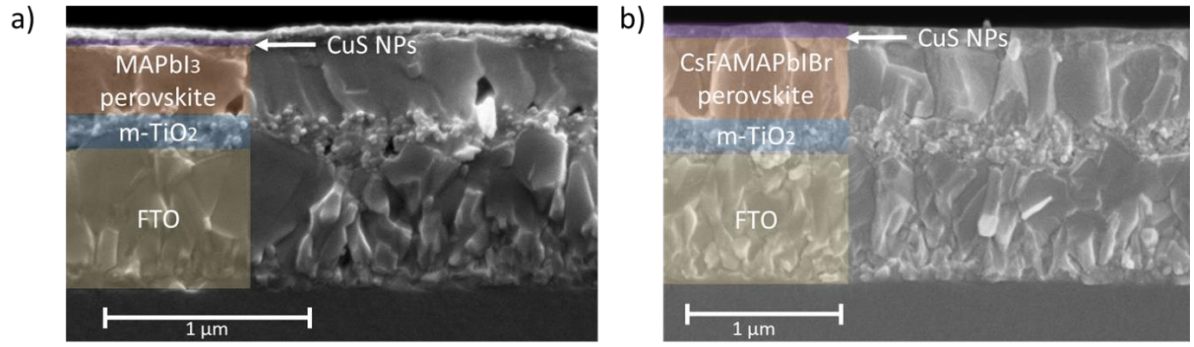


**Figure 3.5.** Cross-section SEM images highlighting each material in the structure of (a) $MAPbI_3$ and (b) CsFaMAPbIBr based PSC.

For comparison, devices without HTM exhibited extremely low $J_{sc}$ and $V_{oc}$ values (PCE below 1% in all cases), confirming the positive role of CuS as a hole-transporting layer. In addition, forward and reverse J-V curves of champion devices including CuS NPs and Spiro-OMeTAD as HTM are shown in **Figure 3.6 c, d** and **e**. As expected, some hysteresis is observed for all evaluated systems. This phenomenon has been reported elsewhere for n-i-p PSC and is attributed to ion migration inside perovskite material and specially to the formation and the release of interfacial charges in both electron and hole transporting layer contacts[129,130].

**Table 3.1.** Photovoltaic parameters of PSCs employing CuS and Spiro-OMeTAD as HTM. The statistics were extracted from more than 130 devices (at least 10 per condition).

| | **$CH_3NH_3PbI_3$ perovskite** | | | |
|---|---|---|---|---|
| **Spinner speed (rpm)** | $V_{oc}$ | $J_{sc}$ | FF | PCE |
| **Without HTM** | 0.57 ± 0.03 | 1.07 ± 0.28 | 0.69 ± 0.02 | 0.42 ± 0.18 |
| **3000** | 0.82 ± 0.04 | 20.46 ± 0.61 | 0.62 ± 0.06 | 10.45 ± 1.25 |

| | | | | |
|---|---|---|---|---|
| **3500** | 0.87 ± 0.02 | 20.92 ± 0.31 | 0.69 ± 0.02 | 12.49 ± 0.75 |
| **4000** | 0.88 ± 0.01 | 20.72 ± 0.36 | 0.71 ± 0.01 | 13.01 ± 0.29 (13.47) |
| **4500** | 0.83 ± 0.01 | 19.83 ± 0.34 | 0.69 ± 0.01 | 11.39 ± 0.41 |
| **Spiro-OMeTAD** | 1.04 ± 0.03 | 21.77 ± 0.31 | 0.74 ± 0.02 | 16.98 ± 0.43 |
| **$(FAPbI_3)_{0.78}(MAPbBr_3)_{0.14}(CsPbI_3)_{0.08}$ perovskite** | | | | |
| **Spinner speed (rpm)** | $V_{oc}$ | $J_{sc}$ | FF | PCE |
| **Without HTM** | 0.42 ± 0.02 | 8.16 ± 0.19 | 0.48 ± 0.03 | 1.64 ± 0.19 |
| **1000** | 0.72 ± 0.01 | 21.57 ± 0.33 | 0.73 ± 0.01 | 11.37 ± 0.24 |
| **1500** | 0.75 ± 0.02 | 21.23 ± 0.07 | 0.74 ± 0.01 | 11.72 ± 0.12 (11.85) |
| **2000** | 0.73 ± 0.02 | 19.95 ± 0.16 | 0.71 ± 0.02 | 10.33 ± 0.42 |
| **2500** | 0.71 ± 0.01 | 20.91 ± 0.18 | 0.69 ± 0.02 | 10.35 ± 0.22 |
| **3000** | 0.73 ± 0.01 | 20.29 ± 0.28 | 0.68 ± 0.01 | 10.15 ± 0.27 |
| **Spiro-OMeTAD** | 0.92 ± 0.01 | 21.95 ± 0.31 | 0.76 ± 0.02 | 15.27 ± 0.23 |

In parenthesis the maximum PCE obtained with each perovskite as light harvester and CuS as HTM.

Stability was evaluated at ambient conditions (~40% RH and ~20°C) being clear the strong instability of $MAPbI_3$ to light-induced degradation[131] as shown in **Figure 3.7**. In particular, devices containing $MAPbI_3$ perovskite show very poor performance after 192h, whereas CsFAMAPbIBr cells retain almost 80 % of the initial efficiency after 504 h. The relative low efficiency loss at the latter case might be attributed to moisture permeation through CuS NPs layer due to its low thickness and considerable air humidity during the test instead of CuS intrinsic factors since different reports show the high chemical stability of the CuS nanocrystals under similar conditions[89,97]. However, according to **Figure 3.7b** PCE retention is similar to the one observed in reference PSC employing CsFAMAPbIBr as light harvester and Spiro-OMeTAD as HTM. In this system instability can be caused by Spiro-OMeTAD

doping agents which are known for being highly hygroscopic so that water absorption and subsequent perovskite degradation are expected[132]. As a matter of fact, it is worth underlining here that despite the modest efficiencies obtained compared with the state-of-the-art, the reported results have high relevance because they imply the use of a low-temperature and solution-processed HTM which is employed for the first time solely as hole-transporting-layer avoiding the use of expensive extra electron-blocking materials. In particular, it is due to the proper precursor developed here which allows us to fabricate compact and high performance HTM films. Moreover, compared with Spiro-OMeTAD, the material cost at laboratory scale for the as prepared CuS-NPs is only 67.47 USD/$m^2$, which is 23 times lower than Spiro-OMeTAD (1591.17 USD/$m^2$) (see cost assessment in Appendix A). In addition, CuS as HTM is compatible with friendly halogen-free solvents and printing R2R technology unlike previous reported inorganic HTMs such as CuSCN[58].

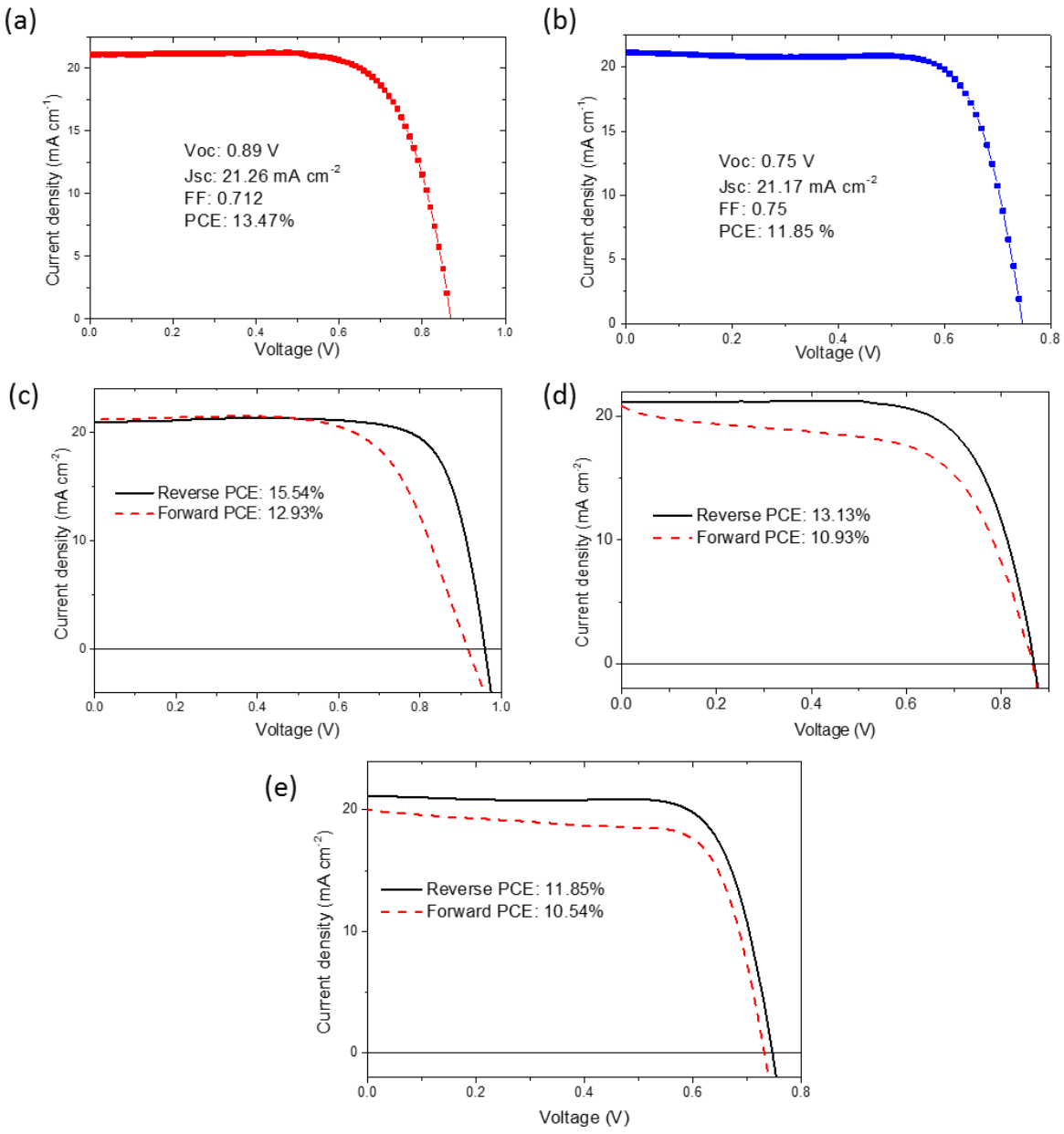


**Figure 3.6.** J-V curves and photovoltaic parameters of most efficient $MAPbI_3$ based (a) and CsFAMAPbBrI based (b) devices employing CuS NPs as HTM. Forward and reverse scan of PSC employing the following perovskite/HTM system: (c) reference CsFAMAPbIBr/Spiro-OMeTAD, (d) $MAPbI_3$/CuS and (e) CsFAMAPbIBr/CuS.

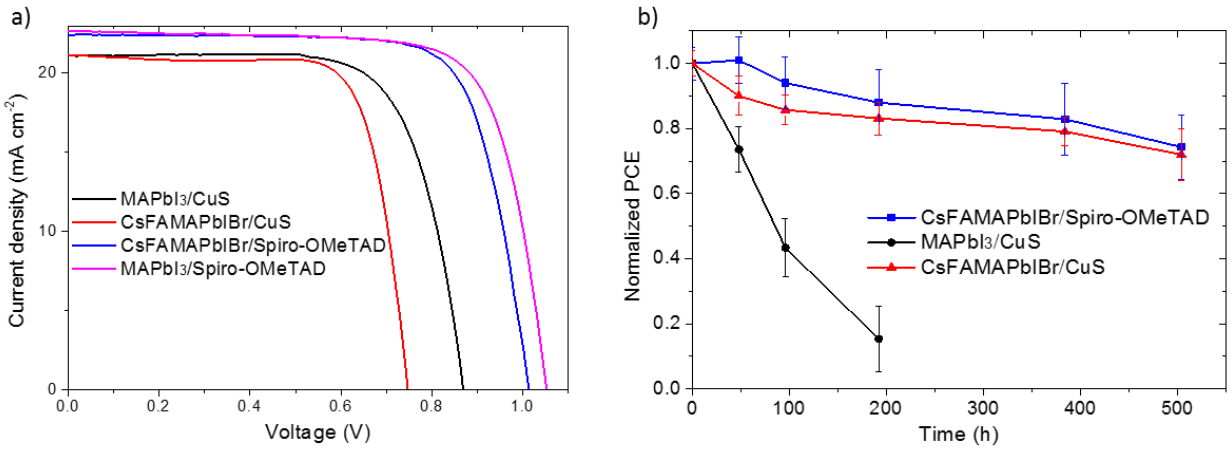


**Figure 3.7.** (a) J-V curves of PSC using CuS and reference Spiro-OMeTAD as HTMs in the two tested device architectures. (b) Stability test performed under 1 Sun light illumination (AM 1.5 Standard Spectrum) for PSC using CuS and Spiro-OMeTAD.

### 3.4. Insights on CuS working mechanisms as HTM in n-i-p PSC.

The *J-V* curves obtained after optimization are present in **Figure 3.7**. Note that the results reveal excellent values for $J_{sc}$ and *FF*, closely resembling those obtained with Spiro-OMeTAD (see **Table 3.1**). There is however a remarkable deterioration for $V_{oc}$, which decreases to 0.89 V and 0.74 V for $MAPbI_3$ and CsFAMAPbIBr respectively. Such low $V_{oc}$ values are indeed the ultimate responsible for the lower efficiencies. To further understand these observations and shed light into the origin of the low $V_{oc}$, UPS measurements were performed. **Figure 3.8** shows the work function ($\Phi$) and valence band spectra for both perovskites and CuS thin films on CsFAMAPbIBr. Interestingly, the valence band spectrum of CuS (**Figure 3.8b**) reveals some intensity that extends to the Fermi level (**Figure 3.8b-c**). A closer inspection at that binding energy region further highlights this tailing intensity, confirming a relatively low but distinguishable density of states (DOS) at the Fermi level (inset in **Figure 3.8c**). This provides additional support of the CuS NPs metallic character already reported

in literature[133] and corroborated by conductivity measurements in **Figure 3.9a**. In addition, the valence band maxima $E_{VBM}$ of CsFAMAPbIBr and $MAPbI_3$ are at 1.45 eV and 1.21 eV binding energy relative to $E_F$. Accordingly, both materials have a strongly n-type character, with the Fermi level pinned at their conduction band minimum (the optical band gap extracted from the absorption spectra in **Figure 3.9** was 1.61 eV and 1.58 eV, respectively).

The energy level diagram deduced from the UPS measurements is presented in **Figure 3.8e.** The filled DOS up to the Fermi level and the position of the conduction band minimum (CBM) in grey, as deduced from the 2.4 eV optical gap (**Figure 3.1b**), support the suitability of CuS for hole collection and electron blocking. However, even in this case, there is a considerable energy gap (~ 1.2 eV) between $MAPbI_3$ or CsFAMAPbIBr and CuS $E_{VBM}$ (5.61 eV, 5.71 eV and 4.61 eV, respectively), an important energy barrier that might favor the electron-hole recombination at the interface. Interestingly, despite the really small work function difference existing between $TiO_2$ and CuS contacts (0.6 eV), it is obtained a relatively high $V_{oc}$ (~ 0.9V in the $MAPbI_3$ case) in fully agreement with a recent investigation published by Ravishanka *et al*[134].

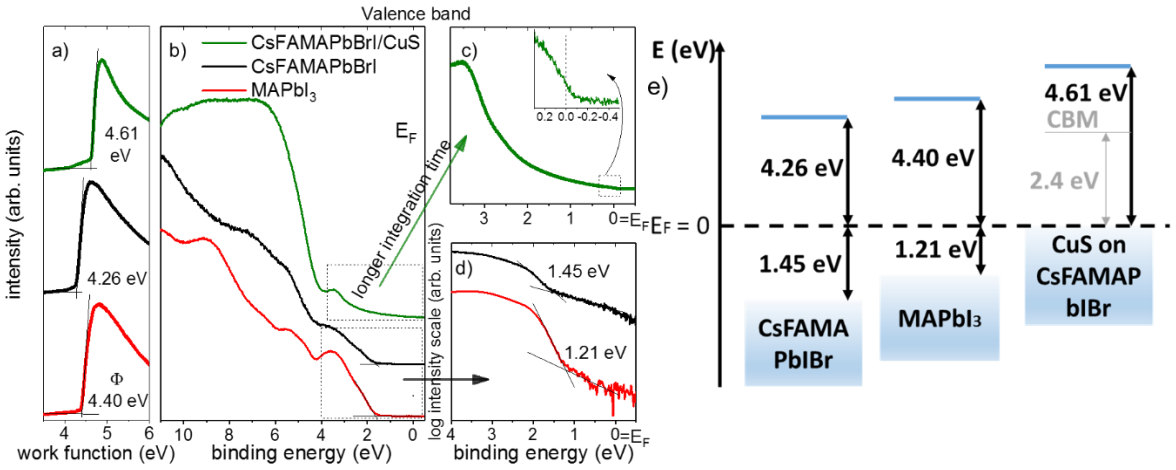


**Figure 3.8.** UPS spectra of CsFAMAPbIBr, MAPbI3 and CuS films. (a) Secondary electron cut-offs (SECO) for work function $\phi$ determination, (b) large and short binding energy range valence band spectra of (c) CuS, (d) CsFAMAPbIBr and $MAPbI_3$. The portion of the spectrum taken at smaller energy step in the inset in e) shows the presence of a density of states at the Fermi level for CuS. (e) Energy level diagram of CsFAMAPbIBr, $MAPbI_3$ and CuS. The work function ($\phi = E_{vac}-E_F$) and $E_{VBM}$ relative to the Fermi level $E_F$ are extracted from the UPS spectra in a) and c,d). The conduction band minimum position (CBM, in grey) is deduced from the the 2.4 eV band gap of CuS.

To further understand the effect of CuS as HTM charge extraction capability of the device interface employing CsFAMAPbIBr as light harvester was evaluated by comparing the photoluminescence (PL) quenching at $V_{oc}$ and short circuit conditions. Usually, the charge transfer dynamics are evaluated by comparing the PL quenching between the pristine bulk active layer and the interface behaviour. However, this gives only partial information and cannot fully explain the device mechanisms. In particular, when an HTM is present, different interface mechanisms causing PL quenching come into play, i.e. hole-transfer or distinct surface trap density. Therefore measuring the whole device under different operative conditions provides a more robust and useful analysis[135].

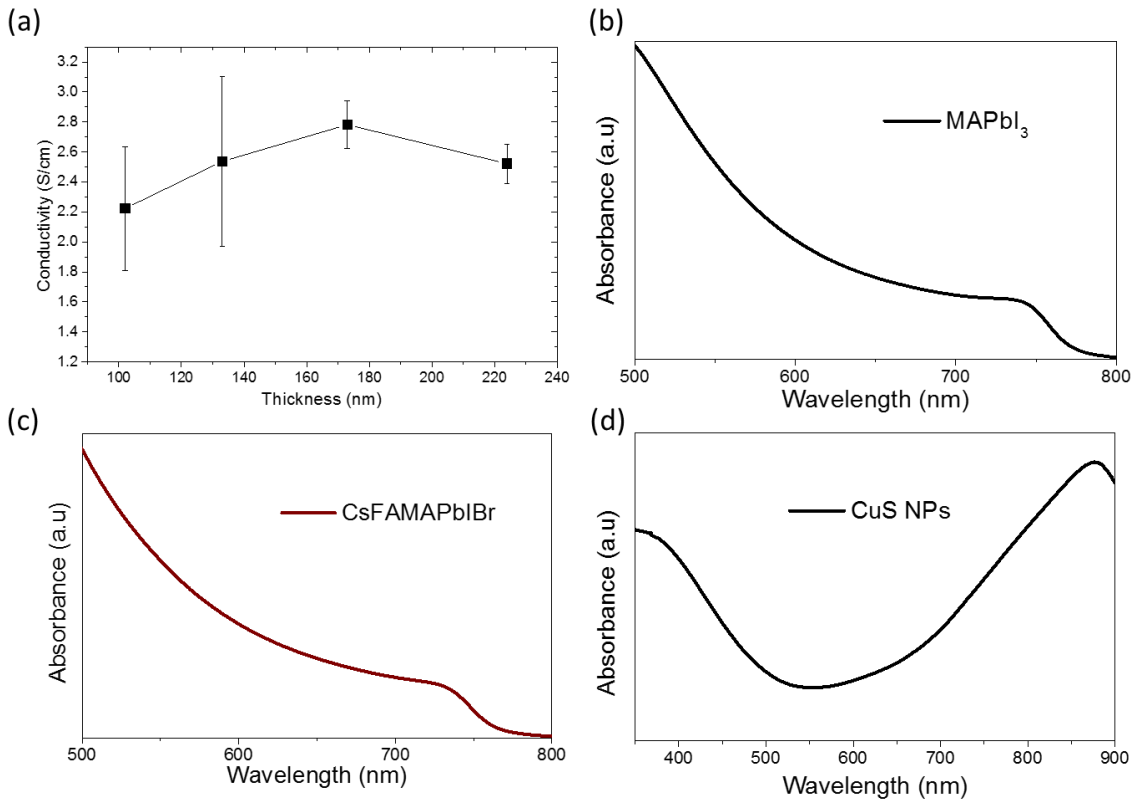


**Figure 3.9.** (a) Conductivity measurements of CuS films on glass. Absorption spectra of (b) $MAPbI_3$, (c) CsFAMAPbIBr and (d) CuS NPs films.

Because perovskites generate free carriers after photoexcitation[136], the PL intensity will depend on whether the device is at open or short circuit conditions. In the first case, PL is proportional to the density of electron-holes which radiatively recombine. The larger is this value, the better would be the device behaviour (minor density of trap states). However, at short circuit conditions part of the charges deviates through the external path, decreasing the radiative recombination and thus, the luminescence intensity. In this case, PL quenching induced in devices containing the exact same configuration except the CuS and Spiro-OMeTAD **(Figure 3.10)** was compared. At $V_{oc}$ conditions, the reference exhibits a PL as twice as the CuS device. Given the exact same thickness of the active layer, this suggest increased intrinsic non radiative recombination for the CuS-device, which can explain the low

experimental $V_{oc}$ values. At short circuiting, it is also observed ~20% lower quenching for the CuS-device than Spiro-OMeTAD, thus a slightly worse charge injection takes place. However, even in this case, when compared to the Spiro-OMeTAD, the charge transference is still happening in a considerable good extent.

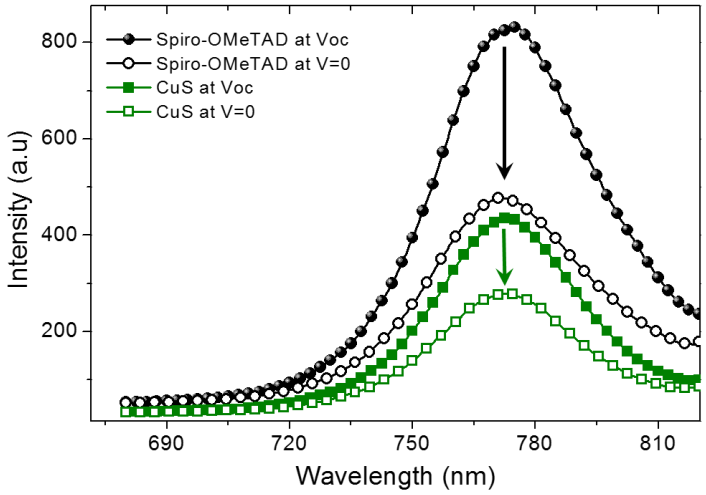


**Figure 3.10.** Photoluminescence spectra of PSC employing Spiro-OMeTAD and CuS as HTM at $V_{oc}$ and V= 0 V.

Noteworthy, further analyzing the samples by UPS upon light exposure, it was observed a rigid shift of both valence band and work function by up to ca. 0.7 eV (red curves, **Figure 3.11a-d**), which is fully reversible once the light is removed (grey and blue curves). Such situation is equivalent to the open circuit conditions where bottom and top electrodes are not in direct electrical contact. This effect, particularly observable due to the rather metallic character of CuS (**Figure 3.8c**), is a direct evidence of the hole-injection within CuS, which therefore behaves like an electrode with regards to the underlying perovskite. Accordingly, under illumination free charges are generated at the perovskite/CuS interface and holes are accumulated into the CuS layer, creating a space charge up to the sample surface[137]. Hence, the

extent of the energy shift observed here (0.74 V) is directly related to the $V_{oc}$, which is further enhanced by the CuS metallic character.

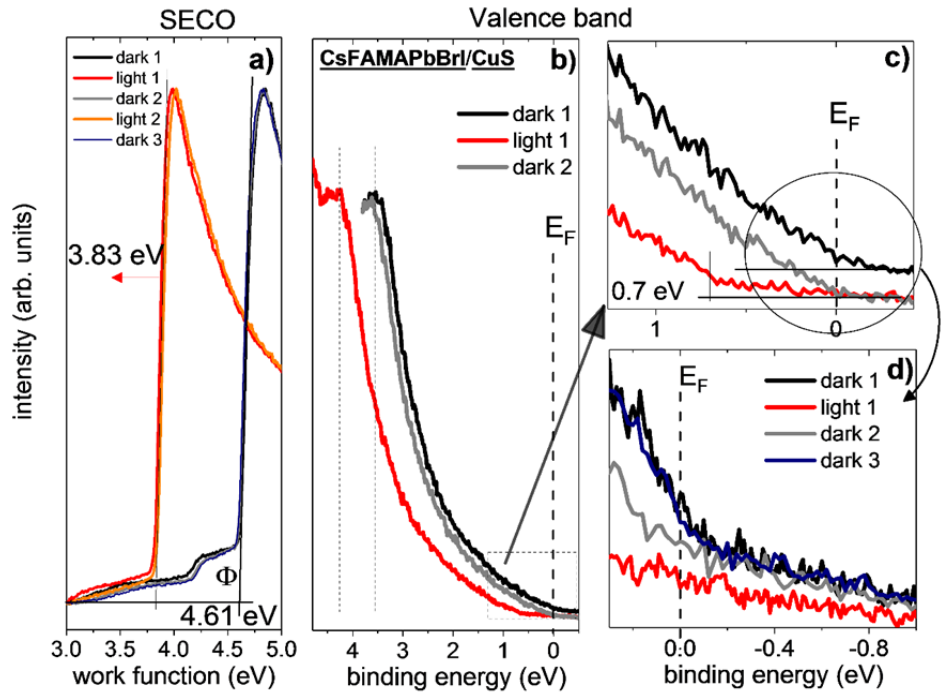


**Figure 3.11.** UPS spectra of CuS upon white light illumination: (a) reversible SECO shift after successive measurements in dark (black), under light (red), in dark (grey), under light (orange), and in dark (blue). (b) Large binding energy range and (c) short binding energy range valence band with reversible shift upon illumination. In (d) the second measurement in dark after illumination (dark 3, blue curve) shows the complete reversibility of the light-induced shift with time.

### 3.5. Conclusions

Therefore, it is possible to conclude that CuS NPs with a flake-like shape have been successfully synthesized and stabilized in non-polar solvents, fully compatible with hybrid lead halide perovskites. This material behaves for the first time as a sole p-type semiconductor in direct PSC thanks to the development of a proper colloidal precursor, which is a very cheap option to substitute expensive state-of-the art materials such as Spiro-OMeTAD (23 times lower in price). Our first observations

suggest that when CuS is employed as HTM, very high values of $J_{sc}$ and $FF$ are achieved leading to remarkable PCE close to 14%. However, this final efficiency is compromised by a significant reduced $V_{oc}$. According to the analysis performed here, the limited $V_{oc}$ is the result of an increased non-radiative recombination taking place at the perovskite/CuS interface, probably enhanced by the large energy barrier existing between the perovskite and CuS valence bands but at the same time $V_{oc}$ seems to be controlled by the metallic character of CuS revealed by UPS upon light exposure. Noteworthy, such a behaviour could be probably improving by using a proper interlayer to passivate the perovskite/CuS interface (e.g. thin conductive or insulating polymer layers, another inorganic semiconductor such as $NiO_x$, $Cu_2O$ or CuI) different to the expensive Spiro-OMeTAD, a suitable strategy that might be considered in future experiments. These findings contribute to fill the knowledge gap about the behaviour of CuS as HTM in PSC due to the previous reported impossibility of having high performance CuS films on perovskite. Moreover, our results point out CuS as a potential extremely low-cost and stable solution-process alternative to the state-of-the art organic HTMs in PSC, opening the door for new improvements and applications of this material towards large-scale low-temperature produced optoelectronic devices.

# Chapter 4. Air-stable n-i-p planar perovskite solar cells using nickel oxide nanocrystals as sole hole-transporting material.

This chapter is based on published work: Tirado et al. ACS Appl. Energy Mater. 2019, 2 (7), 4890–4899. DOI: 10.1021/acsaem.9b00603.

## 4.1. Introduction.

$NiO_x$ has been one of the most successful materials employed in p-i-n architectures.[49] It is an earth abundant p-type semiconductor with a wide band gap (Eg > 3.3eV) that provides high optical transmittance, proper hole mobility and conductivity, as well as high chemical stability.[34] Over the last years $NiO_x$ films have been fabricated by a wide range of techniques, including expensive methods like atomic layer deposition (ALD), physical or chemical vapor deposition (PVD and CVD respectively), electron beam evaporation, or vacuum evaporation,[47–49] as well as lower cost alternatives like spin-coating, screen-printing, spray pyrolysis or sol-gel.[49,138,139] All at once, these efforts combined with interface engineering and $NiO_x$ chemical doping allowed PCE of 20.5%.[138] However its use in n-i-p configurations has been very limited as the deposition of high performance $NiO_x$ films requires dealing with conditions compatible with the perovskite material, mostly based on low temperature processes and non-polar solvents. Indeed, examples of $NiO_x$ as HTM in n-i-p structure is limited to ALD deposition (PCE of 7.28%) and spin-coating (PCE of 9.11%), yet without judicious look to factors affecting PCE and stability.[49,61]Therefore, it is crucial to develop new strategies targeting high performance $NiO_x$ layers compatible with low-cost and stable n-i-p PSCs, and study different chemical and electronic phenomena involved in perovskite/$NiO_x$ interface.

In this chapter, $NiO_x$ nanocrystals were synthesized by an initial water-based methodology and then functionalized them with oleylamine molecules to obtain stable colloidal dispersions in non-polar solvents. Subsequently, this dispersion was employed to fabricate homogenous $NiO_x$ layers on top of a triple cation perovskite $(FAPbI_3)_{0.78}(MAPbBr_3)_{0.14}(CsPbI_3)_{0.08}$ (CsFAMAPbIBr) based cell in an n-i-p structure. Noticeable, $NiO_x$-based devices exhibited a stabilized PCE of 10.99% and a maximum efficiency of 12.71% which is the highest PSC reported so far with $NiO_x$ as top transport layer in n-i-p architecture. In addition, it is studied the effect of perovskite/$NiO_x$ interface on device performance by atomic force microscopy (AFM), kelvin probe force microscopy (KPFM) and ultraviolet photoelectron spectroscopy (UPS). Moreover, it was found that thanks to the hydrophobic nature of the functionalized $NiO_x$, un-encapsulated cells showed outstanding high-stability under very high levels of relative humidity in air, retaining ~90% of initial PCE after 1008 h.

### 4.2. Synthesis and characterization of nickel oxide nanocrystals.

The inorganic HTM fabrication consisted in two steps. First, it was employed a synthetic route reported by Ciro at al.[140] to obtain $NiO_x$ nanocrystals with hydrophilic groups at the surface (hl-$NiO_x$). Second, a ligand exchange process was carried out in a highly concentrated oleylamine solution prepared in chlorobenzene, in order to functionalize the nanocrystals towards a hydrophobic material suitable to disperse in non-polar solvents (ho-$NiO_x$), the representative scheme is showed **Figure 4.2d**. Although long alkyl chains could generate an insulating barrier between nanocrystals, we expect van der Waals force and hydrogen bonds, from oleylamine chains can avoid ho-$NiO_x$ separation and promote some contact points which will allow charge transfer. For more information refer to chapter 5 experimental section.

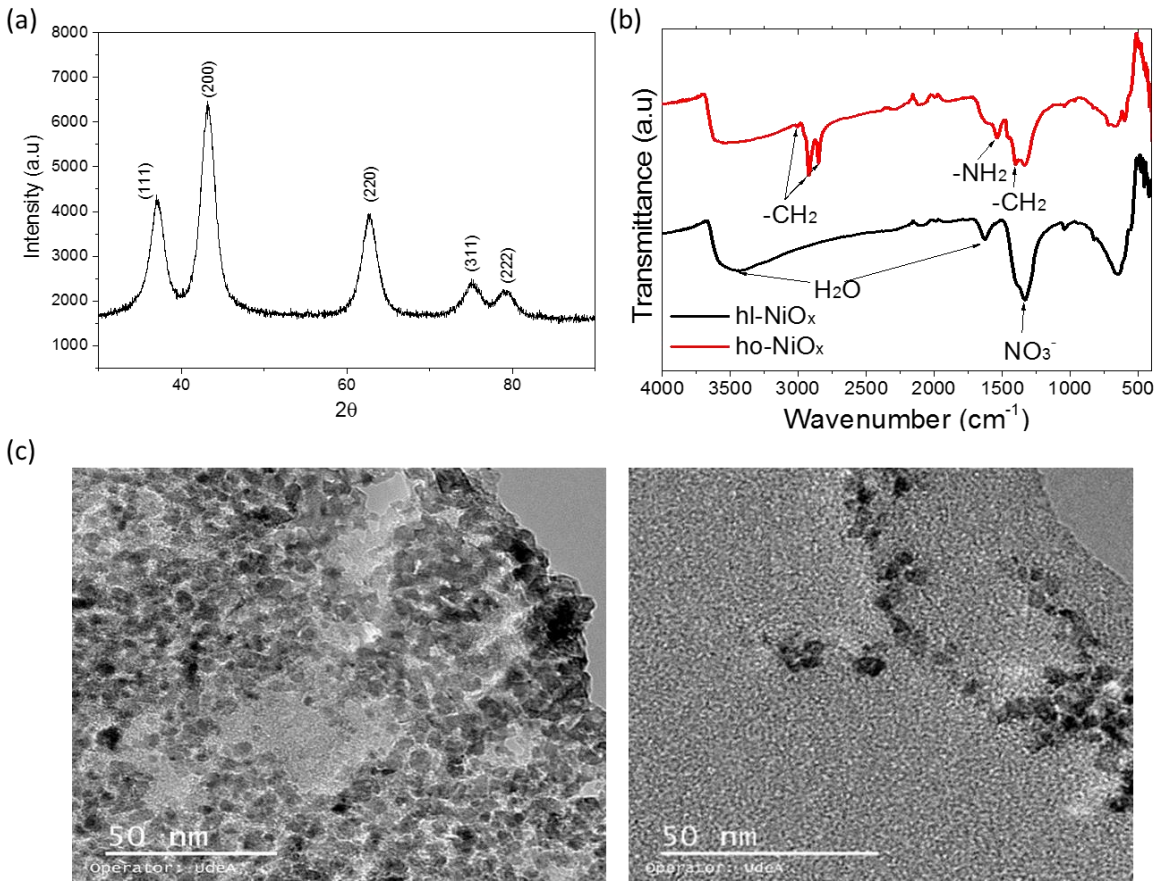

**Figure 4.1.** (a) XRD diffractogram of hydrophobic $NiO_x$ nanocrystals (ho-$NiO_x$). (b) FTIR spectra of hydrophilic and hydrophobic $NiO_x$ nanocrystals. (c) TEM images of ho-$NiO_x$.

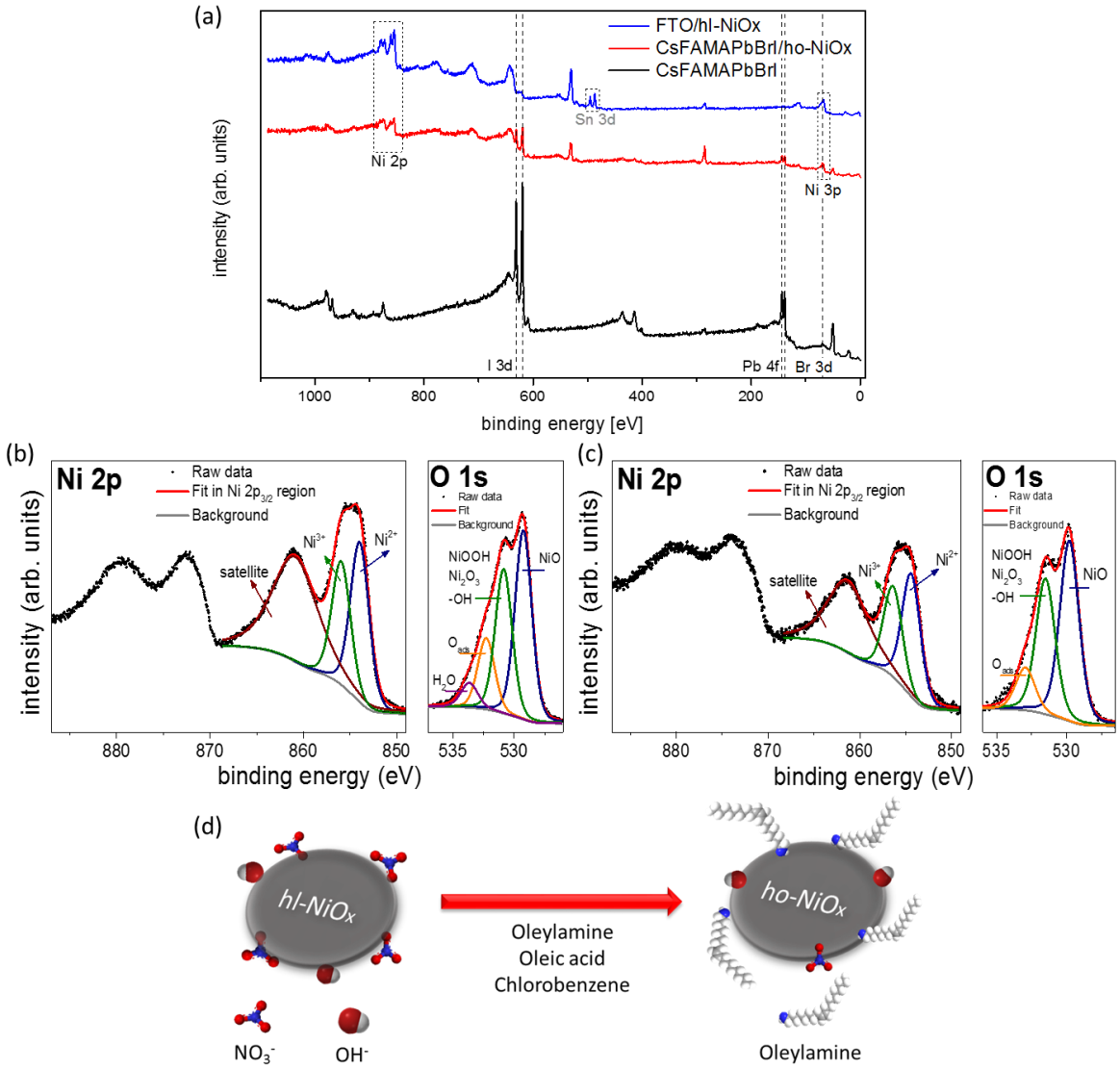


**Figure 4.2.** Analysis of hl-NiOx and ho-NiOx chemical composition by XPS. (a) Wide-scan XPS survey spectra of CsFAMAPbIBr (black), ho-$NiO_x$ (red), and hl-$NiO_x$ (blue). The I 3d, and Pb 4f core level spectra from the underlying perovskite layer are detected for ho-$NiO_x$. Sn 3d from the underlying FTO substrate is also observed for hl-$NiO_x$. (b) XPS core level spectra of Ni 2p, and O 1s for (c) hl-$NiO_x$, and (d) ho-$NiO_x$. The fitting was restricted to the part of the XPS spectra corresponding to Ni $2p_{3/2}$, for Ni 2p. The possible compounds corresponding to the different O 1s

species in the Ni samples are indicated. (d) Scheme of molecules adsorbed on $NiO_x$ surface before and after hydrophobic functionalization process.

X-Ray diffraction (XRD) pattern of the synthesized material, shown in **Figure 4.1a**, revealed several diffraction peaks at 37.02°, 43.27°, 62.76°, 74.99° and 79.22° which can be assigned to (111), (200), (220), (311) and (222) planes of nickel (II) oxide, confirming the presence of desired material. FT-IR analysis was also performed to verify the exchange of the ligand on the nanocrystal surface (see **Figure 4.1b**). As observed in the **Figure 4.1b**, hl-$NiO_x$ nanocrystals exhibit a characteristic absorption band at 1336 $cm^{-1}$ which is assigned to the vibration mode of nitrate ions.[140] An additional broad band at 3350 – 3400 $cm^{-1}$ and a sharp band at 1630 $cm^{-1}$ which can be also associated to adsorbed water at the surface.[141] Besides, the FT-IR spectrum of functionalized ho-$NiO_x$ nanocrystals exhibit two additional sharp peaks at 1400 and 1533 $cm^{-1}$ typical for the $–CH_2$ and $–NH_2$ scissoring modes, respectively. The -CH groups are also confirmed by the peaks at 2850, 2920 and 3000 $cm^{-1}$ assigned to antisymmetric and symmetric C-H stretching vibration.[142,143] Therefore, the presence of aliphatic amine compounds attached to the nanoparticles surface can be confirmed. Thanks to these ligands it was possible to form stable colloidal dispersions of ho-$NiO_x$ nanocrystals in non-polar solvents like chlorobenzene. In addition, transmission electron microscopy (TEM) images, presented in **Figure 4.1c,** revealed a spherical shape for the $NiO_x$ nanocrystals, with a diameter between 3-8 nm, highly desirable for stable colloidal dispersions.

To further investigate chemical composition of hl-$NiO_x$ and ho-$NiO_x$ X-Ray photoelectron spectroscopy (XPS) measurements were performed. Core level peaks assigned to the respective underlying substrate are observed in the wide-scan survey (**Figure 4.2a**): Pb 4f and I 3d from the CsFAMAPbIBr perovskite for ho-$NiO_x$, and Sn 3d from the fluorine doped tin oxide (FTO) for hl-$NiO_x$ which actually are

the corresponding substrates for the analysis. High resolution XPS scan have been conducted for the main core levels Ni 2p and O 1s (**Figure 4.2b and 4.2c**). The Ni 2p XPS spectrum has a complex structure consisting of several multiplets and satellites.[144] The peak at high binding energy between 869.7 eV and 877 eV corresponds to Ni $2p_{1/2}$ (**Figure 4.2b and 4.2c**); the fitting procedure have been restricted to Ni $2p_{3/2}$. The Ni $2p_{3/2}$ spectrum of ho-$NiO_x$ exhibits a peak at 854.4 eV which can be assigned to $Ni^{2+}$ as in NiO, as supported by the observation of the O 1s peak 529.8 eV.[145] The Ni $2p_{3/2}$ at 856.4 eV in ho-$NiO_x$ corresponds to Ni in a higher oxidation state $Ni^{3+}$, possibly as in $Ni_2O_3$, or NiOOH. This would correlate with the presence of the O 1s peak at 531.5 eV, which corresponds to the oxygen species in these compounds and in hydroxide.[145,146] However, the Ni 2p peak at 856.4 eV, which is at 2 eV binding energy higher than that of $Ni^{2+}$, might actually also correspond to $Ni^{3+}$ that refers to $Ni^{2+}$ with a quasilocalized hole, i.e. defect cation, which would corroborate and explain the p-type conductivity of the $NiO_x$ material.[146–148] The typically strong shake-up satellite structure of Ni 2p is observable at ca. 861.4 eV. The O 1s peak at 532.9 eV possibly corresponds to adsorbed atomic oxygen on the sample surface. Although the binding energy position of the core level peaks of hl-$NiO_x$ shifts following the trend observed in ho-$NiO_x$, the different contributions to Ni 2p and O 1s are also observed in **Figure 4.2b**. Additionally, one O 1s peak at 533.65 eV is also observed for hl-$NiO_x$. This peak might be due to the presence of some residual water at the surface of nanocrystals, which has been processed from aqueous solution. These findings not only corroborate the existence of $NiO_x$ for all samples but indicate the presence of hydroxyl, oxydroxide and nickel trioxide species in both hl-$NiO_x$ and ho-$NiO_x$ nanocrystals. **Figure 4.2d** illustrates the ligand exchange reaction taking place at $NiO_x$ surface accordingly to FT-IR and XPS results.

### 4.3. Application of nickel oxide nanocrystals as HTM in planar n-i-p PSC.

In order to confirm the capability of ho-$NiO_x$ as efficient HTM, a series of planar perovskite solar cells were fabricated using the following device architecture: ITO/$SnO_2$/CsFAMAPbIBr/ho-$NiO_x$/Au. In brief, a thin film CsFAMAPbIBr perovskite was sandwiched between $SnO_2$ (used as electron transporting material, ETM) and ho-$NiO_x$, deposited by spin-coating. Finally, a thin layer of gold was thermal evaporated as top electrode. Three different ho-$NiO_x$ colloidal dispersions with a concentration of 20, 30 and 40 mg/ml were evaluated (see **Figure 4.3**). A good ho-$NiO_x$ film formation was previously tested on a mesoscopic n-i-p architecture as shown in cross-section SEM image in **Figure A3** (Appendix). As observed, they all exhibited high short-circuit currents ($J_{sc}$) ~22 mA·cm$^{-2}$ indicating a good charge extraction by ho-$NiO_x$. In addition the open circuit voltage ($V_{oc}$) showed improved valued with increased concentration (from ~0.75 to ~1.04 V), suggesting inhomogeneities on the film coverage for low concentrations. Yet the fill factor (*FF*) was remarkably low ~50% probably due to lower conductivity of ho-$NiO_x$ films compared to Spiro-OMeTAD (see discussion below). In agreement with the photovoltaic parameters trend, a maximum PCE of 8.57%, 9.36% and 12.71% was obtained for the 20, 30 and 40 mg/ml dispersions, respectively. Taking a deep look at the latter condition (see **Figure 4.3** and **Table 4.1)**, it wasobserved a continuous decrease in $V_{oc}$ as the film thickness is reduced, while $J_{sc}$ shows the opposite trend. This led to a compromised film thickness of ~50 nm, which can establish as the optimal conditions to fabricate a proper ho-$NiO_x$ top film on CsFAMAPbIBr. Particularly, an average PCE of 11.38% was observed meanwhile a champion device with a $J_{sc}$ of 22.53 mA cm$^{-2}$, $V_{oc}$ of 1.036 V, *FF* of 54.42% and PCE of 12.71% was also obtained, which is to date the most efficient PSC reported employing $NiO_x$ in an n-i-p configuration. For comparison, planar n-i-p PSC were fabricated using the state-of-the art Spiro-OMeTAD, as well as HTM-free cells. The Spiro-OMeTAD-based champion device exhibited a $J_{sc}$ of 23.14 mA cm$^{-2}$, $V_{oc}$ of 1.04 V, *FF* of 71.86% and PCE

of 17.36%. On the other hand, PSC without HTM showed a poor performance with a $J_{sc}$ of 20.44 mA cm$^{-2}$, $V_{oc}$ of 0.66 V, *FF* of 40.65% leading to a PCE of 5.52%. Results of HTM-free cells evidence the crucial role of HTMs in n-i-p configuration and the positive effect of ho-$NiO_x$ on the photo-generated charge collection. Certainly, by employing ho-$NiO_x$ as HTM, the $V_{oc}$ and $J_{sc}$ increased around 58% and 11% reaching comparable values with the Spiro-OMeTAD-based reference device. This fact indicates a reduction in the surface recombination and better hole collection at perovskite/HTM interface thanks to ho-$NiO_x$ layer compared to "HTM-free" case. **Figure 4.4a** summarizes the *J-V* curves obtained for ho-$NiO_x$ PSCs at different precursor concentrations. Spiro-OMeTAD and HTM-free cells are also included for comparison. As previously mentioned, the *FF* is the parameter that mostly limits the cell performance and hinders a behavior comparable to reference devices. This situation might be attributed to non-radiative recombination paths at perovskite/ho-$NiO_x$ interface[19] which can be the result of poor interconnection between $NiO_x$ nanoparticles and light harvester as seen in inverted structures[49].The hysteresis analysis for both reference and ho-$NiO_x$ devices is also reported in **Figure 4.5**. This phenomenon has been widely observed in n-i-p PSC and can be attributed to ion migration inside perovskite material and to the formation and release of interfacial charges especially in ETM/perovskite contact.[129,130] Thus, it was obtained the stabilized power output (SPO) at maximum power point (extracted from J-V curves) of the champion PSC employing ho-$NiO_x$ as HTM in order to have a more trustworthy measurement of the device PCE. A SPO of 10.99%, close to the average PCE, was observed indicating that hysteresis has a weak influence on the resulting SPO.

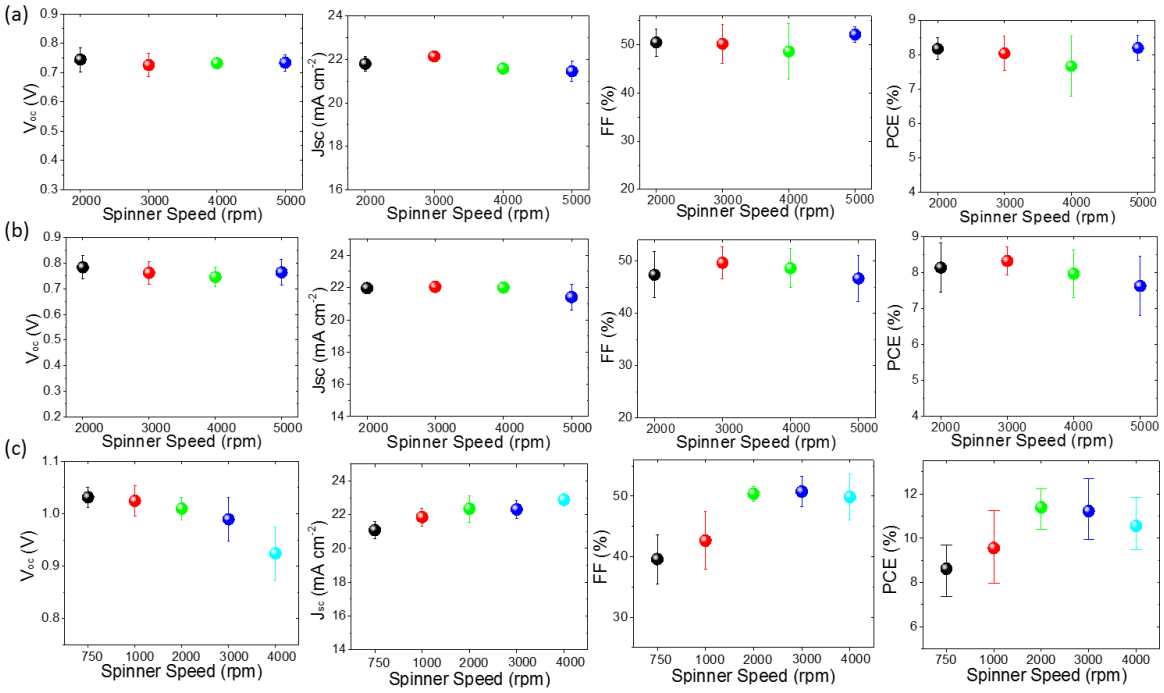


**Figure 4.3.** Photovoltaic parameters of PSCs fabricated with ho-$NiO_x$ as HTM employing three different colloidal suspensions precursors: (a) 20 mg/ml, (b) 30 mg/ml and (c) 40 mg/ml.

**Table 4.1.** PSC performance employing ho-$NiO_x$ at different spinner speed, control Spiro-OMeTAD and HTM free devices. In parenthesis champion ho-$NiO_x$ based PSC.

| HTM | $V_{oc}$ | $J_{sc}$ | FF | PCE |
|---|---|---|---|---|
| $NiO_x$ 750 rpm | 1.03 ± 0.02 | 21.09 ± 0.52 | 39.61 ± 4.05 | 8.62 ± 0.92 (9.69) |
| $NiO_x$ 1000 rpm | 1.02 ±0 .03 | 21.86 ± 0.53 | 42.67 ± 4.77 | 9.55 ± 1.05 (11.24) |
| $NiO_x$ 2000 rpm | 1.01 ± 0.02 | 22.35 ± 0.78 | 50.41 ± 1.21 | 11.38 ± 0.65 (12.23) |
| $NiO_x$ 3000 rpm | 0.99 ± 0.04 | 22.32 ± 0.52 | 50.77 ± 2.53 | 11.22 ± 0.92 (12.71) |
| $NiO_x$ 4000 rpm | 0.92 ± 0.05 | 22.89 ± 0.37 | 49.88 ± 3.75 | 10.55 ± 0.98 (11.85) |
| Spiro-OMeTAD | 1.05 ± 0.02 | 22.42 ± 0.77 | 68.98 ± 3.65 | 16.34 ±1.03 |
| No HTM | 0.65 ± 0.04 | 20.79 ± 0.37 | 39.26 ± 2.25 | 5.28 ± 0.51 |

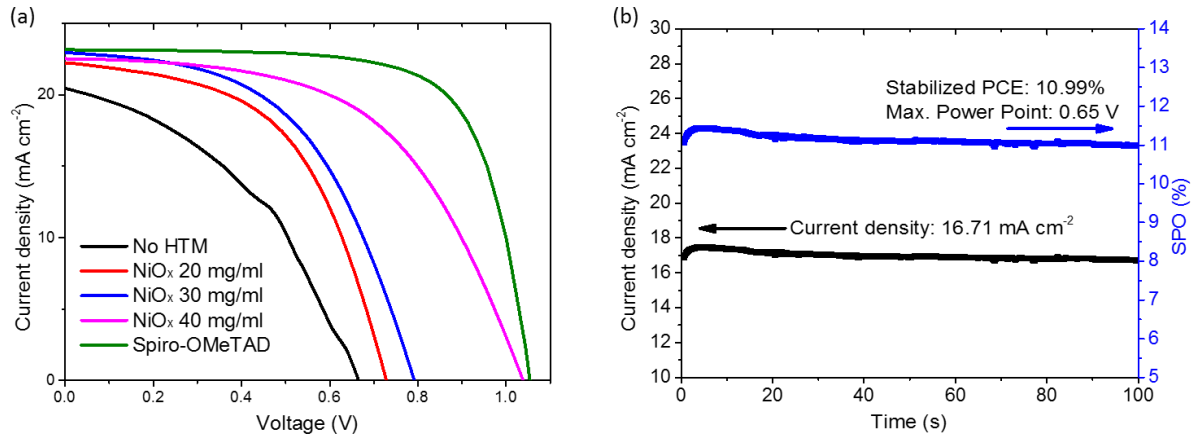


**Figure 4.4.** Photovoltaic response of PSC employing ho-NiOx as HTM. (a) J-V curves of best PSC with three different ho-$NiO_x$ precursor concentration, reference Spiro-OMeTAD and with no HTM, respectively. (b) Stabilized power output (SPO) of champion ho-$NiO_x$ based PSC at maximum power point.

To further understand the different trends showed by the photovoltaic parameters of ho-$NiO_x$ based PSC, a morphological and electrical analysis of the corresponding layers was performed. Atomic Force Microscopy (AFM) images of the HTM precursor showed the layer covered completely the CsFAMAPbIBr (**Figure 4.6a)**, with a film thickness ranging from ~50 nm to 24 nm, and a roughness from 24.3 nm to 14.3 nm (**Figure 4.6b**). Therefore, the average best performing devices had the thickest ho-$NiO_x$ layer, which led to highest values of $V_{oc}$ thanks to the improved protection against gold evaporation. In contrast, the thinnest layers presented clear shunt paths and defects, and thus decreased $V_{oc}$. An electrical conductivity of 1.29 x $10^{-2}$ and 9.94 x $10^{-3}$ S $cm^{-1}$ was measured for optimized Spiro-OMeTAD and ho-$NiO_x$ layers respectively, as showed in **Figure 4.6c**. Despite those values are similar to those reported in literature,[149] the conductivity for ho-$NiO_x$ remains lower to the reference Spiro-OMeTAD, and may be one of the reasons for the low *FF*. This situation can be attributed to oleylamine capping agent which is beneficial in terms of colloidal stability but detrimental for charge transport and interaction between

$NiO_x$ nanocrystals. Accordingly, this finding represents a clear path towards obtaining more efficient PSC with ho-$NiO_x$ as HTM. Thus, by exchanging long chain capping agents with shorter ligands, there is potential to increase nanocrystals interaction so that conductivity would reach higher values than Spiro-OMeTAD, a suitable strategy that might be considered in future experiments.

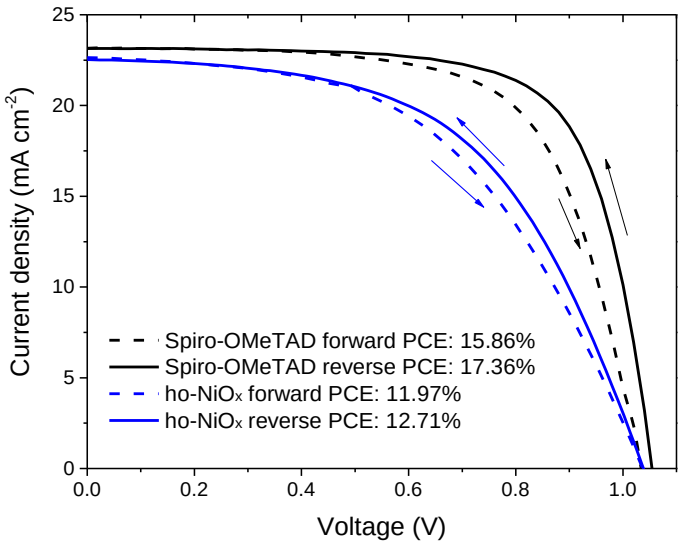


**Figure 4.5.** J-V curves of forward and reverse voltage scan of champion devices employing ho-$NiO_x$ (blue) and Spiro-OMeTAD (black) as HTM.

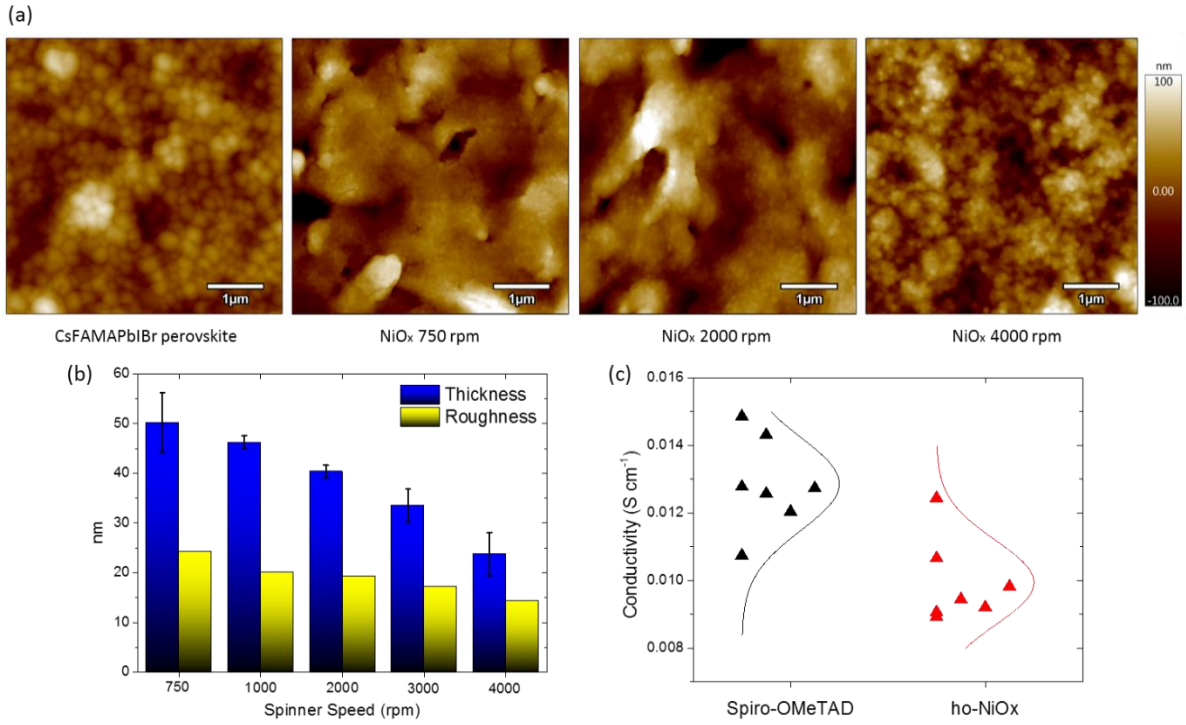


**Figure 4.6.** Morphological and electrical properties of ho-$NiO_x$ films. (a) Morphology micrographs by AFM of CsFAMAPbIBr perovskite and ho-$NiO_x$ layers deposited on top of CsFAMAPbIBr perovskite at different spin-coating conditions. (b) Thickness and roughness of ho-$NiO_x$ layers on $(FAPbI_3)_{0.78}(MAPbBr_3)_{0.14}(CsPbI_3)_{0.08}$ (CsFAMAPbIBr) perovskite. (c) Conductivity measurements of Spiro-OMeTAD and ho-$NiO_x$ (2000 rpm) by four point probe.

Additionally, surface photovoltage measurements (SPV) were performed to analyze the contribution of Spiro-OMeTAD and ho-$NiO_x$ to the resulting device $V_{oc}$. The ITO/$SnO_2$/CsFAMAPbIBr/HTM structure was tested under different illumination intensities. As shown in **Figure 4.7a**, SPV is positive for both cases indicating a desirable p-type nature of the two materials and a proper hole collection and transport from the light harvester bulk to the HTM (as illustrated in band diagram of **Figure 4.7b**).[150] Interestingly, SPV magnitude employing Spiro-OMeTAD and ho-$NiO_x$ differs around ~280 mV meaning that a most efficient photogenerated free-charge collection is present at the perovskite/Spiro-OMeTAD interface compared to the perovskite/ho-$NiO_x$ interface.[151] However, extracted $V_{oc}$ from *J-V* curves differs

just in few millivolts which suggest that ho-NiOx based PSC have the potential to reach a higher photovoltage due to a better valence band alignment (it will be discussed later) and the possibility of increase conductivity and hole mobility.

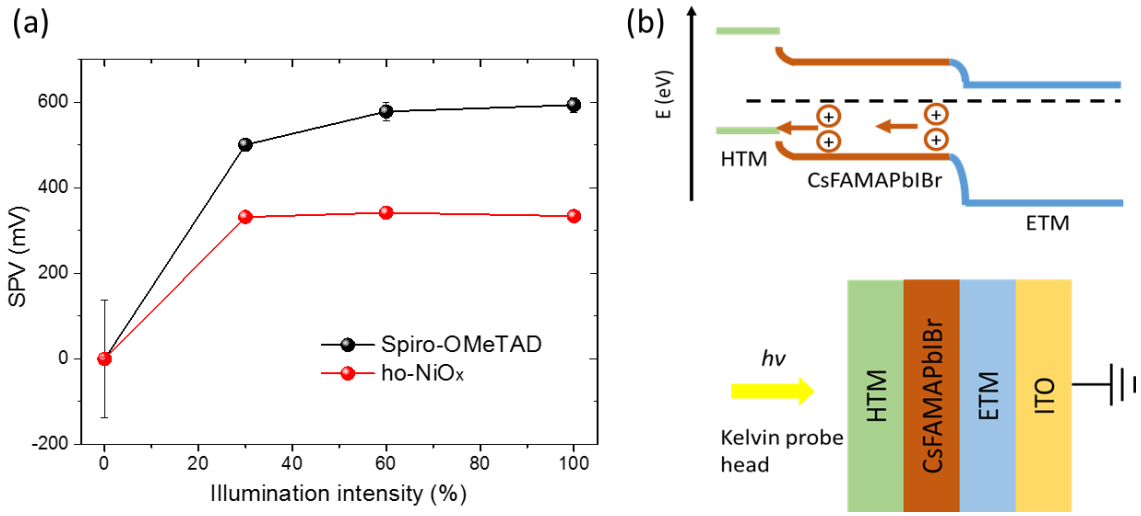


**Figure 4.7.** Charge extraction analysis of evaluated HTM by KPFM. (a) Surface photovoltage measurement of PSC employing ho-NiOx and Spiro-OMeTAD under different illumination intensities. (b) Scheme of back-electrode free device used for KPFM analysis and band diagrams showing charge accumulation at the side of the sample that was illuminated.

To analyze the band alignment between light harvester/HTM and the effect of surface ligand exchange on $NiO_x$ nanocrystals energy bands it was performed ultraviolet photoelectron spectroscopy (UPS) measurements of CsFAMAPbIBr perovskite, hl-$NiO_x$ and ho-$NiO_x$. The work function and valence band spectra of the two $NiO_x$, and that of the perovskite samples are shown in **Figure 4.8**. The work function $\phi$ is determined from the secondary electron cut-offs (SECO). $\phi$ values of hl-$NiO_x$ and ho-$NiO_x$ differ by ca. 0.7 eV (**Figure 4.8a**). The valence band spectra and particularly the valence band maxima $E_{VBM}$, each of them determined from the onset of the spectrum, also differ by 0.94 eV (**Figure 4.8 b-d**). These differences are likely to put on the account of the different substrates used for both samples, since ho-$NiO_x$ was deposited on perovskite and hl-$NiO_x$ directly on FTO. Moreover, as mentioned

above, these $NiO_x$ materials have been prepared from different solution, using oleylamine ($C_{18}H_{35}NH_2$) as a ligand in chlorobenzene, and OH-groups as ligands in water for ho-$NiO_x$, and hl-$NiO_x$, respectively. For instance, the presence of OH-groups or water residue on the surface of hl-$NiO_x$ might induce a surface dipole that increases the work function in comparison to ho-$NiO_x$. The surface of the CsFAMAPbIBr perovskite is strongly n-type ($E_{VBM}$=1.45 eV), considering an optical band gap of ca. 1.61 eV (**Figure 4.9**). The lower $E_{VBM}$ of $NiO_x$ indicates a favorable energy level alignment for the extraction of holes from CsFAMAPbIBr to ho-$NiO_x$ compared to Spiro-OMeTAD ($E_{VBM}$ extracted from Hawash et al. work[152]) as summarized in the energy diagram in **Figure 4.8f**. Moreover, this finding together with the SPV measurements suggests that some surface recombination paths exist at perovskite/ho-$NiO_x$ interface which limits $V_{oc}$. Possibly, an improvement in HTM morphology and an increase of its conductivity by oleylamine replacement as capping ligand, should enhance $V_{oc}$ and *FF* leading to more efficient PSC employing ho-$NiO_x$ as HTM.

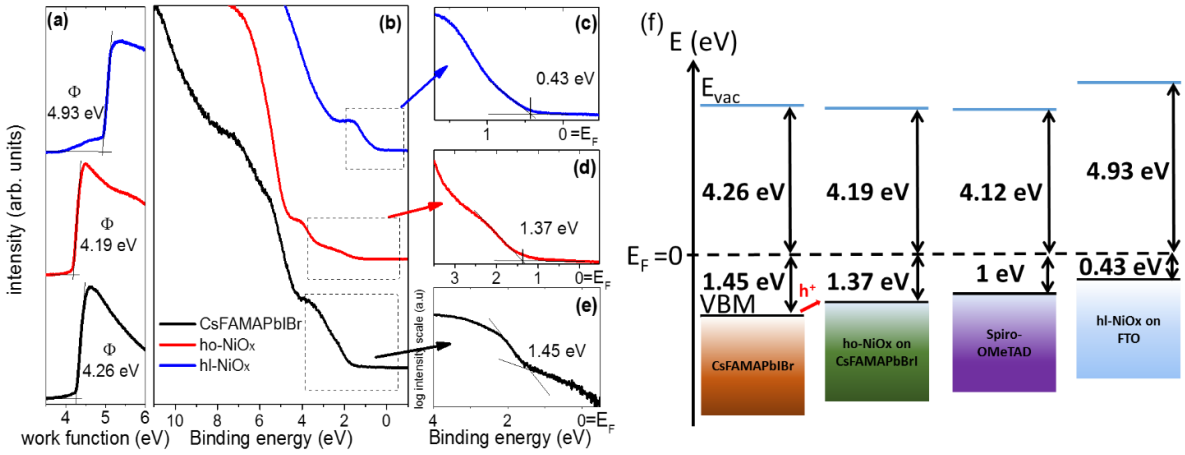


**Figure 4.8.** UPS spectra of the CsFAMAPbIBr perovskite film (black curves), ho-$NiO_x$ on CsFAMAPbIBr (red curves), and hl-$NiO_x$ on FTO (blue curves): (a) SECO for determining the work function ϕ, (b) large binding energy range valence band spectra, and short binding energy range valence band spectra of (c) hl-$NiO_x$, (d) ho-$NiO_x$, and (e) CsFAMAPbIBr. (f) Energy diagram

summarizing the energy level positions extracted from the UPS spectra and including energy levels of Spiro-OMeTAD from reference.[152]

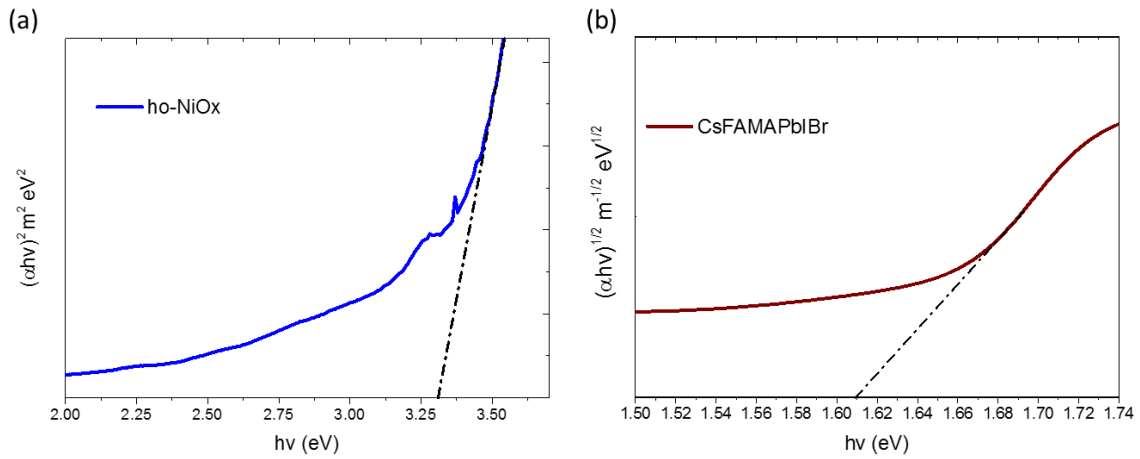


**Figure 4.9.** Band gap estimation of ho-$NiO_x$ (a) and CsFAMAPbIBr perovskite (b) from corresponding absorption spectra.

Additionally, photoelectron spectra have been collected upon illumination of the $NiO_x$ samples (**Figure 4.10**). A reversible shift of the work function and $E_{VBM}$ by ca. 0.2 eV is detected under light for ho-$NiO_x$ as shown in **Figure 4.10**. This shift can be interpreted as a space charge observed at the surface. This is a consequence of charge carrier generation in the perovskite layer upon additional illumination and subsequent collection at the perovskite/ho-$NiO_x$ interface, followed by the accumulation of electrons, and holes in the perovskite, and the ho-$NiO_x$ layers, respectively. Therefore, the binding energy shift observed here is related to a space charge comparable to the case in open circuit conditions upon illumination. However, likely and *inter alia*, due to the low energy offset between the CsFAMAPbIBr under layer and ho-$NiO_x$, and the photocurrent that leaves the sample during the measurement,[137] thus affecting the overall current density, the shift upon illumination has a smaller extent (ca. 0.2 eV) in comparison to $V_{oc}$= 1.03 V.

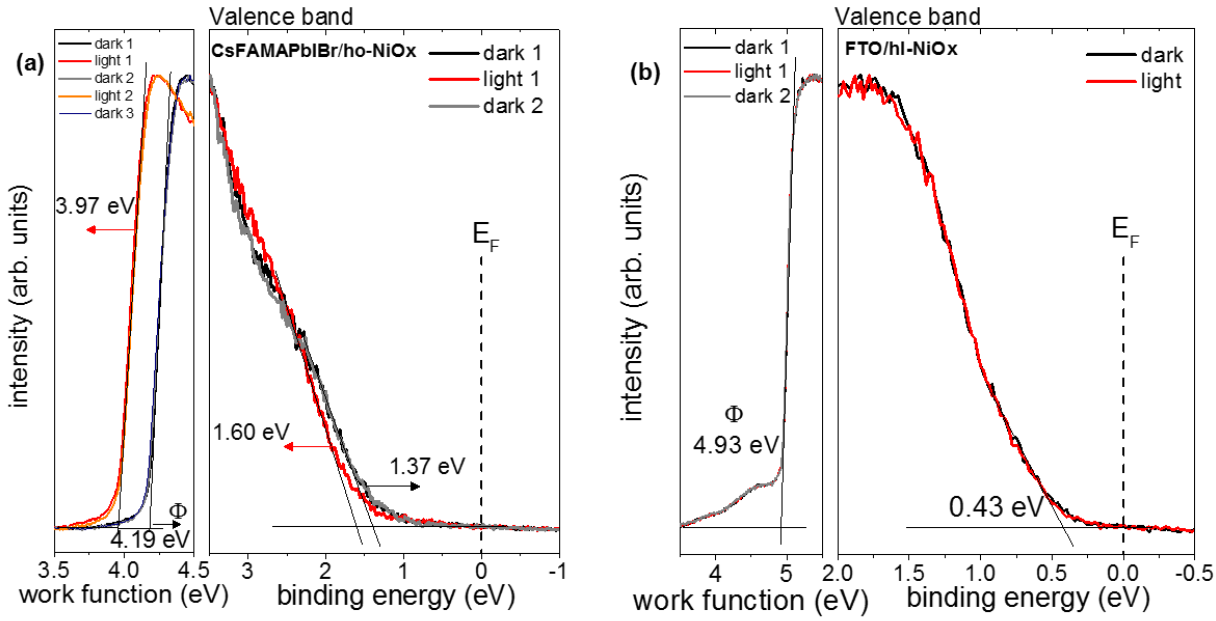


**Figure 4.10.** UPS spectra of (a) ho-$NiO_x$, and (b) hl-$NiO_x$ upon white light illumination. (a) Reversible SECO shift after successive measurements in dark (black), under light (red), in dark (grey), under light (orange), and in dark (blue). (b) The FTO substrate of hl-$NiO_x$ does not have the same active properties as CsFAMAPbBrI, and therefore no charge carriers generation nor distribution were taking place. Consequently, no illumination-induced shift as for the case of hl-$NiO_x$ was observed.

Finally, ambient atmosphere and thermal device stability were compared using ho-$NiO_x$ with the Spiro-OMeTAD reference device. It is widely known that in n-i-p architecture, the HTM layer is the exposed face to degradation agents, therefore being a critical factor to maintain the stability of the device. Aiming to the protection capability of the inorganic HTM, an ambient stability test was performed at humidity of ~65% without any encapsulation. As shown in **Figure 4.11a**, the devices using ho-$NiO_x$ retain around 90% of their initial efficiency after 1008 h (42 days), in contrast with the control device which experienced severe degradation in the first 48 h. Additionally, PSC with HTM free structure were subjected to air stability test also showing a poor PCE retention further indicating the beneficial role of ho-$NiO_x$

as an intrinsic protective layer. Photographs of ho-NiOx-based, Spiro-OMeTAD-based and HTM free PSC are provided in **Figure A4** (Appendix) showing a clear degradation of devices employing Spiro-OMeTAD. As shown in **figure 4.11b**, the most affected photovoltaic parameter of the reference device employing Spiro-OMeTAD was $J_{sc}$, also corroborated in EQE spectrum, as shown in **Figures 4.12a** and **4.12b**. This fact is significant, and directly correlated with water permeation through the HTM layer due to hygroscopic dopants employed for Spiro-OMeTAD.[60] A suitable explanation for the barrier properties of the ho-$NiO_x$ is the hydrophobic nature of the alkyl chains of the oleylamine molecule used to functionalize the nanoparticles. Wetting angles of 112° and 75° degrees, were measured for ho-$NiO_x$ and Spiro-OMeTAD, respectively (**Figure 4.12c**). The superior hydrophobicity of the ho-$NiO_x$ films provides an intrinsic barrier against ambient moisture, conferring excellent stability to the device.

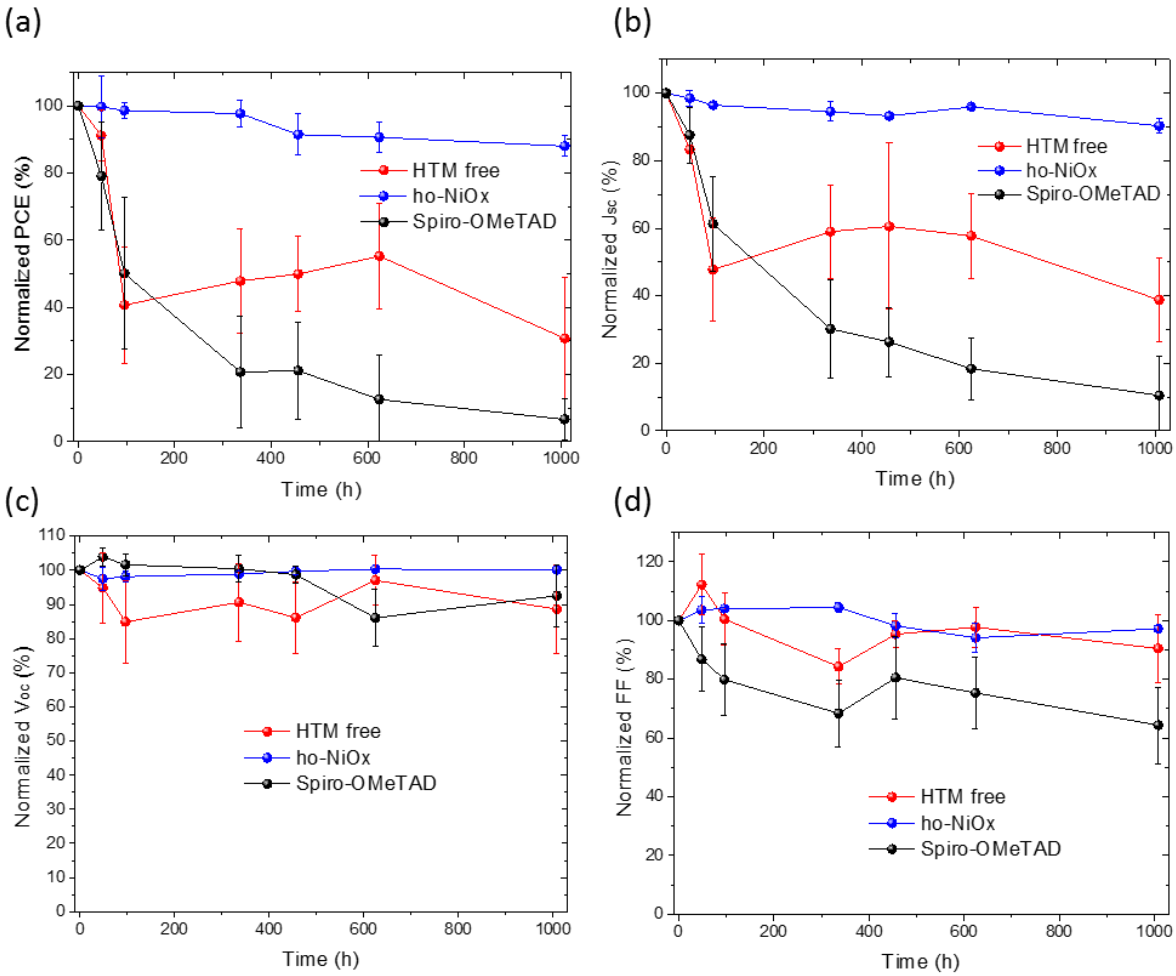


**Figure 4.11.** Air stability test of unencapsulated PSC at ~65% RH. Photovoltaic parameters monitoring is showed for devices employing ho-$NiO_x$ (blue), Spiro-OMeTAD (black) and HTM free (red).

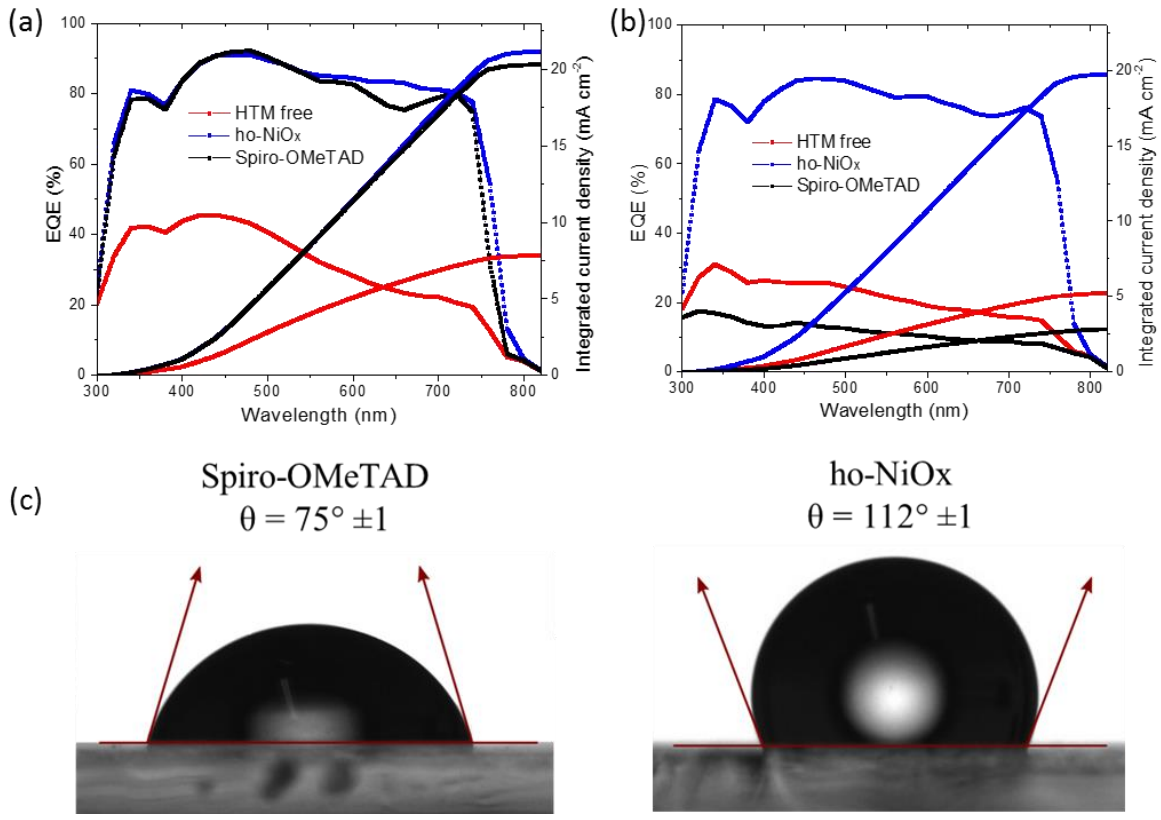


**Figure 4.12.** (a) EQE spectra and integrated $J_{sc}$ of PSC employing different HTM at beginning of stability test (a) and after 1008 h (b). (c) Contact angle of Spiro-OMeTAD and ho-NiO$_x$ films deposited on CsFAMAPbIBr perovskite.

To further investigate the thermal stability the devices were subjected to 85°C in a nitrogen atmosphere (results are shown in **Figure 4.13**). A superior stability of the ho-NiO$_x$ is obtained compared to the reference device. Nonetheless, the devices roughly retained 60% of the initial efficiency after 600 h. This PCE reduction can be related only to morphological changes in device layers by thermal stress since chemical changes are not expected in inert atmosphere at 85°C. A deeper analysis to the photovoltaic parameters revealed that the $V_{oc}$ of the ho-NiO$_x$-based device is more affected by temperature than that of the reference device, which may be attributed to the dewetting of the metal oxide thin film[153] forming interfacial defects that are evidenced in the $V_{oc}$ decrease. However, a higher stability in the *FF* for the

ho-$NiO_x$ containing devices. According to literature, the fill factor reduction is typically attributed to diffusion of gold within the HTM, producing shunts across the device.[154] This could suggest that ho-$NiO_x$ films are less prone to gold diffusion.

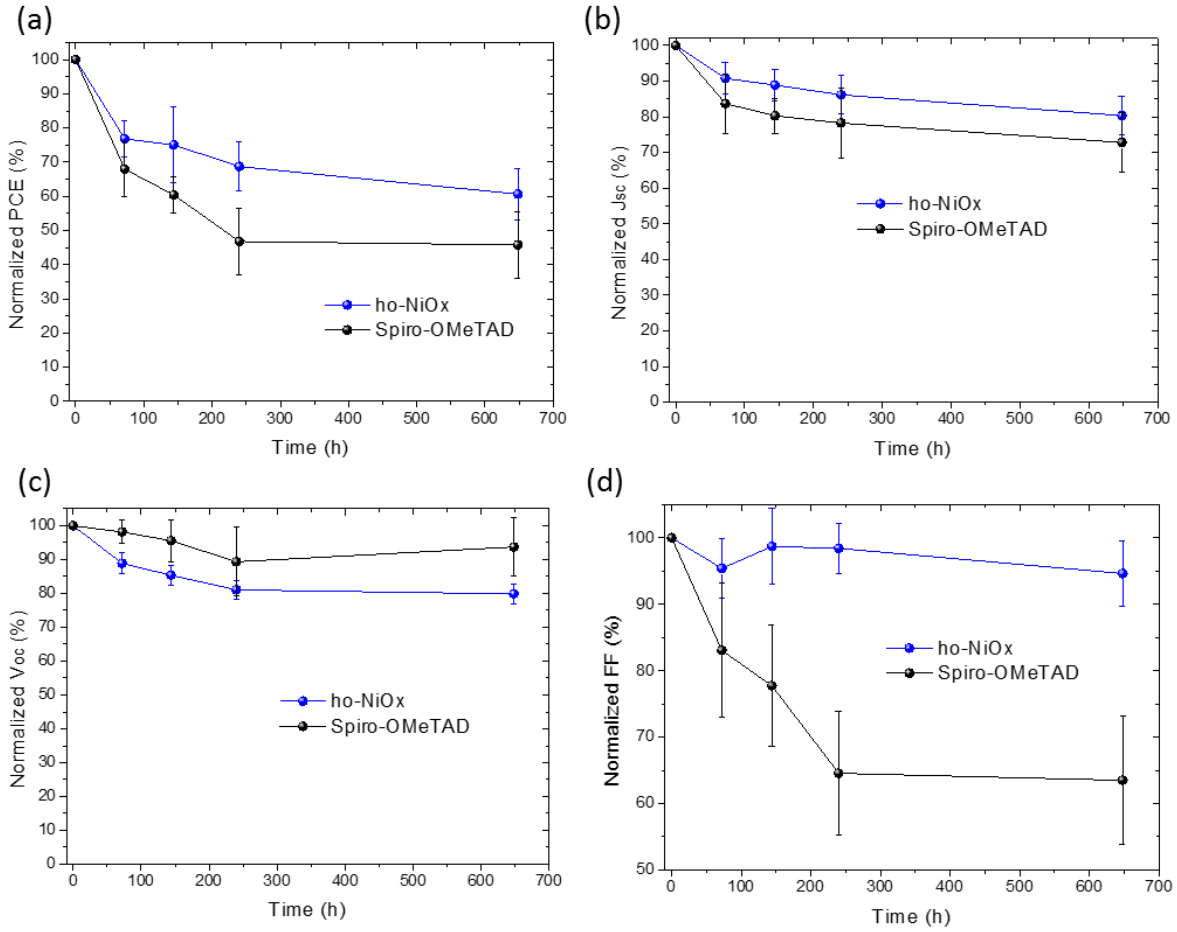


**Figure 4.13.** Thermal stability test of unencapsulated PSC at 85°C and nitrogen atmosphere. Photovoltaic parameters monitoring is showed for devices employing ho-$NiO_x$ (blue) and Spiro-OMeTAD (black).

## 4.4. Conclusions

In summary, hydrophobic p-type $NiO_x$ nanocrystals were obtained from hydrophilic material employing a ligand exchange route which allows the formation of oleylamine capped nanocrystals via low temperature process. The so called ho-$NiO_x$ material can be dispersed in non-polar solvents that are chemically compatible

with perovskite and low-temperature solution based n-i-p perovskite devices. The capability of preparing ho-$NiO_x$ nanocrystals opens the way for replacing expensive HTMs, as Spiro-OMeTAD, with earth abundant inorganic materials in planar direct architectures. Remarkably, a champion PCE of 12.71% and a stabilized power output of 10.99% were obtained, being the highest values reported so far in literature. Our findings suggest that NiOx-based PSC could be improved by interface passivation, as well as increasing $NiO_x$ conductivity with other ligand alternatives or by doping. Noteworthy, ho-$NiO_x$ nanocrystals behave as protecting barrier against high-humidity environments, allowing ~90% PCE retention after 1008 h stored in ~65% RH air, without encapsulation. In contrast, Spiro-OMeTAD-based devices only retained ~5% of the initial PCE. Therefore, this work provides a strategy to effectively apply low-cost $NiO_x$ nanocrystals as HTM in high air-stable n-i-p PSC by a facile solution process route, providing a guideline to improve device performance towards large-scale compatible, stable and cost-effective PSC.

# 5. Experimental Part

## 5.1. P-type semiconductor synthesis procedures

### 5.1.1 Deposition of $Cu_xS$ films

$Cu_xS$ films were deposited on glass slides substrates using a modified spray pyrolysis method proposed by Adelifard et al. [104]. First, substrates were washed with neutral soap and sonicated in deionized (DI) water for 5 minutes. Then, they were placed on a hot plate at 285° C. Sequentially, an aqueous solution of Copper (II) acetate (Sigma-Aldrich) (0.02 M) and Thiourea (Panreac) (0.06 M) was sprayed over the substrates using an in-house spray coater. Process conditions included 40 psi air pressure, 20 cm gap between spray head and substrate, and the solution was deposited in cycles of 2 s at a 5 ml/min rate. 4, 5, 6 or 7 cycles were used to achieve different $Cu_xS$ film thicknesses.

### 5.1.2. Synthesis of CuS nanoparticles.

In a typical procedure two separated precursor solutions were prepared. One with 0.120 g of sulfur powder (S, 99.9%; Sigma Aldrich) and the other with 0.425 g of copper chloride dihydrate (Sigma Aldrich, 99.999%) dissolved in 20 ml and 10 ml of oleylamine (Sigma Aldrich, 70%), respectively. The latter solution was heated to reach 150°C and then sulfur solution was rapidly added. Reaction was maintained for 3 min and then the mixture was cooled down to room temperature. Product was collected by centrifugation at 5000 rpm for 3 min, washed five times with ethanol to remove oleylamine remnants and finally dispersed in toluene to obtain a 47 mg/ml stable dispersion.

### 5.1.3. Synthesis of $NiO_x$ nanocrystals.

Hydrophilic nanoparticles (NPs) of nickel oxide were synthesized by employing a chemical precipitation method previously reported by Zhang et al.[155] In a typical procedure, $Ni(NO_3)_2.6H_2O$ (1.4 g, Merck) was dispersed with magnetic stirring in 1 mL of deionized water to obtain a dark green solution. Employing NaOH solution (10 M, Sigma-Aldrich) pH of previous solution was adjusted to 10. The green precipitate was washed with deionized water twice and then dried at 80°C for 12 h. The as prepared green solid was annealed at 270°C for 3 h obtaining a dark-black powder. Finally, 150 mg of black product were added to a solution composed of 10 μL Oleic Acid (Sigma Aldrich, 90%), 500 μL Oleylamine (Sigma Aldrich, 70%) and 1.5 ml of chlorobenzene. The previous mixture was magnetic stirred at ambient temperature (~20°C) for 24 h to obtain a colloidal dispersion. Then, ethanol was added to precipitate the functionalized nanocrystals which were collected by centrifugation at 4000 rpm. Subsequently, the obtained hydrophobic nickel oxide product was washed twice with ethanol and dried at 60°C for 4 h.

## 5.2. Device fabrication procedures.

### 5.2.1 Fabrication protocol for p-i-n PSC employed as proof of concept of $Cu_xS$ semitransparent electrode.

Devices were fabricated on $Cu_xS$ and ITO coated glass (Naranjo) as reference. The ITO substrates were washed with neutral soap (Inmunodet neutro) and sequentially sonicated in DI water, acetone and isopropanol for 5 minutes. Ultraviolet ozone (UVO) treatment was done for 5 min at 100 °C, for both ITO and $Cu_xS$ electrodes devices. To obtain a perovskite layer, a precursor solution of methylammonium iodide (Dyesol) and lead iodide (Alfa Aesar; 1:1 molar ratio; 55% wt.) in N,N-dimethylformamide (DMF) was deposited by spin-coating at 4000 rpm for 25 s.

During spinning, 500 μL of diethyl ether (Aldrich) were dripped on the substrate after 10 seconds and the films were annealed at 65 °C for 1 min and 100 °C for 10 min. $PC_{61}BM$ (1-Material) was deposited via spin-coating a 20 mg/mL solution in chlorobenzene (CB) at 2000 rpm for 30 s. Rhodamine 101 was deposited on top of the PC61BM layer by spin coating a 0.5 mg/mL solution in anhydrous isopropanol at 4000 rpm for 30 s. Finally, to complete the devices, 100 nm silver electrodes were thermally evaporated (base pressure $10^{-6}$ mbar) at a deposition rate around ≈ 0.1 nm $S^{-1}$. In order to have trustworthy statics 16 devices employing each copper sulfide thickness were prepared.

### 5.2.2. Protocol for mesoscopic n-i-p PSC using CuS nanoparticles as HTM.

Chemically etched FTO glass (Nippon Sheet Glass) was sequentially cleaned by sonication in a 2% Helmanex soap solution, acetone and ethanol for 15 min each, followed by a UV-ozone treatment for 15 min. Then a solution of 0.045 g/ml titanium diisopropoxide bis(acetylacetonate) (Sigma-Aldrich) in anhydrous ethanol was sprayed at 450°C to deposit a 30 nm thick $TiO_2$ compact layer. To form a 200 nm mesoporous $TiO_2$ layer a 0.11 g/ml ethanol solution of a commercially available $TiO_2$ paste (Dyesol 30NRD) was spin-coated at 2000 rpm and substrates were annealed at 500°C for 30 min. Afterwards, a 0.1 M solution of Li-TFSI in acetonitrile was deposited at 3000 rpm for 10 s, followed by a sintering at 500°C for 30 min. $MAPbI_3$ precursor solution was prepared by mixing 1.5 M $PbI_2$ and 1.5 M $CH_3NH_3I$ in DMSO. CsFAMAPbIBr solution was prepared by mixing 1.15 M $PbI_2$, 0.19 M $PbBr_2$, 1.1 M formamidinium iodide (FAI) and 0.19 M methylammonium bromide (MABr) in a mixture of DMF and DMSO with a 4:1 volume ratio (solution A). Subsequently, a solution B was fabricated by mixing 1.15 M CsI and 1.15 M $PbI_2$ in DMSO. Then solution A and B were mixed in a volume ratio of 10:1 to have the triple cation perovskite precursor. $MAPbI_3$ was then deposited at 1000 rpm for 10 s (500 rpm $s^{-1}$,

first step) and 4000 rpm for 30 s (2000 rpm $s^{-1}$, second step). 10 s prior to the end of the program, 100 μl of chlorobenzene were dropped. For the CsFAMAPbIBr perovskite it was used 2000 rpm for 12 s (200 rpm $s^{-1}$), and 5000 rpm for 25 s (2000 rpm $s^{-1}$). In this step chlorobenzene was dropped 9 s before the end of the process. Afterwards, films were annealed at 100°C for 60 min. A 47 mg/ml CuS NPs dispersion was then dynamically spin-coated. Finally, the gold electrode (70 nm) was deposited by thermal evaporation.

### 5.2.3. Fabrication of planar n-i-p PSC employing ho-$NiO_x$ as HTM.

ITO coated glass (Naranjo) was sequentially cleaned by sonication in a 2% Helmanex soap solution, acetone and ethanol for 15 min each, followed by a UV-ozone treatment for 15 min. Then a thin layer of $SnO_2$ was deposited by two steps method. First, a 0.048 M $SnCl_2.2H_2O$ (Sigma Aldrich, 98%) solution in ethanol was spin-coated at 3000 rpm for 30 s on ITO substrates which were then annealed at 180°C for 1 h. Subsequently, the previous substrates were submerged for 3 h in a chemical bath at 70°C typically composed of 3.75 g Urea (Sigma Aldrich, 99%), 62.5 μL 3-mercaptopropionic acid (Sigma Aldrich, 99%), 3.75 ml HCl (Sigma Aldrich, 37%) and 675 mg $SnCl_2.2H_2O$ (Sigma Aldrich, 98%) in 250 ml of deionized water. Then, substrates were washed with deionized water, annealed at 180°C for 1 h and underwent to UV-ozone treatment for 15 min. Afterwards, a 500 nm CsFAMAPbIBr perovskite layer was fabricated employing one step deposition process as follows. CsFAMAPbIBr solution was prepared by mixing 1.15 M $PbI_2$, 0.19 M $PbBr_2$, 1.1 M formamidinium iodide (FAI) and 0.19 M methylammonium bromide (MABr) in a mixture of DMF and DMSO with a 4:1 volume ratio (solution A). Subsequently, a solution B was fabricated by mixing 1.15 M CsI and 1.15 M $PbI_2$ in DMSO. Then solution A and B were mixed in a volume ratio of 10:1 to have the triple cation perovskite precursor. Deposition was carried out by spin-coating this solution at

2000 rpm for 12 s (200 rpm $s^{-1}$), and 5000 rpm for 25 s (2000 rpm $s^{-1}$). In this step chlorobenzene was dropped 9 s before the end of the process. Afterwards, films were annealed at 100°C for 60 min. Later, nickel oxide dispersions in chlorobenzene at different concentrations were spin-coated on top of CsFAMAPbIBr layer. For control devices Spiro-OMeTAD was spin-coated at 4000 rpm for 20 s. The Spiro-OMeTAD solution was prepared by dissolving in chlorobenzene at 70 mM and adding 4-tert-butylpyridine and Li-TFSI in acetonitrile at the molar ratio of Spiro : Li- TFSI : TBP of 1 : 0.5 : 3.3. Finally, the gold electrode (70 nm) was deposited by thermal evaporation.

**5.3. Characterization techniques.**

*Electrical characterization and evaluation of PSC J-V curves.*

The electrical characterization of the devices was performed using a 4200SCS Keithley system at a voltage swept speed around 50 mV/s in combination with an Oriel sol3A sun simulator, which was calibrated to AM1.5G standard conditions using an Oriel 91150 V reference cell. An Oriel IQE 200 was used to determine the external quantum efficiency (EQE).

*Conductivity measurements.*

Sheet resistance (Rsq) was calculated by four point probe employing a 4200SCS Keithley system.

*Optical properties.*

Optical transmittance and absorption were measured in the range of 250-800 nm using a Cary 100 Agilent spectrophotometer and the optical bandgap of different materials was determined using a method reported elsewhere [156].

*X-ray diffraction.*

The XRD measurement were obtained with a Rigaku Ultima III X-ray diffractometer operating at 40 KV accelerating voltage and 44 mA current

*FTIR and Raman spectra.*

FTIR and Raman spectra were collected in a shimadzu Tracer with ATR and a Horiba LabRAM HR with Laser 632 nm, respectively.

*Transmission electron microscopy.*

TEM images were obtained in a Tecnai F20 Super Twin TMP equipment.

*Scanning electron microscopy.*

Cross-section and surface SEM-images were taken in a Hitachi-4800 UHR SEM.

*Atomic force microscopy.*

Surface roughness, thickness and topography images of the different layers were obtained using a Bruker DektakXT profilometer and a MFP-3D infinity AFM (Asylum Research). Surface photo voltage (SPV) of perovskite films and $NiO_x$ layers was carried out using Kelvin Probe Force Microscopy (KPFM) technique in a MFP-3D infinity AFM (Asylum Research) with a maximum irradiance of 3 W $m^{-2}$.

*X-ray photoelectron spectroscopy and ultraviolet photoelectron spectroscopy.*

Photoelectron spectroscopy (PES) measurements were performed in a ultra-high vacuum analysis chamber (base pressure of 2 x 10-10 mbar) using a He-discharge UV source (Omicron) with an excitation energy of 21.2 eV for UPS and a Al K$\alpha$ X-ray source with an excitation energy of 1486.6 eV for XPS. The photoelectron spectra

were recorded using a Phoibos 100 (Specs) hemispherical energy analyzer at a pass energy of 5 eV for the valence band, 20 eV for the core level spectra, and 50 eV for the survey scans. For work function determination, the secondary electron cut-off (SECO) was recorded by applying a -10 V sample bias to clear the analyzer work function. A mixed Gaussian/Lorentzian peak shape and a Shirley type background were employed for XPS peak fitting with the XPS Peak 4.1 software. Samples were illuminated under white halogen lamp at a power of 150 $mW.cm^{-2}$ (daylight rendering spectrum).

# 6. Appendix

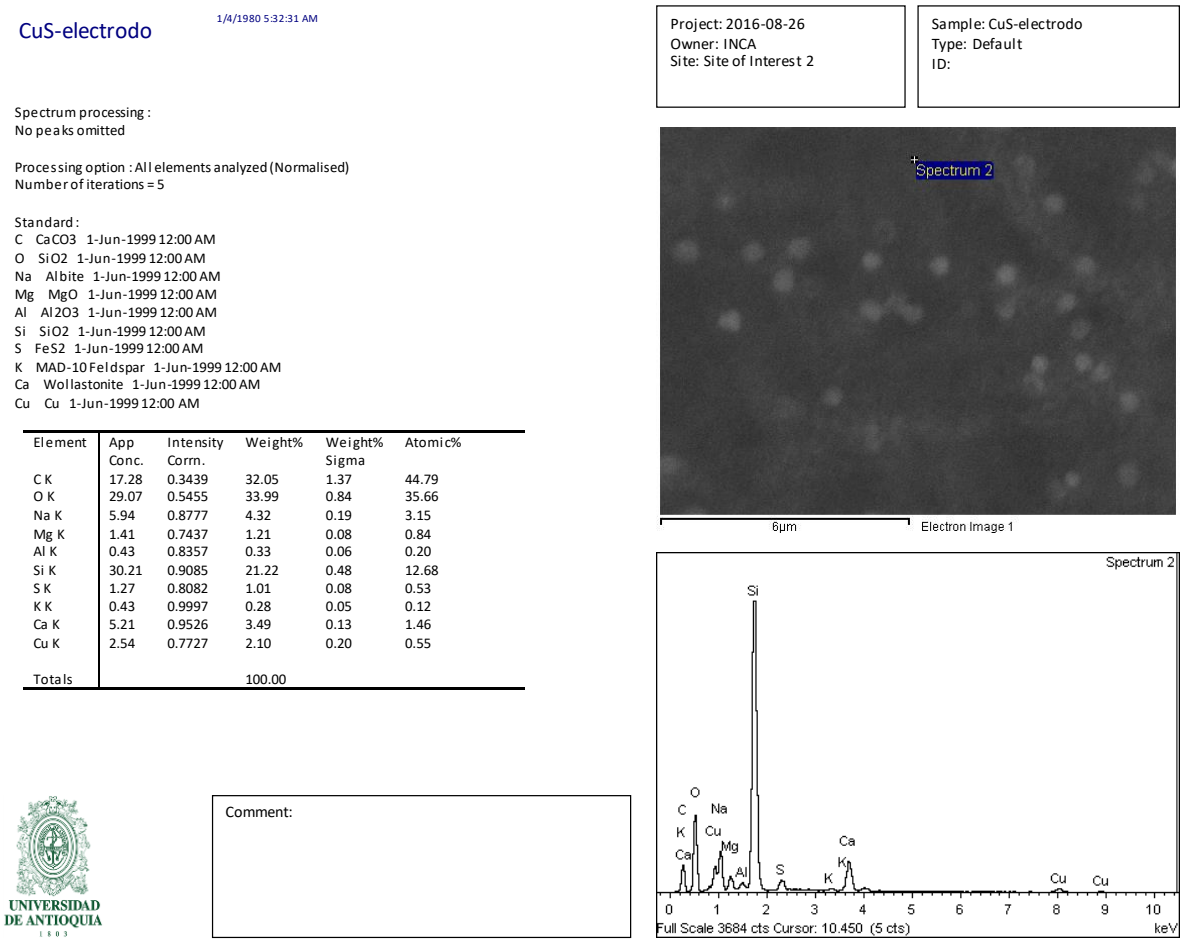

CuS-electrodo 1/4/1980 5:32:31 AM

Project: 2016-08-26
Owner: INCA
Site: Site of Interest 2

Sample: CuS-electrodo
Type: Default
ID:

Spectrum processing :
No peaks omitted

Processing option : All elements analyzed (Normalised)
Number of iterations = 5

Standard :
C CaCO3 1-Jun-1999 12:00 AM
O SiO2 1-Jun-1999 12:00 AM
Na Albite 1-Jun-1999 12:00 AM
Mg MgO 1-Jun-1999 12:00 AM
Al Al2O3 1-Jun-1999 12:00 AM
Si SiO2 1-Jun-1999 12:00 AM
S FeS2 1-Jun-1999 12:00 AM
K MAD-10 Feldspar 1-Jun-1999 12:00 AM
Ca Wollastonite 1-Jun-1999 12:00 AM
Cu Cu 1-Jun-1999 12:00 AM

| Element | App Conc. | Intensity Corrn. | Weight% | Weight% Sigma | Atomic% |
|---|---|---|---|---|---|
| C K | 17.28 | 0.3439 | 32.05 | 1.37 | 44.79 |
| O K | 29.07 | 0.5455 | 33.99 | 0.84 | 35.66 |
| Na K | 5.94 | 0.8777 | 4.32 | 0.19 | 3.15 |
| Mg K | 1.41 | 0.7437 | 1.21 | 0.08 | 0.84 |
| Al K | 0.43 | 0.8357 | 0.33 | 0.06 | 0.20 |
| Si K | 30.21 | 0.9085 | 21.22 | 0.48 | 12.68 |
| S K | 1.27 | 0.8082 | 1.01 | 0.08 | 0.53 |
| K K | 0.43 | 0.9997 | 0.28 | 0.05 | 0.12 |
| Ca K | 5.21 | 0.9526 | 3.49 | 0.13 | 1.46 |
| Cu K | 2.54 | 0.7727 | 2.10 | 0.20 | 0.55 |
| Totals | | | 100.00 | | |



UNIVERSIDAD DE ANTIOQUIA 1803

Comment:

**Figure A1.** Energy-dispersive X-ray spectroscopy (EDS) report of $Cu_xS$ semitransparent electrode on glass substrate.

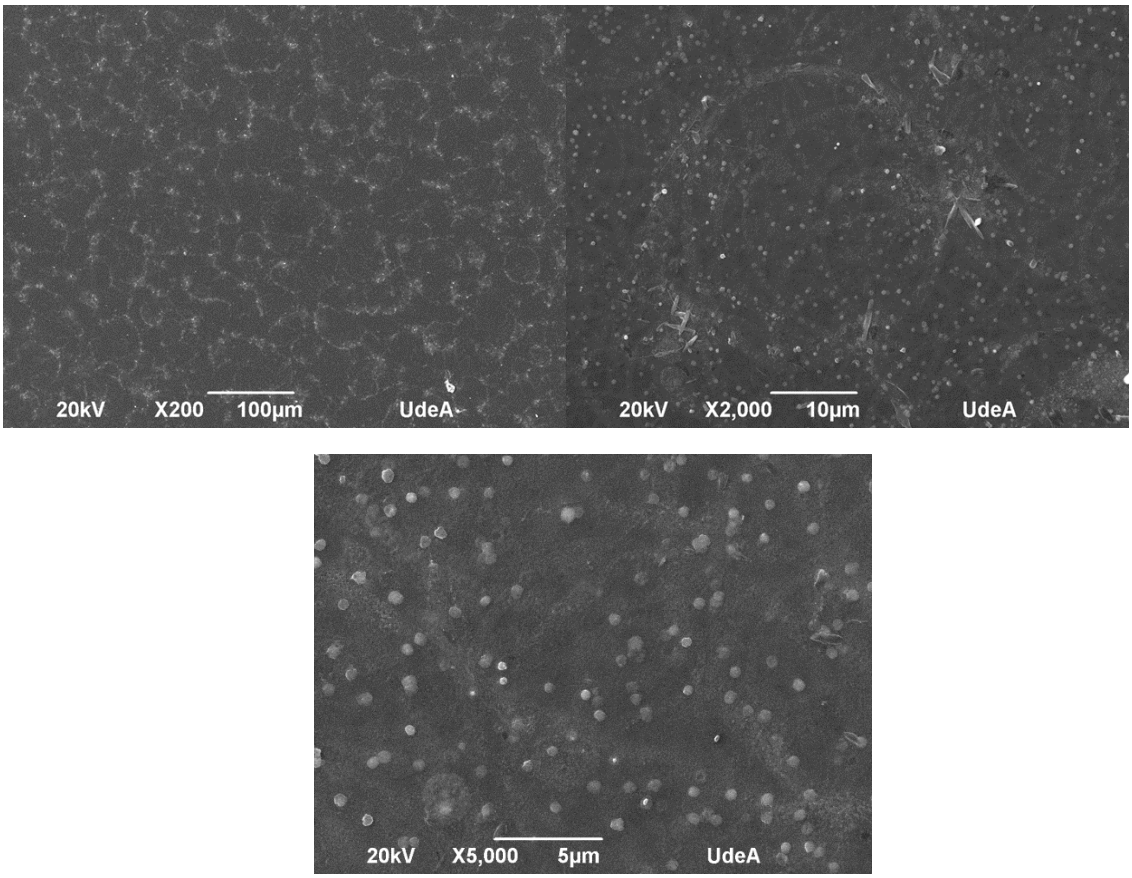


**Figure A2.** SEM micrographs of $Cu_xS$ films on glass at different magnifications.

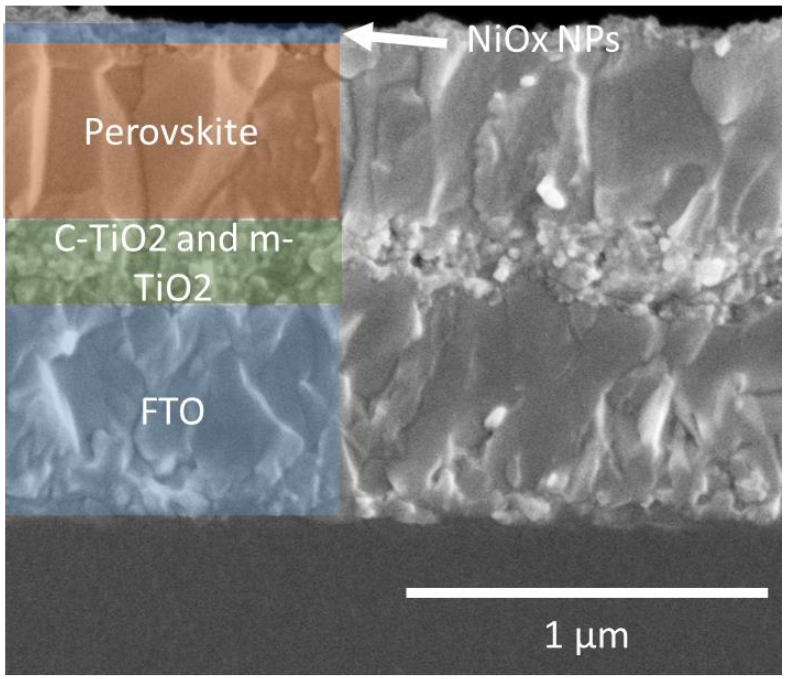


**Figure A3.** Cross-section SEM image of mesoscopic PSC with a layer of ho-$NiO_x$ deposited by spin-coating on top of perovskite layer. This device corresponds to a preliminary work to evaluate ho-$NiO_x$ capability as hole-transport layer.

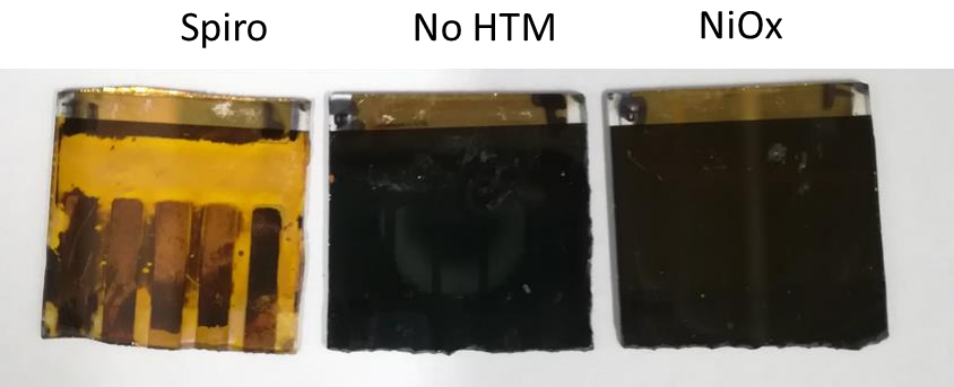


**Figure A4.** Planar n-i-p PSC pictures employing different HTM after 1008 h (42 days) of exposure to ambient air (RH~65%, 20°C) without any encapsulation.

**Cost Assessment of CuS nanoparticles**

CuS nanoparticles (NPs) cost by square meter was calculated by taking account only raw materials prices and quantities for a typical lab scale batch. Then this total cost was divided by the potential covered area using the obtained CuS NPs colloidal dispersion. The simple mathematical model is shown below and was extended to estimate Spiro-OMeTAD cost by square meter.

$$CuS\ NPs\ Cost/m^2 = \frac{M_{Cu} \cdot C_{Cu} + M_{OLA} \cdot C_{OLA} + M_S \cdot C_S}{A}$$

$$A = \frac{V_D}{V_A} \cdot a$$

Where,

$M_{Cu}$: $CuCl_{2.2}H_2O$ mass employed (0.425 g).

$C_{Cu}$: $CuCl_{2.2}H_2O$ cost (0.384 USD/g).

$M_{OLA}$: Oleylamine mass employed (24.39 g).

$C_{OLA}$: Oleylamine cost (0.135 USD/g).

$M_S$: Sulfur mass employed (0.12 g).

$C_S$: Sulfur cost (0.16 USD/g).

$A$: Total area covered by obtained CuS NPs dispersion ($m^2$).

$V_D$: CuS NPs dispersion volume obtained in a typical lab scale batch (4 ml).

$V_A$: Volume of one aliquot to cover 1 $in^2$ or $6.45 \times 10^{-4}\ m^2$ (0.05 ml).

$a$: Area covered by one aliquot of CuS NPs dispersion ($6.45 \times 10^{-4}\ m^2$).

$$Spiro - OMeTAD\ Cost/m^2 = \frac{M_{Spiro} \cdot C_{Spiro}}{A}$$

Where,

$M_{Spiro}$: Spiro-OMeTAD mass employed to cover the same area than using CuS NPs (0.3125 g).

$C_{Spiro}$: Spiro-OMeTAD cost (262.8 USD/g).

$A$: Total area covered by obtained CuS NPs dispersion ($m^2$).

# 7. General conclusions and outlook

$Cu_xS$ films were synthesized by spray pyrolysis technique obtaining a mixture of digenite and covellite crystal phases with high conductivity, p-type character and moderate transmittance over solar spectrum. The suitability of this layer to act as front electrode was evaluated in a p-i-n PSC configuration resulting in an ITO-free PSC. PCE as high as 5.96% was observed along with high FF over 70%. As expected electronic properties and especially surface defects of perovskite absorber depended on the substrate nature which was analyzed by SPV measurements. In brief, $Cu_xS$ nature seems to induce more defects at perovskite surface limiting $V_{oc}$ which also suggests that $Cu_xS$-based PSC can enhance their performance by proper increasing this photovoltaic parameter. Interestingly, PSC employing $Cu_xS$ films as semi-transparent electrode shows a tremendous reduction of materials device cost around 77% highlighting the potential application of this material by simple spray pyrolysis technique in PSC or other optoelectronic devices.

On the other hand, pure covellite CuS nanoparticles were synthesized employing alkyl ligands and characterized so that stable colloidal dispersions in non-polar solvents were obtained. The capability of CuS NPs as HTM in PSC was probed in a mesoscopic n-i-p architecture by completely replacing state-of-the-arte Spiro-OMeTAD. The effect of CuS NPs on device performance was evaluated employing two different perovskite absorbers: $CH_3NH_3PbI_3$ and $(FAPbI_3)_{0.78}(MAPbBr_3)_{0.14}(CsPbI_3)_{0.08}$. Champion PCE of 13.47% and 11.85% were obtained, respectively, being the highest reported efficiency of PSC with a single layer of CuS as HTM. UPS and PL measurements suggests that PCE is meanly limited by non-radiative recombination at perovskite/HTM interface due to a big difference in VB of corresponding materials and metallic nature of CuS NPs (acting as a recombination center).

Finally, hydrophobic $NiO_x$ nanocrystals (ho-$NiO_x$) were synthesized by a ligand exchange method. An optimization trial including variations in precursor concentration and spin-coating conditions was employed to find the best deposition conditions of ho-$NiO_x$ as HTM in a planar n-i-p PSC structure. HTM films around 50 nm thickness exhibited the best PCE around 12.7%, being the maximum PCE reported so far for single layer of $NiO_x$ as HTM in n-i-p architecture. Moreover, $V_{oc}$ was similar to control devices using Spiro-OMeTAD with *FF* as the limiting factor. Meanwhile UPS measurements indicate a good energy band alignment between ho-$NiO_x$ and perovskite even better than perovskite/Spiro-OMeTAD, Conductivity and SPV analysis suggest a lower conductivity of inorganic HTM and the presence of non-radiative recombination paths at perovskite/ho-$NiO_x$ interface. Remarkably, hydrophobic nature of ho-$NiO_x$ nanocrystals leads to formation of a hydrophobic layer on top of perovskite which serves as protecting barrier against ambient moisture, so that unencapsulated PSC exhibited ~90% of PCE retention for more than 1000 h which is desirable for operational conditions.

Synthesis and deposition protocols showed in this work as well as different findings obtained are tended to increase the knowledge about the effect of some almost unexplored inorganic HTM on PSC performance. The promising results discussed in this work pay the way for new improvements in this subject so that inorganic HTM could reach organic counterparts performance with the added value of higher stability and lower cost. In addition, I described some routes which could be followed to enhance the results reported here:

Further studies should be carried out to understand the relation between crystal phase composition of $Cu_xS$ films and PSC behavior. Specifically, the effects on perovskite absorber crystallinity, surface traps sites and stability. Mentioned crystal phase compositions might be tuned by varying spray pyrolysis temperature and

reagents molar ratio. Thus, $Cu_xS$-based ITO-free PSC could achieve attractive performances.

CuS NPs probed to be a promising low-cost strategy to have fully-inorganic blocking layers PSC which is really desirable for commercialization purposes. However, PCE should be increased to values comparable with organic HTM behavior. Findings exposed in this work suggested that a proper interlayer between perovskite/CuS should reduce non-radiative recombination rates so that $V_{oc}$ could reach state-of-the-art numbers. Materials suitable for this interlayer can be ultra-thin insulating films or other inorganic HTM dispersed in anhydrous solvents which will not be dissolved by non-polar solvents of CuS NPs precursor. Primarily, it is mandatory to keep the inorganic and chemical stable nature of HTM bilayer to preserve the advantages of as synthesized CuS NPs.

Hydrophobic $NiO_x$ nanocrystals (ho-$NiO_x$) showed an interesting combination of properties and effects on PSC performance: reasonable PCE, better thermal stability than state-of-the-art HTM and an impressive ambient stability. Thus, ho-$NiO_x$ is a promising material to achieve high performance and scalable fully-inorganic blocking layers PSC by increasing device PCE. A reasonable strategy could be to enhance HTM conductivity and hole mobility by chemical doping with proper elements such as Cu, Ag or Cs, an approach that has been effective in p-i-n architecture. On the other hand, HTM properties can be tuned by ligand exchange with shorter molecules than oleylamine so that interconnection between $NiO_x$ nanocrystals and contact with perovskite absorber could be improved. Therefore, photovoltaic parameters such as *FF* and $V_{oc}$ are expected to increase while keeping chemical stability related to the inorganic HTM.

# 8. References


1 J. Yan and B. R. Saunders, *RSC Adv.*, 2014, **4**, 43286–43314.

2 *Press Release from World Energy Outlook (WEO-2013), International Energy Agency*, 2013.

3 M.-E. Ragoussi and T. Torres, *Chem. Commun.*, 2015, **51**, 3957–3972.

4 K. D. G. I. Jayawardena, L. J. Rozanski, C. A. Mills, M. J. Beliatis, N. A. Nismy and S. R. P. Silva, *Nanoscale*, 2013, **5**, 8411–27.

5 REN 21, *RENEWABLES 2018 GLOBAL STATUS REPORT*, 2018.

6 M. Cai, Y. Wu, H. Chen, X. Yang, Y. Qiang and L. Han, *Adv. Sci.*, 2017, **4**, 1600269.

7 A. Kojima, K. Teshima, Y. Shirai and T. Miyasaka, *J. Am. Chem. Soc.*, 2009, **131**, 6050–6051.

8 W. S. Yang, B.-W. Park, E. H. Jung, N. J. Jeon, Y. C. Kim, D. U. Lee, S. S. Shin, J. Seo, E. K. Kim, J. H. Noh and S. Il Seok, *Science (80-. ).*, 2017, **356**, 1376 LP-1379.

9 J.-P. Correa-Baena, A. Abate, M. Saliba, W. Tress, T. Jesper Jacobsson, M. Gratzel and A. Hagfeldt, *Energy Environ. Sci.*, 2017, **10**, 710–727.

10 H. J. Snaith, *J. Phys. Chem. Lett.*, 2013, **4**, 3623–3630.

11 T. C. Sum and N. Mathews, *Energy Environ. Sci.*, 2014, **7**, 2518–2534.

12 R. Singh, P. K. Singh, B. Bhattacharya and H.-W. Rhee, *Appl. Mater. Today*, 2019, **14**, 175–200.

13 K. Qin, B. Dong and S. Wang, *J. Energy Chem.*, 2019, **33**, 90–99.

14 J.-P. Correa-Baena, M. Saliba, T. Buonassisi, M. Grätzel, A. Abate, W. Tress and A. Hagfeldt, *Science (80-. ).*, 2017, **358**, 739 LP-744.

15 S. Il Seok, M. Grätzel and N.-G. Park, *Small*, 2018, **14**, 1704177.

16 N.-G. Park, *Mater. Today*, 2015, **18**, 65–72.

17 K. Domanski, EPFL PP - Lausanne, 2018.

18 K. Zhu, T. Miyasaka, J. Y. Kim and I. Mora-Seró, *J. Phys. Chem. Lett.*, 2015, **6**, 2315–2317.

19 J. Chen and N.-G. Park, *Adv. Mater.*, 2018, **0**, 1803019.

20 A. Kojima, K. Teshima, Y. Shirai and T. Miyasaka, *J. Am. Chem. Soc.*, 2009, **131**, 6050–6051.

21 H.-S. Kim, C.-R. Lee, J.-H. Im, K.-B. Lee, T. Moehl, A. Marchioro, S.-J. Moon, R. Humphry-Baker, J.-H. Yum, J. E. Moser, M. Gratzel and N.-G. Park, *Sci. Rep.*, 2012, **2**.

22 M. M. Lee, J. Teuscher, T. Miyasaka, T. N. Murakami and H. J. Snaith, *Science (80-. ).*, 2012, **338**, 643–647.

23 F. Wang, Y. Cao, C. Chen, Q. Chen, X. Wu, X. Li, T. Qin and W. Huang, *Adv. Funct. Mater.*, 2018, **28**, 1803753.

24 J.-Y. Jeng, Y.-F. Chiang, M.-H. Lee, S.-R. Peng, T.-F. Guo, P. Chen and T.-C. Wen, *Adv. Mater.*, 2013, **25**, 3727–3732.

25 J. Cui, F. Meng, H. Zhang, K. Cao, H. Yuan, Y. Cheng, F. Huang and M. Wang, *ACS Appl. Mater. Interfaces*, 2014, **6**, 22862–22870.

26 D. Ramirez, E. Velilla, J. F. Montoya and F. Jaramillo, *Sol. Energy Mater. Sol. Cells*, 2019, **195**, 191–197.

27 S. Pitchaiya, M. Natarajan, A. Santhanam, V. Asokan, A. Yuvapragasam, V. Madurai Ramakrishnan, S. E. Palanisamy, S. Sundaram and D. Velauthapillai, *Arab. J. Chem.*, 2018.

28 P. Tonui, S. O. Oseni, G. Sharma, Q. Yan and G. Tessema Mola, *Renew. Sustain. Energy Rev.*, 2018, **91**, 1025–1044.

29 S. Brittman, G. W. P. Adhyaksa and E. C. Garnett, *MRS Commun.*, 2015, **5**, 7–26.

30 M. I. H. Ansari, A. Qurashi and M. K. Nazeeruddin, *J. Photochem. Photobiol. C Photochem. Rev.*, 2018, **35**, 1–24.

31 G. Grancini, C. Roldán-Carmona, I. Zimmermann, E. Mosconi, X. Lee, D. Martineau, S. Narbey, F. Oswald, F. De Angelis, M. Graetzel and M. K. Nazeeruddin, *Nat. Commun.*, 2017, **8**, 15684.

32 P. Schulz, *ACS Energy Lett.*, 2018, **3**, 1287–1293.

33 L. Fan, Y. Li, X. Yao, Y. Ding, S. Zhao, B. Shi, C. Wei, D. Zhang, B. Li, G. Wang, Y. Zhao and X. Zhang, *ACS Appl. Energy Mater.*, 2018, **1**, 1575–1584.

34 X. Yin, Z. Yao, Q. Luo, X. Dai, Y. Zhou, Y. Zhang, Y. Zhou, S. Luo, J. Li, N. Wang and H. Lin, *ACS Appl. Mater. Interfaces*, 2017, **9**, 2439–2448.

35 X. Li, J. Yang, Q. Jiang, H. Lai, S. Li, Y. Tan, Y. Chen and S. Li, *J. Mater. Chem. A*, 2019.

36 H. S. Jung and N.-G. Park, *Small*, 2015, **11**, 10–25.

37 P. Schulz, D. Cahen and A. Kahn, *Chem. Rev.*, 2019, **119**, 3349–3417.

38 C. Liu, X. Zhou, S. Chen, X. Zhao, S. Dai and B. Xu, *Adv. Sci.*, 2019, **0**, 1801169.

39 X. Yang, H. Wang, B. Cai, Z. Yu and L. Sun, *J. Energy Chem.*, 2018, **27**, 650–672.

40 B. Roose, Q. Wang and A. Abate, *Adv. Energy Mater.*, 2019, **9**, 1803140.

41 Z. H. Bakr, Q. Wali, A. Fakharuddin, L. Schmidt-Mende, T. M. Brown and R. Jose, *Nano Energy*, 2017, **34**, 271–305.

42 H. Lei, G. Fang, F. Cheng, W. Ke, P. Qin, Z. Song, Q. Zheng, X. Fan, H. Huang and X. Zhao, *Sol. Energy Mater. Sol. Cells*, 2014, **128**, 77–84.

43 J. Xiao, J. Shi, H. Liu, Y. Xu, S. Lv, Y. Luo, D. Li, Q. Meng, Y. Li, J. Xiao, J. Shi, Y. Xu, S. Lv, Y. Luo, D. Li, Q. Meng, H. Liu and Y. Li, *Adv. Energy Mater.*, 2015.

44 J. Chen, Z. Chen, D. Yang, F. Ye, S. Wang and X. Yang, *Macromol. Chem. Phys.*, 2015, **216**, 1008–1013.

45 Z. Yu and L. Sun, *Adv. Energy Mater.*, 2015, **5**, n/a-n/a.

46 L. Xu, L.-L. Deng, J. Cao, X. Wang, W.-Y. Chen and Z. Jiang, *Nanoscale Res. Lett.*, 2017, **12**, 159.

47 T. S. Yang, W. Cho, M. Kim, K.-S. An, T.-M. Chung, C. G. Kim and Y. Kim, *J. Vac. Sci. Technol. A*, 2005, **23**, 1238–1243.

48 M. Leskelä and M. Ritala, *Thin Solid Films*, 2002, **409**, 138–146.

49 S. Sajid, A. M. Elseman, H. Huang, J. Ji, S. Dou, H. Jiang, X. Liu, D. Wei, P. Cui and M. Li, *Nano Energy*, 2018, **51**, 408–424.

50 F. Xie, C.-C. Chen, Y. Wu, X. Li, M. Cai, X. Liu, X. Yang and L. Han, *Energy Environ. Sci.*, 2017, **10**, 1942–1949.

51 E. Avigad and L. Etgar, *ACS Energy Lett.*, 2018, **3**, 2240–2245.

52 Y.-J. Chen, M.-H. Li, J.-C.-A. Huang and P. Chen, *Sci. Rep.*, 2018, **8**, 7646.

53 Y. Xu, H. Wang, Y. Yu, L. Tian, W. Zhao and B. Zhang, *J. Phys. Chem. C*, 2011, **115**, 15288–15296.

54 Y.-X. Wang, X.-F. Tang and Z.-G. Yang, *Colloids Surfaces A Physicochem. Eng. Asp.*, 2011, **388**, 38–40.

55 S. Ye, W. Sun, Y. Li, W. Yan, H. Peng, Z. Bian, Z. Liu and C. Huang, *Nano Lett.*, 2015, **15**, 3723–3728.

56 N. Arora, M. I. Dar, A. Hinderhofer, N. Pellet, F. Schreiber, S. M. Zakeeruddin and M. Grätzel, *Science (80-. ).*, 2017.

57 K. Zhao, R. Munir, B. Yan, Y. Yang, T.-S. Kim and A. Amassian, *J. Mater. Chem. A*, 2015.

58 P. Qin, S. Tanaka, S. Ito, N. Tetreault, K. Manabe, H. Nishino, M. K. Nazeeruddin and M. Grätzel, *Nat Commun*, 2014, **5**.

59 M. I. Hossain, F. H. Alharbi and N. Tabet, *Sol. Energy*, 2015, **120**, 370–380.

60 H. Lei, G. Yang, X. Zheng, Z.-G. Zhang, C. Chen, J. Ma, Y. Guo, Z. Chen, P. Qin, Y. Li and G. Fang, *Sol. RRL*, 2017, 1700038–n/a.

61 Z. Liu, A. Zhu, F. Cai, L. Tao, Y. Zhou, Z. Zhao, Q. Chen, Y.-B. Cheng and H. Zhou, *J. Mater. Chem. A*, 2017, **5**, 6597–6605.

62 W. Li, H. Dong, X. Guo, N. Li, J. Li, G. Niu and L. Wang, *J. Mater. Chem. A*, 2014, **2**, 20105–20111.

63 S. N. Habisreutinger, T. Leijtens, G. E. Eperon, S. D. Stranks, R. J. Nicholas and H. J. Snaith, *Nano Lett.*, 2014, **14**, 5561–5568.

64 A. J. Huckaba, P. Sanghyun, G. Grancini, E. Bastola, C. K. Taek, L. Younghui,

K. P. Bhandari, C. Ballif, R. J. Ellingson and M. K. Nazeeruddin, *ChemistrySelect*, 2016, **1**, 5316–5319.

65 D. Han, C. Wu, Q. Zhang, S. Wei, X. Qi, Y. Zhao, Y. Chen, Y. Chen, L. Xiao and Z. Zhao, *ACS Appl. Mater. Interfaces*, 2018.

66 V. E. Madhavan, I. Zimmermann, C. Roldán-Carmona, G. Grancini, M. Buffiere, A. Belaidi and M. K. Nazeeruddin, *ACS Energy Lett.*, 2016, **1**, 1112–1117.

67 J. Tirado, C. Roldán-Carmona, F. A. Muñoz-Guerrero, G. Bonilla-Arboleda, M. Ralaiarisoa, G. Grancini, V. I. E. Queloz, N. Koch, M. K. Nazeeruddin and F. Jaramillo, *Appl. Surf. Sci.*, 2019, **478**, 607–614.

68 S. Akin, Y. Liu, M. I. Dar, S. M. Zakeeruddin, M. Grätzel, S. Turan and S. Sonmezoglu, *J. Mater. Chem. A*, 2018, **6**, 20327–20337.

69 M. Cai, Y. Wu, H. Chen, X. Yang, Y. Qiang and L. Han, *Adv. Sci.*, 2017, **4**, n/a-n/a.

70 T. Salim, S. Sun, Y. Abe, A. Krishna, A. C. Grimsdale and Y. M. Lam, *J. Mater. Chem. A*, 2015, **3**, 8943–8969.

71 P. Qin, N. Tetreault, M. I. Dar, P. Gao, K. L. McCall, S. R. Rutter, S. D. Ogier, N. D. Forrest, J. S. Bissett, M. J. Simms, A. J. Page, R. Fisher, M. Gr??tzel and M. K. Nazeeruddin, *Adv. Energy Mater.*, 2015, **5**, n/a-n/a.

72 M. Liu, M. B. Johnston and H. J. Snaith, *Nature*, 2013, **501**, 395–8.

73 D. Li, J. Cui, H. Zhang, H. Li, M. Wang and Y. Shen, *Chem. Lett.*, 2015, **45**, 89–91.

74 A. Dymshits, A. Rotem and L. Etgar, *J. Mater. Chem. A*, 2014, **2**, 20776–20781.

75 D. S. Ghosh, T. L. Chen, N. Formica, J. Hwang, I. Bruder and V. Pruneri, *Sol. Energy Mater. Sol. Cells*, 2012, **107**, 338–343.

76 M. Dianetti, F. Di Giacomo, G. Polino, C. Ciceroni, A. Liscio, A. D'Epifanio, S. Licoccia, T. M. Brown, A. Di Carlo and F. Brunetti, *Sol. Energy Mater. Sol. Cells*, 2015, **140**, 150–157.

77 H. Hu, D. Wang, Y. Zhou, J. Zhang, S. Lv, S. Pang, X. Chen, Z. Liu, N. P. Padture and G. Cui, *RSC Adv.*, 2014, **4**, 28964–28967.

78 K.-W. Tsai, C.-C. Chueh, S. T. Williams, T.-C. Wen and A. K. Y. Jen, *J. Mater. Chem. A*, 2015, **3**, 9128–9132.

79 R. Wu, J. Yang, J. Xiong, P. Liu, C. Zhou, H. Huang, Y. Gao and B. Yang, *Org. Electron.*, 2015, **26**, 265–272.

80 K. H. L. Z. and K. X. and M. G. B. and R. G. Egdell, *J. Phys. Condens. Matter*, 2016, **28**, 383002.

81 S. Sheng, G. Fang, C. Li, S. Xu and X. Zhao, *Phys. status solidi*, 2006, **203**, 1891–1900.

82 H. Sung, N. Ahn, M. S. Jang, J.-K. Lee, H. Yoon, N.-G. Park and M. Choi, *Adv. Energy Mater.*, 2016, **6**, n/a-n/a.

83 J. Yoon, H. Sung, G. Lee, W. Cho, N. Ahn, H. S. Jung and M. Choi, *Energy Environ. Sci.*, 2017, **10**, 337–345.

84 P. You, Z. Liu, Q. Tai, S. Liu and F. Yan, *Adv. Mater.*, 2015, **27**, 3632–3638.

85 K. Yan, Z. Wei, J. Li, H. Chen, Y. Yi, X. Zheng, X. Long, Z. Wang, J. Wang, J. Xu and S. Yang, *Small*, 2015, **11**, 2269–2274.

86 K. S. Kim, Y. Zhao, H. Jang, S. Y. Lee, J. M. Kim, K. S. Kim, J.-H. Ahn, P. Kim,

J.-Y. Choi and B. H. Hong, *Nature*, 2009, **457**, 706–710.

87 K. Sun, P. Li, Y. Xia, J. Chang and J. Ouyang, *ACS Appl. Mater. Interfaces*, 2015, **7**, 15314–15320.

88 M. Kaltenbrunner, G. Adam, E. D. Glowacki, M. Drack, R. Schwodiauer, L. Leonat, D. H. Apaydin, H. Groiss, M. C. Scharber, M. S. White, N. S. Sariciftci and S. Bauer, *Nat Mater*, 2015, **14**, 1032–1039.

89 M. Ye, X. Wen, N. Zhang, W. Guo, X. Liu and C. Lin, *J. Mater. Chem. A*, 2015, **3**, 9595–9600.

90 W. Ke, G. Fang, H. Lei, P. Qin, H. Tao, W. Zeng, J. Wang and X. Zhao, *J. Power Sources*, 2014, **248**, 809–815.

91 Y. C. Zhang, X. Y. Hu and T. Qiao, *Solid State Commun.*, 2004, **132**, 779–782.

92 X. Chen, Z. Wang, X. Wang, R. Zhang, X. Liu, W. Lin and Y. Qian, *J. Cryst. Growth*, 2004, **263**, 570–574.

93 N. Mukherjee, A. Sinha, G. G. Khan, D. Chandra, A. Bhaumik and A. Mondal, *Mater. Res. Bull.*, 2011, **46**, 6–11.

94 S. S. Kalanur, S. Y. Chae and O. S. Joo, *Electrochim. Acta*, 2013, **103**, 91–95.

95 C. Naşcu, I. Pop, V. Ionescu, E. Indrea and I. Bratu, *Mater. Lett.*, 1997, **32**, 73–77.

96 Y. B. He, A. Polity, I. Österreicher, D. Pfisterer, R. Gregor, B. K. Meyer and M. Hardt, *Phys. B Condens. Matter*, 2001, **308–310**, 1069–1073.

97 H. Rao, W. Sun, S. Ye, W. Yan, Y. Li, H. Peng, Z. Liu, Z. Bian and C. Huang, *ACS Appl. Mater. Interfaces*, 2016, **8**, 7800–7805.

98 K.-J. Huang, J.-Z. Zhang, Y.-L. Jia, K. Xing and Y.-M. Liu, *J. Alloys Compd.*,

2015, **641**, 119–126.

99 F. Li, J. Wu, Q. Qin, Z. Li and X. Huang, *Powder Technol.*, 2010, **198**, 267–274.

100 C. Feng, L. Zhang, M. Yang, X. Song, H. Zhao, Z. Jia, K. Sun and G. Liu, *ACS Appl. Mater. Interfaces*, 2015, **7**, 15726–15734.

101 Z. Xu, T. Li, F. Zhang, X. Hong, S. Xie, M. Ye, W. Guo and X. Liu, *Nanoscale*, 2017.

102 X. Zhang, W. Guo, G. Gao, M. Que, C. Pan and Z. L. Wang, *J. Mater. Chem. C*, 2016, **4**, 4733–4739.

103 D. Perednis and L. J. Gauckler, *J. Electroceramics*, 2005, **14**, 103–111.

104 M. Adelifard, H. Eshghi and M. M. B. Mohagheghi, *Appl. Surf. Sci.*, 2012, **258**, 5733–5738.

105 S. J. Abbas, M. Rani and S. K. Tripathi, *Phys. B Condens. Matter*, 2014, **443**, 107–113.

106 S. B. Sepulveda-Mora and S. G. Cloutier, *J. Nanomater.*, 2012, **2012**.

107 J. Ciro, S. Mesa, J. I. Uribe, M. A. Mejía-Escobar, D. Ramirez, J. F. Montoya, R. Betancur, H.-S. Yoo, N.-G. Park and F. Jaramillo, *Nanoscale*, 2017, **9**, 9440–9446.

108 H. Zhou, L. Yang and W. You, *Macromolecules*, 2012, **45**, 607–632.

109 R. Kaixv, Y. Pengfei, Z. Yuzhu, C. Xingzhong, D. Cunku, C. Lan, L. Hui and D. Xiwen, *Small*, 2017, **13**, 1700867.

110 W. Xu, S. Zhu, Y. Liang, Z. Li, Z. Cui, X. Yang and A. Inoue, *Sci. Rep.*, 2015, **5**, 18125.

111 N. Giesbrecht, J. Schlipf, L. Oesinghaus, A. Binek, T. Bein, P. Müller-Buschbaum and P. Docampo, *ACS Energy Lett.*, 2016, **1**, 150–154.

112 Y. Tidhar, E. Edri, H. Weissman, D. Zohar, G. Hodes, D. Cahen, B. Rybtchinski and S. Kirmayer, *J. Am. Chem. Soc.*, 2014, **136**, 13249–13256.

113 W. Zhang, S. Pathak, N. Sakai, T. Stergiopoulos, P. K. Nayak, N. K. Noel, A. a. Haghighirad, V. M. Burlakov, D. W. DeQuilettes, A. Sadhanala, W. Li, L. Wang, D. S. Ginger, R. H. Friend and H. J. Snaith, *Nat. Commun.*, 2015, **6**, 1–9.

114 J. Liqiang, S. Xiaojun, S. Jing, C. Weimin, X. Zili, D. Yaoguo and F. Honggang, *Sol. Energy Mater. Sol. Cells*, 2003, **79**, 133–151.

115 K.-J. Huang, J.-Z. Zhang and Y. Fan, *J. Alloys Compd.*, 2015, **625**, 158–163.

116 H. Nozaki, K. Shibata and N. Ohhashi, *J. Solid State Chem.*, 1991, **91**, 306–311.

117 X. Jiang, Y. Xie, J. Lu, W. He, L. Zhu and Y. Qian, *J. Mater. Chem.*, 2000, **10**, 2193–2196.

118 H. Grijalva, M. Inoue, S. Boggavarapu and P. Calvert, *J. Mater. Chem.*, 1996, **6**, 1157–1160.

119 J. Tirado, D. Ramirez, R. Betancur and F. Jaramillo, *Thin Solid Films*, 2018, **662**, 90–96.

120 P. Waldner and W. Sitte, *Monatshefte für Chemie - Chem. Mon.*, 2012, **143**, 1215–1218.

121 H. Zhang, Y. Zhang, J. Yu and D. Yang, *J. Phys. Chem. C*, 2008, **112**, 13390–13394.

122 J. Li, T. Jiu, G.-H. Tao, G. Wang, C. Sun, P. Li, J. Fang and L. He, *J. Colloid Interface Sci.*, 2014, **419**, 142–147.

123 N. A. Yeryukov, A. G. Milekhin, L. L. Sveshnikova, T. A. Duda, L. D. Pokrovsky, A. K. Gutakovskii, S. A. Batsanov, E. E. Rodyakina, A. V Latyshev and D. R. T. Zahn, *J. Phys. Chem. C*, 2014, **118**, 23409–23414.

124 M. T. Ramesan, *Polym. Eng. Sci.*, 2014, **54**, 438–445.

125 *Surf. Interface Anal.*, 2017, **49**, 1325–1334.

126 D. L. Perry and J. A. Taylor, *J. Mater. Sci. Lett.*, 1986, **5**, 384–386.

127 J. Ye, X. Zhang, L. Zhu, H. Zheng, G. Liu, H. Wang, T. Hayat, X. Pan and S. Dai, *Sustain. Energy Fuels*, 2017, **1**, 907–914.

128 Z. Yao, W. Wang, H. Shen, Y. Zhang, Q. Luo, X. Yin, X. Dai, J. Li and H. Lin, *Sci. Technol. Adv. Mater.*, 2017, **18**, 253–262.

129 B. Chen, M. Yang, S. Priya and K. Zhu, *J. Phys. Chem. Lett.*, 2016, **7**, 905–917.

130 S. A. L. Weber, I. M. Hermes, S.-H. Turren-Cruz, C. Gort, V. W. Bergmann, L. Gilson, A. Hagfeldt, M. Graetzel, W. Tress and R. Berger, *Energy Environ. Sci.*, 2018, **11**, 2404–2413.

131 M. Saliba, T. Matsui, J.-Y. Seo, K. Domanski, J.-P. Correa-Baena, M. K. Nazeeruddin, S. M. Zakeeruddin, W. Tress, A. Abate, A. Hagfeldt and M. Gratzel, *Energy Environ. Sci.*, 2016, **9**, 1989–1997.

132 Q. Luo, Y. Zhang, C. Liu, J. Li, N. Wang and H. Lin, *J. Mater. Chem. A*, 2015, **3**, 15996–16004.

133 X. Xu, J. Bullock, L. T. Schelhas, E. Z. Stutz, J. J. Fonseca, M. Hettick, V. L. Pool, K. F. Tai, M. F. Toney, X. Fang, A. Javey, L. H. Wong and J. W. Ager, *Nano Lett.*, 2016, **16**, 1925–1932.

134 S. Ravishankar, S. Gharibzadeh, C. Roldán-Carmona, G. Grancini, Y. Lee, M.

Ralaiarisoa, A. M. Asiri, N. Koch, J. Bisquert and M. K. Nazeeruddin, *Joule*, 2018, **2**, 788–798.

135 K. Tvingstedt, O. Malinkiewicz, A. Baumann, C. Deibel, H. J. Snaith, V. Dyakonov and H. J. Bolink, *Sci. Rep.*, 2014, **4**, 6071.

136 V. D'Innocenzo, G. Grancini, M. J. P. Alcocer, A. R. S. Kandada, S. D. Stranks, M. M. Lee, G. Lanzani, H. J. Snaith and A. Petrozza, *Nat. Commun.*, 2014, **5**, 3586.

137 J. Frisch, M. Schubert, E. Preis, J. P. Rabe, D. Neher, U. Scherf and N. Koch, *J. Mater. Chem.*, 2012, **22**, 4418–4424.

138 S. Yue, K. Liu, R. Xu, M. Li, M. Azam, K. Ren, J. Liu, Y. Sun, Z. Wang, D. Cao, X. Yan, S. Qu, Y. Lei and Z. Wang, *Energy Environ. Sci.*, 2017, **10**, 2570–2578.

139 I. Sta, M. Jlassi, M. Hajji and H. Ezzaouia, *Thin Solid Films*, 2014, **555**, 131–137.

140 J. Ciro, D. Ramírez, M. A. Mejía Escobar, J. F. Montoya, S. Mesa, R. Betancur and F. Jaramillo, *ACS Appl. Mater. Interfaces*, 2017, **9**, 12348–12354.

141 C. R. Bhattacharjee, D. D. Purkayastha and J. R. Chetia, *J. Coord. Chem.*, 2011, **64**, 4434–4442.

142 M. Salavati-Niasari, N. Mir and F. Davar, *J. Alloys Compd.*, 2010, **493**, 163–168.

143 M. A. Rahman, M. S. Alam, M. A. J. Miah, M. M. Rahman, D. Dupin and H. Ahmad, *Polym. Adv. Technol.*, 2012, **23**, 1187–1193.

144 M. C. Biesinger, B. P. Payne, L. W. M. Lau, A. Gerson and R. S. C. Smart, *Surf. Interface Anal.*, 2009, **41**, 324–332.

145 W. Chen, Y. Wu, J. Fan, A. B. Djurišić, F. Liu, H. W. Tam, A. Ng, C. Surya, W. K. Chan, D. Wang and Z.-B. He, *Adv. Energy Mater.*, 2018, **8**, 1870091.

146 U. Kwon, B.-G. Kim, D. C. Nguyen, J.-H. Park, N. Y. Ha, S.-J. Kim, S. H. Ko, S. Lee, D. Lee and H. J. Park, *Sci. Rep.*, 2016, **6**, 30759.

147 J.-L. Yang, Y.-S. Lai and J. S. Chen, *Thin Solid Films*, 2005, **488**, 242–246.

148 K. C. Icli and M. Ozenbas, *Electrochim. Acta*, 2018, **263**, 338–345.

149 H. Wang, A. D. Sheikh, Q. Feng, F. Li, Y. Chen, W. Yu, E. Alarousu, C. Ma, M. A. Haque, D. Shi, Z.-S. Wang, O. F. Mohammed, O. M. Bakr and T. Wu, *ACS Photonics*, 2015, **2**, 849–855.

150 L. Barnea-Nehoshtan, S. Kirmayer, E. Edri, G. Hodes and D. Cahen, *J. Phys. Chem. Lett.*, 2014, **5**, 2408–2413.

151 D. Luo, W. Yang, Z. Wang, A. Sadhanala, Q. Hu, R. Su, R. Shivanna, G. F. Trindade, J. F. Watts, Z. Xu, T. Liu, K. Chen, F. Ye, P. Wu, L. Zhao, J. Wu, Y. Tu, Y. Zhang, X. Yang, W. Zhang, R. H. Friend, Q. Gong, H. J. Snaith and R. Zhu, *Science (80-. ).*, 2018, **360**, 1442 LP-1446.

152 Z. Hawash, S. R. Raga, D.-Y. Son, L. K. Ono, N.-G. Park and Y. Qi, *J. Phys. Chem. Lett.*, 2017, **8**, 3947–3953.

153 C. V. Thompson, *Annu. Rev. Mater. Res.*, 2012, **42**, 399–434.

154 K. Domanski, J. P. Correa-Baena, N. Mine, M. K. Nazeeruddin, A. Abate, M. Saliba, W. Tress, A. Hagfeldt and M. Grätzel, *ACS Nano*, 2016, **10**, 6306–6314.

155 H. Zhang, J. Cheng, F. Lin, H. He, J. Mao, K. S. Wong, A. K.-Y. Jen and W. C. H. Choy, *ACS Nano*, 2016, **10**, 1503–1511.

156 A. Venter and J. R. Botha, *S Afr J Sci*, 2011, **107**.